Integrin αIIbβ3 - a journey from protein to cell

Inauguraldissertation

zur
Erlangung des akademischen Grades
Doktor der Naturwissenschaften (Dr. rer. nat.)

der
Mathematisch-Naturwissenschaftlichen Fakultät

der

Universität Greifswald

vorgelegt von
Una Janke

Greifswald, Dezember 2020

Dekan: Prof. Dr. Gerald Kerth

1. Gutachter: Prof. Dr. Mihaela Delcea
2. Gutachter: Prof. Dr. Anisur Rahman

Tag der Promotion: 23.03.2021

“The blood is life…”

Bram Stoker, Roman *Dracula* (1897)

Table of Contents

Abstract

Blood platelets are primary major players in the coagulation cascade, that act upon damage in blood vessels at the subendothelial surface. During this process, platelets change their shape, release granules and aggregate by cross-linking of integrin αIIbβ3 *via* fibrinogen. The heterodimeric transmembrane receptor integrin αIIbβ3 is highly expressed on platelets and its regulation is bidirectional. *Inside-out signaling* leads to increased affinity for ligands due to dramatic rearrangements in the integrin conformation changing from an inactive bent conformation to an extended, high-affinity conformation. The swing-out motion of the integrin head domain enables binding of ligands, e.g. fibrinogen, resulting in *outside-in signaling* guiding kinase activation, shape change, platelet aggregation and spreading, subsequently.
Agonists (e.g. thrombin) and other triggers (e.g. shear stress) promote the activity of platelets, making the study of specific proteins delicate. Therefore, this PhD thesis describes a biomimetic system used to study αIIbβ3 membrane receptors. Integrin αIIbβ3 was successfully reconstituted into liposomes and characterized by biophysical and molecular biological methods (e.g. dynamic light scattering, transmission electron microscopy, circular dichroism spectroscopy and flow cytometry). The fusion of liposomes to a solid substrate allows the analysis of potential activation triggers and interaction partners concerning their role in integrin αIIbβ3 activation in a lipid bilayer. Among others, quartz-crystal microbalance measurements show that divalent ions and clinically relevant drugs (e.g. unfractionated heparin and quinine), known to be involved in immune thrombocytopenia (ITP), are certainly candidates which induce integrin activation and minor changes in protein secondary structure. In addition, protein corona formation during contact of nanoparticles with blood components, such as fibrinogen, as well as their interaction with artificial platelet model membranes containing integrins were studied. Moreover, lipid environment can be strongly controlled as integrin activation is dependent on the ratio of liquid-ordered and disordered phases within the membrane. Eventually, by exclusion of disturbances of complex external and internal factors, the established system enables the interaction analysis of various substances with receptors under physiological conditions. In contrast, these disturbances are required to understand the complex machinery of cellular processes *in vivo*. Hence, an expression platform, on the basis of HEK293 cells, was established to study not only the interaction of integrin αIIbβ3 with cytoskeletal networks, but also the impact of mutations on integrin resulting in a disease-like phenotype. Mutations known to induce Glanzmann thrombasthenia (GT) symptoms, were introduced and led to different mechanical properties of integrin-expressing cells, especially during cell adhesion cells. Thereby, generation of biological and medically-relevant processes combined with the biophysical setup contribute to understand disease mechanisms as well as the action of therapeutic agents in diseases such as GT and ITP.

Zusammenfassung

Blutplättchen sind die Hauptakteure in der Gerinnungskaskade, die auf Schäden in Blutgefäßen an der subendothelialen Oberfläche einwirken. Während dieses Prozesses ändern Blutplättchen ihre Form, setzen Granula frei und aggregieren durch Vernetzung des Integrins αIIbβ3 und Fibrinogen. Der heterodimere Transmembranrezeptor Integrin αIIbβ3 wird auf Blutplättchen exprimiert und seine Regulation ist bidirektional. *Inside-Out*-Signale führen zu einer erhöhten Affinität für Liganden aufgrund dramatischer Umlagerungen in der Integrin Konformation, die sich von einer inaktiven geschlossenen Konformation zu einer gestreckten Konformation mit hoher Affinität ändern. Die Ausschwenkbewegung der Integrin Kopfdomäne ermöglicht die Bindung von Liganden, z.B. Fibrinogen, was zur Aktivierung von Singalkaskaden, einer Blutplättchen Aggregation und einer anschließenden Ausbreitung führt. Agonisten (z. B. Thrombin) und andere Trigger (z. B. Scherbeanspruchung) fördern die Aktivität von Blutplättchen, wodurch die Untersuchung spezifischer Proteine schwierig wird. Diese Doktorarbeit zeigt ein biomimetisches System zur Untersuchung von αIIbβ3-Membranrezeptoren. Integrin αIIbβ3 wurde erfolgreich in Liposomen rekonstituiert und durch biophysikalische und molekularbiologische Verfahren (z. B. dynamische Lichtstreuung, Transmissionselektronenmikroskopie, Zirkulardichroismus-Spektroskopie und Durchflusszytometrie) charakterisiert. Die Fusion von Liposomen mit einem festen Substrat ermöglicht die Analyse potenzieller Aktivierungsauslöser und Interaktionspartner hinsichtlich ihrer Rolle bei der Aktivierung des Integrins αIIbβ3 in einer Lipiddoppelschicht. Quarzkristall-Mikrowaagen Messungen zeigen unter anderem, dass zweiwertige Ionen und klinisch relevante Arzneimittel (z. B. unfraktioniertes Heparin und Chinin), von denen bekannt ist, dass sie an der Immunthrombozytopenie (ITP) beteiligt sind, zweifellos Kandidaten sind, die eine Integrin-Aktivierung und geringfügige Änderungen der Proteinsekundärstruktur induzieren.

Darüber hinaus wurden die Bildung von Proteinkorona beim Kontakt von Nanopartikeln mit Blutbestandteilen wie Fibrinogen, sowie deren Wechselwirkung mit artifiziellen Integrin Thrombozyten-Modellmembranen untersucht. Darüber hinaus kann die Lipidumgebung gesteuert werden, da die Integrin-Aktivierung auch vom Verhältnis der geordneten und ungeordneten Phasen innerhalb der Membran abhängt. Unter Ausschluss von Störungen komplexer externer und interner Faktoren, ermöglicht das etablierte System schließlich die Interaktionsanalyse verschiedener Substanzen mit Rezeptoren unter physiologischen Bedingungen. Im Gegensatz dazu sind eben diese „Störungen“ erforderlich, um die komplexe Maschinerie zellulärer Prozesse *in vivo* zu verstehen. Daher wurde eine Expressionsplattform auf der Basis von HEK293-Zellen eingerichtet, um nicht nur die Wechselwirkung von Integrin αIIbβ3 mit dem Zytoskelett zu untersuchen, sondern auch den Einfluss von Mutationen des Integrins, was zu einem krankheitsähnlichen Phänotyp führt. Mutationen, von denen bekannt ist, dass sie Glanzmann-Thrombasthenie (GT)-Symptome induzieren, wurden eingebracht

und führten zu unterschiedlichen mechanischen Eigenschaften von Integrin-exprimierenden Zellen, insbesondere während der Zelladhäsion. Dadurch trägt die Erzeugung biologischer und medizinisch relevanter Prozesse in Kombination mit dem biophysikalischen Aufbau dazu bei, die Krankheitsmechanismen sowie die Wirkung von Therapeutika bei Krankheiten wie GT und ITP zu verstehen.

Contribution of Others

Within the scope of this PhD thesis, several students wrote their Master and Bachelor theses under my direct supervision in the Biophysical Chemistry group of Prof. Mihaela Delcea at the University of Greifswald.

Therefore, I would like to mention Theresa Brinker, that carried out most of the AFM measurements. In addition, Marco Harms, Alexandra Mitlehner and Aileen Weide established the integrin purification, as well as the new lipidic system protocols, while Sophie Möller contributed to the QCM-D experiments of nanoparticle-protein conjugates interacting with lipid membranes.

Furthermore, MDS studies were performed by Dr. Martin Kulke and Norman Geist. Dr. Ulrike Martens carried out the nanoparticle characterization and Dr. Peter Nestler prepared all AFM images of QCM sensor crystals. TEM images were taken under direction of Dr. Rabea Schlüter from the Imaging lab at the University of Greifswald.

List of Abbreviations

The commonly used abbreviations for chemical and physical units, amino acids and DNA bases are utilized.

αIIbβ3	Integrin αIIbβ3 or Glycoprotein IIbIIIa
ADP	Adenosine diphosphate
ADMIDAS	Adjacent site of MIDAS
AFM	Atomic force microscopy
AH	α-helical
Amp	Ampicillin
ATP	Adenosine triphosphate
AU	Absorbance unit
BCA	Bicinchoninic acid
BSA	Bovine serum albumin
CD	Circular Dichroism
CD41/61	Cluster of differentiation 41/61
CHAPS	3-[(3-Cholamidopropyl)-dimethylammonio]-1-propansulfonat
CIB1	Calcium- and integrin-binding protein 1
CMC	Critical micelle concentration
ConA	Concanavalin A
D	Dissipation (QCM-D)
DAG	Diacylglycerol
DC	Deformability cytometry
DLS	Dynamic light scattering
DMEM	Dulbecco´s modified eagles medium
DMPC	1,2-Dimyristoyl-sn-glycero-3-phosphocholine
DMPG	1,2-Dimyristoyl-sn-glycero-3-phospho-(1'-rac-glycerol)
DMSO	Dimethyl sulfoxide
DOPC	1,2-Dioleoyl-sn-Glycero-3-Phosphocholine
DTT	Dithiothreitol
E. coli	*Escherichia coli*
ECM	Extracellular matrix
EDTA	Ethylene diamine tetra acetic acid
e.g.	*exempli gratia*
EGF	Epidermal growth factor
ELISA	Enzyme-linked immunosorbent assay
Emmeans	estimated marginal means

ex/em	Excitation/Emission
f	Frequency (QCM-D)
FA	Focal adhesions
FACS	Fluorescence activated-cell sorting
FAK	Focal adhesion kinase
FCS	Fetal calf serum
Fb	Fibrinogen
FITC	Fluorescein isothiocyanate
FSC-A	Forward scatter-area
FSC-H	Forward scatter-height
g	Factor of earth acceleration
G-418	Geneticin 418
GDP	Guanosine diphosphate
GP	Glycoprotein
GT	Glanzmann thrombasthenia
GTP	Guanosine triphosphate
HEK293	Human embryonic kidney 293
HEPES	2-[4-(2-hydroxyethyl)-1-piperazine]-ethane sulfonic acid
HRP	Horseradish peroxidase
i.e.	*id est*
IgM/IgG	Immunoglobuline M/G
ITAM	Immune receptor tyrosine-based activation motif
LIBS	Ligand induced binding sites
LIMBS	ligand-induced metal binding site
LUV	large unilamellar vesicle
MES	2-(N-morpholino) ethane sulfonic acid
MIDAS	Metal ion dependent adhesion site
MLV	Multilamellar vesicle
NMR	Nuclear magnetic resonance
NP	Nanoparticle / Nonyl phenoxy polyethoxyl ethanol
OD	Optical density
Optiprep	Iodixanol 60 %
PAGE	Polyacrylamide gel electrophoresis
PAR1	Proteinase activated receptor 1
PBS	Phosphate buffer saline
PC	Phosphatidylcholine
PDB	Protein data bank

PDI	Polydispersive index
PE	Phosphatidylethanolamine
PI3K	Phosphoinositide 3-kinase
PKC	Protein kinase C
PMSF	Phenylmethylsulphonyl fluoride
PS	Phosphatidylserine
PSD	Position sensitive device
PSI	Plexin-Semaphorin-Integrin domain
PTB	Phospho-tyrosine binding
QCM-D	Quartz crystal microbalance with dissipation monitoring
Rho	Ras homolog gene
RT-DC	Real time-deformability cytometry
SDS	Sodium dodecyl sulfate
SEC	Size exclusion chromatography
SEM	Standard error of the mean
SM	Sphingomyelin (N-stearoyl-D-erythro-sphingosylphosphorylcholine)
SSC-A	Side scatter area
SUV	Small unilamellar vesicles
Syk	Spleen tyrosine kinase
SyMBS	Synergistic metal ion binding site
TBST	Tris buffed saline with tween-20
TC	Tissue culture
TEM	Transmission electron microscopy
TLC	Thin layer chromatography
Tris	2-Amino-2-(hydroxymethyl)-1,3-propanediol
TXA_2	Thromboxane A_2
ULV	Unilamellar vesicle
vWF	von Willebrand factor
WB	Western blot
WT	Wildtype
YM	Young’s Modulus

1. Introduction

1.1. Platelets and their role in health and disease

Blood platelets are playing the major role in hemostasis and thrombosis. These anucleated cells are produced by megakaryocytes in the bone marrow and circulate in the blood up to 10 days at high levels of 150-400 cells/µL whole blood until they are cleared in the liver and the spleen. Contact of platelets with extracellular matrix (ECM) induced by injuries of the vessel walls leads to a rapid adherence and aggregation resulting in clot formation, which prevents excessive bleeding (Gianazza et al. 2020). Platelet function needs to be balanced since non-functional clot formation causes bleeding disorders, whereas increased platelet reactivity leads to higher risk of thrombosis. Currently, many studies focus again on additional platelet qualities including inflammatory response in adaptive and innate immunity (Semple et al. 2011). In response to several stimuli, platelets change their shape and release their granules, which in turn, induces a signaling cascade activating more platelets, consequently. The different granules contain secretion products such as coagulation factors, chemokines, cytokines, prostaglandins and thromboxane A2. Among others, the fibrinogen receptor integrin αIIbβ3, also named glycoprotein (GP) IIb/IIIa, is activated and platelet aggregation is initiated (Ghoshal and Bhattacharyya 2014). Platelets are involved in a multitude of diseases including hemostatic disorders, but also in diseases that are only indirectly related to platelet function (e.g. atherothrombosis, diabetes mellitus, inflammatory diseases, cancer and neurological disorders) (Gianazza et al. 2020).

Together with thrombotic thrombocytopenic purpura, von Willebrand disease, Bernard-Soulier syndrome and Glanzmann thrombasthenia, immune thrombocytopenia (ITP) is one of the common platelet disorders (Krishnegowda and Rajashekaraiah 2015). In most ITP patients, autoantibodies target the platelet integrin αIIbβ3, which is followed by opsonization and clearance of platelets by the immune system. This leads to higher bleeding risk, consequently (Audia et al. 2017). The underlying mechanism is still unknown, although viral antigens and antigenic mimicry may play an important role. Additionally, ITP emerges as accompanying disease of autoimmune disorders, such as lupus erythematosus (Cines et al. 2009). Among acute ITP (which affects mostly children) and chronic ITP, other isoforms are known e.g. neonatal alloimmune thrombocytopenia, where maternal antibodies cross the placenta during pregnancy, bind fetal platelet antigens and induce severe thrombocytopenia (Audia et al. 2017). Moreover, clinically used drugs can induce antibodies directed to platelet antigens, or can decrease the platelet count and lastly, may cause thrombocytopenia. Potential drugs are e.g. ibuprofen, tamoxifen, but also the αIIbβ3 inhibitors tirofiban and eptifibatide, that induce antibodies directed to ligand-induced binding sites (LIBS) (Visentin and Liu 2007). The anti-malaria drug quinine, is also known as a drug that causes destruction of platelets by the immune system (Zhu et al. 2015).

The integrin αIIbβ3 is additionally responsible for the inherited bleeding deficiency Glanzmann thrombasthenia (GT) characterized by dysfunctional integrin or the complete absence of platelets caused by plenty of mutations in the genes encoding for both integrin subunits (Solh et al. 2015). Interestingly, some cases of acquired GT are characterized by the presence of antibodies that inhibit adhesive platelet function, without platelet destruction (Porcelijn et al. 2008).

1.2. Platelet activation

Platelet activation includes various signaling pathways and is a highly complex biological process illustrated in Figure 1. After exposure of ECM caused by injuries, platelet adhere *via* glycoprotein receptors, mainly GP VI and exposed von Willebrand factor (vWF)/collagen complexes leading to formation of a platelet monolayer. As a consequence, cells change their shape and release their content of alpha- and dense granules, including important clotting factors, as well as the platelet agonists thrombin, thromboxane A_2, adenosine diphosphate (ADP) and prostaglandin E2. Platelet activation induced by glycoproteins is mediated by immunoreceptor tyrosine-based activation motif signaling, whereas stimulation through agonists includes G-protein-coupled receptors.

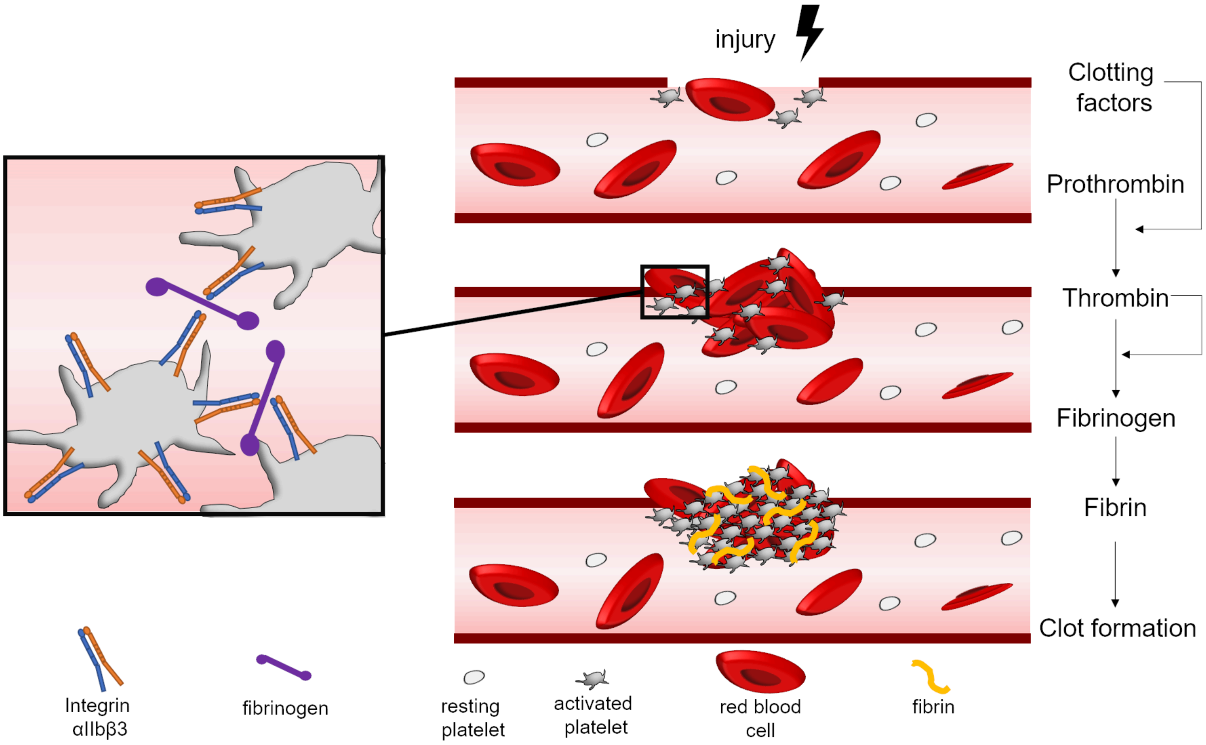

Figure 1: Schematic illustration of clot formation. Upon injury, platelets and red blood cells bind to the ECM and are activated leading to release of clotting factors. In turn, these induce the coagulation cascade resulting in thrombin and fibrin formation among others. A stable clot is formed by activated platelets that aggregate and connect *via* activated integrin αIIbβ3 bridged with fibrinogen. Adapted from (Versteeg et al. 2013)

Agonist-initiated platelet activation signaling, e.g. by cleavage of protease-activated receptors (PAR) by thrombin, starts with activation of phospholipase C, which leads downstream to increased cytosolic Ca^{2+} ion concentration. As a consequence, the guanosine triphosphate (GTP)-binding protein Rap1 is activated and initiates the binding of talin-1 to the cytoplasmatic domain of integrin αIIbβ3. This integrin makes the platelet-platelet adhesion over fibrinogen or vWF cross-linking feasible and plays a crucial role in aggregation as well as thrombus formation. After binding of talin-1 and kindlin-3, αIIbβ3 receptor is upregulated and its activation is induced. Due to the conformational shift, binding of its ligands is possible (Michelson et al. 2019; Yun et al. 2016). Typical ligands include fibrinogen, fibrin, von Willebrand factor, fibronectin, vitronectin and thrombospondin-1. Many of these molecules contain a short RGD motif, which is the main peptide sequence recognized by αIIbβ3. However, αIIbβ3 binds also to other binding sites, e.g. the KQAGDV sequence in the γ-chain of fibrinogen (Durrant et al. 2017; Huang et al. 2019). The detailed activation of αIIbβ3 is described in Chapter 1.5.3.

Another important progress during hemostasis is the initiation of the coagulation cascade, which ultimately leads to fibrin formation. Factor VII is released by damaged blood vessels and forms a complex with tissue factors, which in turn, leads to the initiation of the activation of various factors resulting in thrombin and other feedback loop activation. Thrombin is a serine protease which causes fibrinogen conversion to fibrin to form a stable mesh around the platelet clot (Figure 1). Simultaneously, negative regulatory control mechanisms are initiated e.g. by inhibitors like antithrombin (Versteeg et al. 2013).

1.3. Platelet mechanics and cytoskeleton

Upon injury, the platelet clot is a highly active material with a hierarchical structure. Fully activated platelets form a compact core, whereas decreasingly less activated platelets are in the outer shell due to an agonist concentration gradient rising from the inner core regulating additionally the packing density. Platelets play a major role in regulation of forces and contraction within the clot. Due to their contractive forces, stiffness of the clot increases significantly and platelet-derived filopodia can remodel the fibrin mesh (Williams et al. 2019; Lam et al. 2011). The cytoskeletal morphologies and shape changes upon clot formation involve complex signaling pathways and proteins such as αIIbβ3 receptor, resulting in actin remodeling.

However, platelets not only function as an executer, they are also highly sensitive mechanosensors. They directly respond to the stiffness of their surroundings, which impacts adhesion, aggregation and activation of the cells. Studies show that platelets respond to immobilized, but not to soluble fibrinogen by integrin tension regulation (Zhang et al. 2018). Spreading of platelets on fibrinogen show, among various F-actin bundles, contractile stress fibers and thus, cytoskeletal rearrangements (Burridge and Wittchen 2013). Interestingly, studies with platelets from patients suffering from Glanzmann thrombasthenia show significantly rounder shaped cells and reduced cytoskeletal remodeling (Lickert et al. 2018). This indicates already the important role of integrin αIIbβ3 in platelet mechanics.

Integrins and associated proteins build highly dynamic structures, the cell-matrix adhesions, such as focal complexes, focal adhesions, fibrillary adhesions and podosomes. These structures are characterized by the linkage of actin to the membrane resulting in places of mechanotransduction by connection of ECM and cytoskeleton. Basically, such places, called focal complexes, are initiated by the clustering of integrins. The latter evolve into stable focal adhesions by either intracellular contractive machinery mediated by actomyosin or extracellular-derived forces. The assembly of focal adhesions is mainly regulated by tyrosin phosphorylation by e.g. Src kinases, focal adhesion kinase and phosphoinositid-3-kinase. Typical proteins in focal adhesions are talin and tyrosine-phosphorylated proteins, that directly link integrin and actin, but more than 50 other molecules with various functions are involved, such as paxillin, Rho and vinculin (Geiger et al. 2001).

The fundamental process of shape change, upon the contractile event during platelet activation, transmigrates from discoid shape, over spherical and slightly smaller cells right up to formation of pseudopodia and lamellipodia. Fully spreading of platelets involves a radical rise in polymerized actin. Unstimulated platelets contain only 40-50 % actin filaments (F-actin), which escalate to 70 % after thrombin-induced stimulation. An essential molecule upon that process is the Arp 2/3 complex, which induces the pointed-end nucleation activity of actin filaments and causes branched polymers, consequently. Typical actin structures in activated platelets are filopodia, lamellipodia, stress-like fibers and the contractile ring (Figure 2), (Bearer et al. 2002).

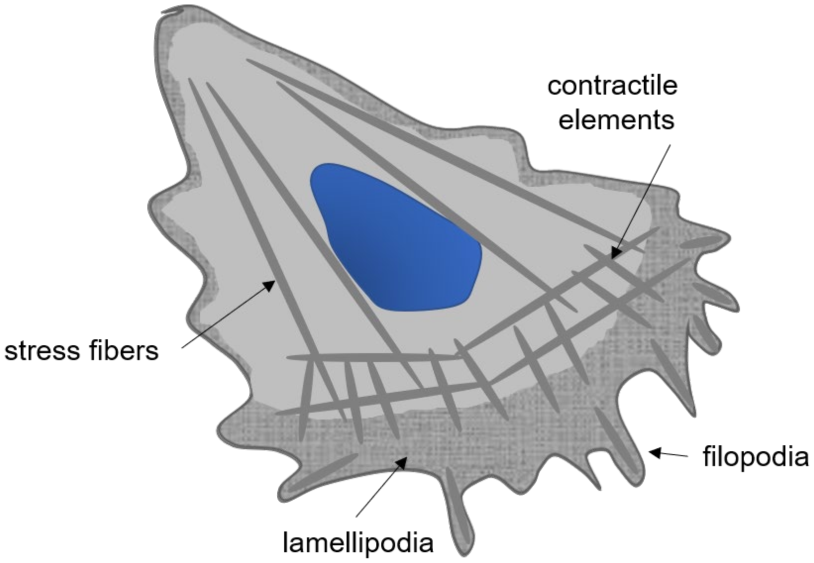

Figure 2: Actin structures in activated cells/platelets. Schematic illustration of different actin structures showing stress fibers, lamellipodia, filopodia and contractile elements forming a contractile ring in activated platelets. Adapted from (Blanchoin et al. 2014)

1.4. Platelet membranes and lipids

Upon activation of platelets, major remodeling of lipids occurs leading to structural changes of the platelet membrane as in spreading and degranulation. Additionally, lipids play a major role in signaling events. The platelet membrane contains different types of molecules ranging from cholesterol to sphingomyelins. For this reason, lipids and their characteristics are described in detail.

Lipids are hydrophobic, amphipathic molecules consisting of non-polar fatty acid chains and a polar head group, which are connected by either glycerol (glycerolipids) or sphingosine (sphingolipids). Fatty acids can be saturated or unsaturated comprising various amounts of double bounds (Yeagle 2016). Following these characteristics, there are different families of lipids in platelets, that can be separated by their functional head groups, such as phospholipids, sphingolipids, steroids, but also by other structural differences such as fatty acid chain length and saturation.

The main lipids in platelets are phospholipids, the headgroup of which contains phosphate. Due to their amphipathic characteristics, lipids are forming a self-assembled lipid bilayer with hydrophobic fatty acid chains in the core and the hydrophobic head groups directed towards the aqueous phase (Figure 3A). Multiple shapes can be formed due to the hydrophobic effect, such as planar bilayers, micelles, hexagonal phases, but mostly bilayers (Yeagle 2016). In superior animals and plants, choline, serine, glycerol and ethanolamine are the most abundant head groups of phospholipids, as depicted in Figure 3B.

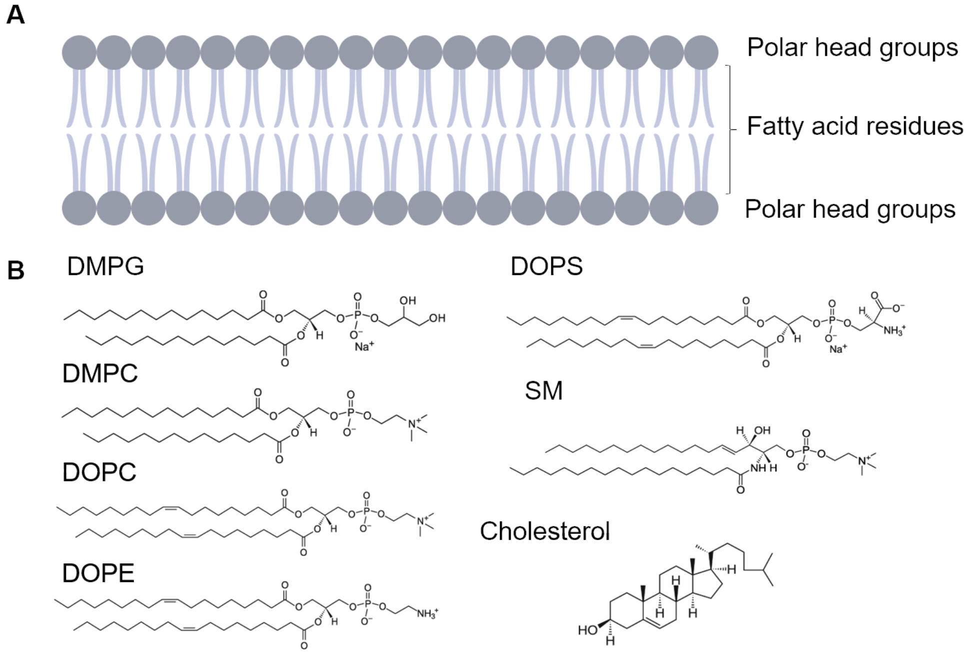

Figure 3: Schematic representation of lipid membrane and chemical structures of lipids. A) Lipid membrane with hydrophobic fatty acid residues and polar head groups. B) Chemical structure of lipids used in this work: DMPG (1,2-dimyristoyl-sn-glycero-3-phospho-glycerol), DMPC (1,2-dimyristoyl-sn-glycero-3-phosphocholine), DOPC (1,2-dioleoyl-sn-glycero-3-phosphocholine), DOPE (1,2-dioleoyl-sn-glycero-3-phosphoethanolamine), DOPS (1,2-dioleoyl-sn-glycero-3-phospho-L-serine), SM (Sphingomyelin), cholesterol. Structures were created with Chemsketch.

Another major membrane component within the lipids are the sphingolipids, such as sphingomyelin (SM). Together with cholesterol, SM are the main elements of lipid rafts, that are enriched specialized signaling areas (Yeagle 2016). Cholesterol belongs to sterols group and has a rigid hydrocarbon skeleton with one hydroxyl group (Figure 3B). Cholesterol increases both membrane stability and permeability. It arranges within the gaps between the different fatty acid chains in the membrane. At exceedingly disordered region, as well as high temperatures, cholesterol promotes membrane rigidity. However, in ordered membrane areas or low temperatures cholesterol weakens the cohesive forces between the fatty acid residues and mediates destabilization (Lee 2011; Kaiser et al. 2009; Brügger 2014).

The thermodynamic phases, also called gel phase (disordered) and liquid crystalline (ordered) phase, are affected by increasing fatty acid tail lengths and the number of double bounds, which reflects characteristic transition temperatures (T_m). Due to this fact, lateral diffusion of lipids within the membrane (which is generally in fluid phase in a range of 1 $\mu m^2/s$) can be controlled (Sunshine and Iruela-Arispe 2017). Additionally, an exchange of lipids within the two leaflets is slower and depends on the nature of head group, temperature, and fatty acid chain length (Berg et al. 2002). In this PhD thesis, 1,2-dimyristoyl-sn-glycero-3-phosphocholine (DMPC), 1,2-dimyristoyl-sn-glycero-3-phospho-glycerol (DMPG), 1,2-dioleoyl-sn-glycero-3-phosphocholine (DOPC), SM (Sphingomyelin) and cholesterol were used as representative lipids for biomimetic studies.

Membranes allow rotational, translational and trans-bilayer movement of lipids within the membrane, which affects asymmetry. In platelet membranes, the cytosolic leaflet contains phosphatidylethanolamine (28 %) and phosphatidylserine (10 %), while the external leaflet contains mainly sphingolipids (18 %) and phosphatidylcholine (40 %) (Figure 4). Moreover, membrane fluidity is maintained by integrated cholesterol (O'Donnell et al. 2014; Sunshine and Iruela-Arispe 2017). Platelet membranes consist of sphingomyelins and cholesterol that are enriched in specific domains (Figure 4) characterized by liquid-ordered instead of liquid-disordered phases, namely lipid rafts (Kaiser et al. 2009).

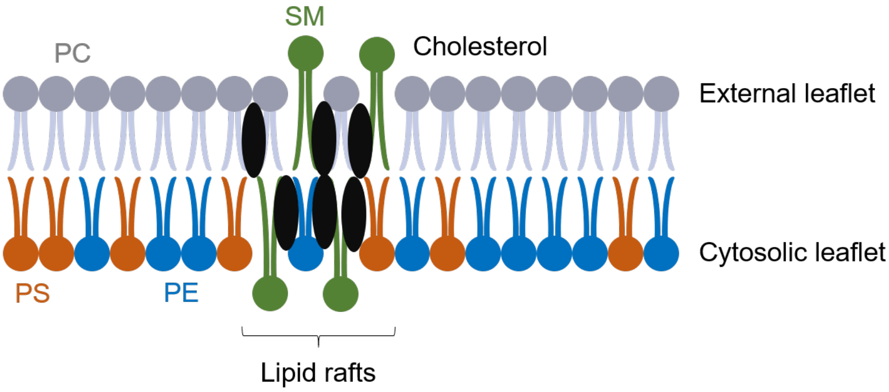

Figure 4:Lipid distribution in the platelet membrane. The outer leaflet of the membrane comprises mainly PC (in grey) and the inner leaflet PS (in orange) and PE (in blue). SM (in green) and cholesterol (in black) are enriched in specific signaling domains, called lipid rafts.

Upon platelet activation, the membrane provides substrates for different enzyme reactions converting lipids, consequently. This rearrangement contributes to the change in platelet shape and the generation of prothrombotic substances, e.g. prostaglandins, phosphatidylinositides and diacylglycerol. Additionally, conversion of lipids results in rising amount of phosphatidylserine or phosphatidyl-ethanolamine in the external leaflet. Therefore, Ca^{2+} influx is preserved and ions accumulate at the negatively charged membrane. Consequently, scramblases are stabilized and promote coagulation by phospholipid rearrangements (Williamson 2015; O'Donnell et al. 2014). Because integrins and also lipid composition, play a major role in platelet activation, it is clear that lipid rafts present a key role in integrin function. For instance, the lymphocyte integrins LFA-1 and α4β1 are recruited to lipid rafts upon T-cell stimulation (Leitinger and Hogg 2002). In addition, the lateral organization of the plasma membrane and its raft domains are associated with actin filamentous structures, which can be inhibited by blocking of αIIbβ3. However, no integrin αIIbβ3 was detected in rafts after platelet activation (Bodin et al. 2005).

1.5. The platelet integrin αIIbβ3

1.5.1. Integrins

Integrins are transmembrane receptors in vertebrates encoded by two genes in humans on chromosome 17. They are responsible for a variety of unique functions depending on the type of integrin. The most important function is the regulation of cell-cell and cell-ECM interaction and therefore, cell adhesion as well as other physiological cell processes such as cell migration, cell recruitment, tissue anchoring, inflammatory responses and cell aggregation (Hughes 2001; Ye et al. 2012).

Integrins are heterodimeric bidirectional receptors composed of two non-covalently bound subunits, namely α- and β-subunit. There are 18 α- und 8 β-subunits known, that could form up to 24 different receptors with various purposes and distributions within the body. Each subunit has one helical transmembrane domain and an unstructured short cytoplasmatic part, that is important for integrin activation. The large extracellular fragment, containing the head domain formed by both subunits, undergoes dramatic rearrangements upon integrin activation, pointing the N-terminus towards the extracellular space (Campbell and Humphries 2011; Michelson et al. 2019). The variety of integrin ligands indicates several different signaling pathways. Most intracellular ligands are binding to the cytoplasmic tail of the β-subunit, which enables to categorize the integrins evolutionary. β1, β2 and β7 integrins represent two thirds of all integrins with loss of these integrins leading to severe effects, e.g. immunodeficiency and neurological disorders. β3, β5, β6 and β8 integrins are arginine-glycine-aspartate (RGD) motif receptors, with ligands such as collagen, laminin or fibrinogen. β4 integrins have a different cytoplasmic domain and are only associated with the α6-subunit (Hughes 2001).

Only two integrins are formed with the β3-subunit, αIIbβ3 and αVβ3, which are both expressed in platelets, while αVβ3 is additionally present in e.g. leukocytes, endothelial and cancer cells. Platelets retain vascular integrity and prevent life-threatening blood loss. The possibility of clot formation upon injury, is strongly dependent on the capability to aggregate. This is mediated by integrin αIIbβ3, which is the most abundant platelet receptor with 80,000 copies per cell representing 17% of total protein mass in the platelet membrane. Both subunits are glycosylated polypeptide chains. After post-translational processing of the αIIb-subunit into a heavy and a light chain linked by a disulfide bridge in the Golgi-apparatus, the 235 kDa protein translocates to the membrane. Generally, all integrins undergo transition from a low affinity state (bent, resting state) to a high-affinity state (active, extended) (Michelson et al. 2019; Bennett 2005; Campbell and Humphries 2011).

1.5.2. Structure of αIIbβ3

The overall structure of platelet integrin αIIbβ3 is depicted in Figure 5A. The extracellular domain of the αIIb-subunit contains a seven-bladed β-propeller, that could bind four divalent ions providing stability to the interface through the thigh domain. The latter is followed by calf1- and calf 2-domains, that are giving rigidity due to the large hydrophobic interface. The leg domain contains two flexible areas, where the one between thigh and calf domain serves as a "knee" region. The β3 extracellular domain comprises an A-domain with six β-sheets encircled by 8 α-helices (Figure 5B). Additionally, this domain contains three metal-ion binding sites: the metal-ion dependent adhesion site (MIDAS), the adjacent to MIDAS (ADMIDAS) and a ligand-induced binding site also named as synergistic metal ions binding site (SyMBS). The A-domain forms a large interface with the hybrid domain containing both hydrophilic and hydrophobic residues. The plexin-semaphorin-integrin (PSI)-domain connects the hybrid domain with four epidermal growth factor (EGF) like-domains, that contain flexible regions between the individual parts and are cysteine-rich, but all 56 cysteines form disulfide bonds. A conformational change and the flexibility of the legs cause a movement of the α7-helix in the A-domain towards the hybrid domain, which leads to a swing-out motion of the hybrid domain upon activation of integrin (Figure 5B; transition from yellow to orange). The extracellular β3 leg-domain finishs with a β-tail proximal to the membrane (Michelson et al. 2019; Campbell and Humphries 2011; Bennett 2005).

Both subunits creating an interface between the β-propeller of the α-subunit and the A-domain within the β-subunit. This forms, according to electron microscopy (EM) (Dai et al. 2015) and cryo-EM (Adair and Yeager 2002; Xu et al. 2016), a globular head domain, whereas the other parts display the stalk domains.

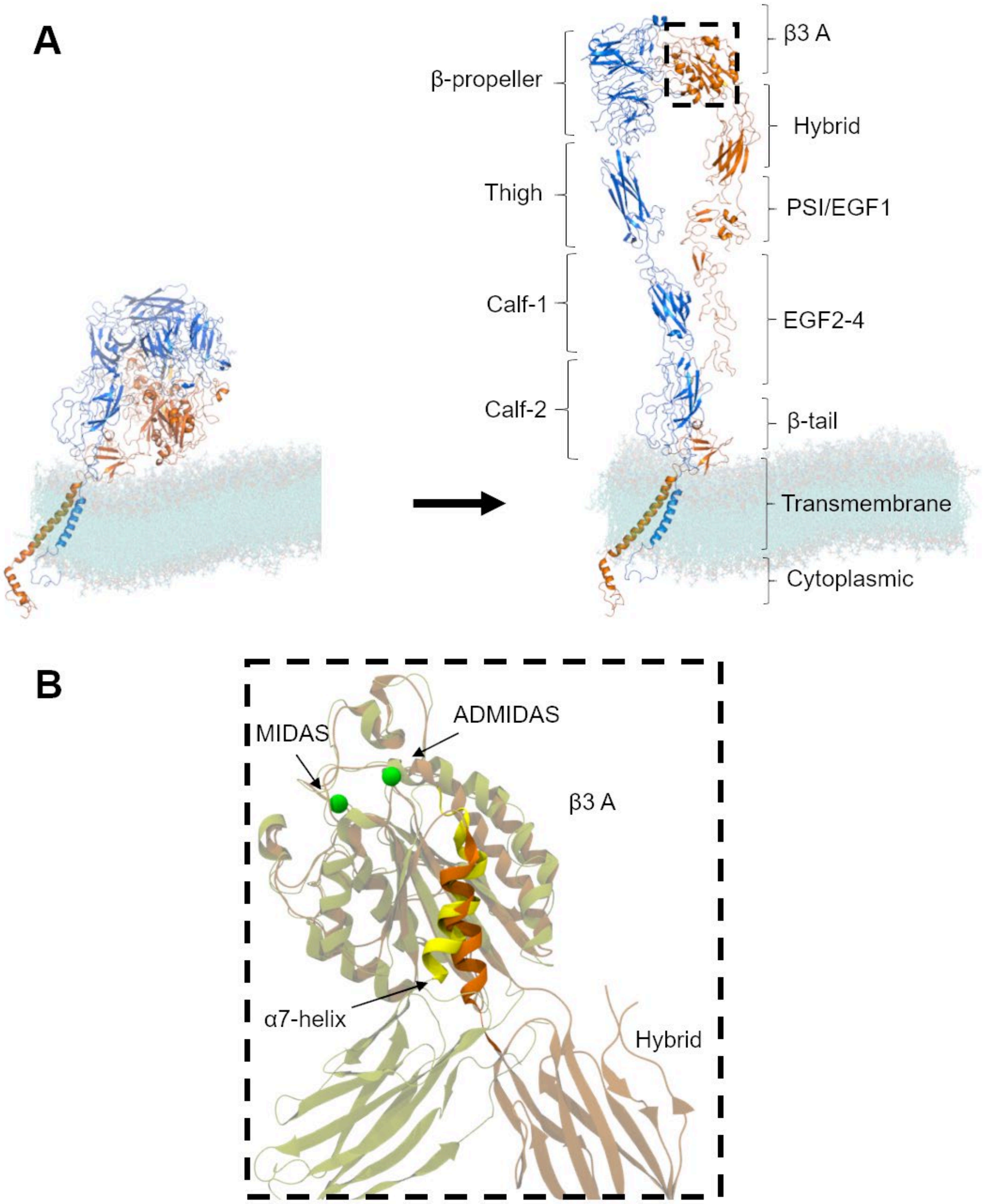

Figure 5: Integrin αIIbβ3 structure. A) Structure of αIIbβ3 in closed (left) and open/active (right) conformation in a DMPG:DMPC (1:20) lipid membrane (cyan). αIIb-subunit is depicted in blue and β3-subunit in orange. Picture combines the structure from PDB-code 2k9j and ectodomain (PDB-code 3fcs), missing residues were added as random coils. Adapted from (Janke et al. 2019). B) Close-up view of the ligand-occupied β3 A-and hybrid-domain from PDB-code 2vdr (orange) aligned with A-domain from closed conformation (yellow; PDB-code 3fcs). Ca^{2+} (green) are located in the MIDAS and ADMIDAS. Swing-out motion of the hybrid domain is shown due to movement of the α7-helix upon integrin activation.

The transmembrane domains of both subunits are mostly α-helices that cross at a 25-30° angle. These regions contain mostly hydrophobic amino acids, especially a GFFKR (glycine-phenylalanine-phenylalanine-lysin-arginine) sequence serving as a crucial binding site for various intracellular regulator proteins. Transmitting of signals upon the different conformations initiated through this sequence seems to be important for maintaining integrin inactive (Kim et al. 2011; Michelson et al. 2019). Additionally, there are electrostatic interactions between the two helices in the transmembrane domains of both subunits upon resting state, that are destructed in active conformation (Ma et al. 2007). Therefore, the transmembrane domains play an essential role in transmission of signals across the membrane.

The cytoplasmatic tails of αIIbβ3 are characterized by α-helices, but mostly unstructured domains. In the absence of interaction partners, they are flexible and transient structures, whereby both subunits interact with each other through their membrane proximal regions by electrostatic and hydrophobic interactions. The β3-tail contains a NPLY and a NITY recognition motif that induce binding of talin-1 and kindlin-3 *via* their PTB (phosphotyrosine binding)-domain (Michelson et al. 2019). The talin head region associates with the β-tail, but whole protein has also additional binding sites for actin and vinculin, which serves as a mechanical link between integrin and the cytoskeleton. Moreover, talin faces the membrane by its positively charged residues, which promotes the dissociation of the integrin cytoplasmatic tails by breaking the salt bridge between αIIb- and β3-subunit and changes the angle of the transmembrane domains, consequently (Kim et al. 2011). With the help of kindlin, talin induces integrin activation and serves as a force sensor, as well as integrin affinity regulator (Sun et al. 2019).

1.5.3. Activation and function of αIIbβ3

Integrin αIIbβ3 exists in at least three conformational states: i) the bent conformation with the head domain pointing towards the membrane, ii) the extended conformation but closed head, and iii) the extended conformation with open head domain, which correspond to low-, intermediate, and high affinity states, respectively (Xu et al. 2016).

Inside-out activation

Activation process is achieved by two ways: i) receptor clustering and lateral movement, which increases the avidity of ligand interactions, and ii) induction of conformational changes in both subunits of the integrin increasing the ligand affinity. This requires a mechanism that converts signals from the intracellular space through the membrane and a large distance (~20 nm), which extends the extracellular domain of the integrin, consequently. The procedure, called inside-out signaling, is initiated by multiple stimuli that work synergistically such as: agonist binding to platelet receptors, e.g. protease-activated receptor 1 (PAR1), cell adhesion and shear stress. In turn, diacylglycerol (DAG) is activated and intracellular Ca^{2+} concentration arises, which activates Rap1, a small GTPase, and the protease calpain that cleaves talin-1 (Michelson et al. 2019). The latter consist of a 50 kDa head and a 220 kDa rod-domain. Talin binds to the cytoplasmic tail of the β3-subunit and displace the αIIb-subunit away by binding to the membrane proximal region. Kindlin-3 is significant for integrin activation and supports activation by talin (Sun et al. 2019). The separation of the two subunits transmits the signal through the transmembrane domains and this in turn, provides the driving force to trigger the reversible conformational change in the extracellular domain. As a consequence, swing-out motion of the hybrid domain causes opening of the integrin head domain (switchblade-model), which is presented in Figure 5B. The platelet integrin conformation equilibrium changes towards the high-affinity state and ligand binding is feasible (Ma et al. 2007; Kim et al. 2011; Campbell and Humphries 2011). However, some studies predicting the so-called deadbolt-model, where integrin stays in the bent conformation even upon ligand binding (Adair et al. 2005). Among the fact that talin connects integrin with the actin cytoskeleton, the degranulation of actin polymers leads to a reduction of the tensile force and a reassociation of the subunits as well as ligand dissociation, consequently (Michelson et al. 2019). The inside-out activation is depicted schematically in Figure 6.

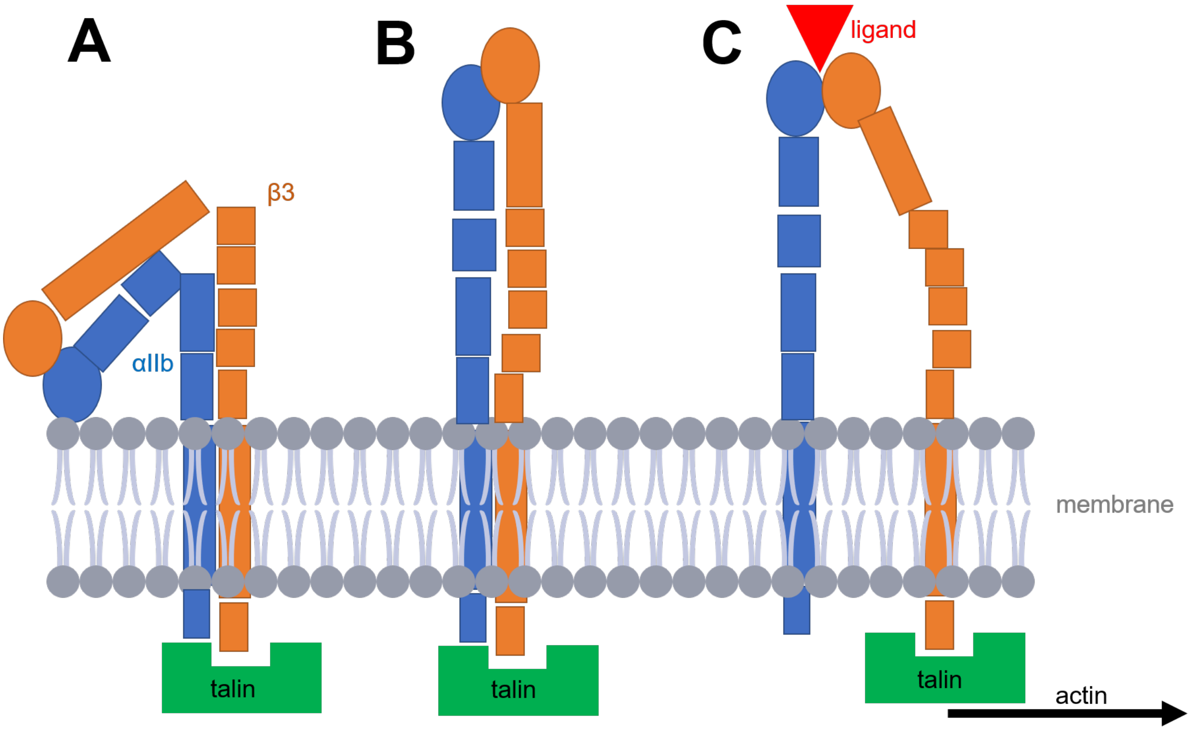

Figure 6: Inside-out activation of integrin αIIbβ3. Platelets are activated and downstream of the activation cascade talin-1 is activated. Talin-1 binds to the cytoplasmatic tail of the β3-subunit (orange) and brings the bent (A) conformation of αIIbβ3 to the extended conformation (B). Ligand binding is possible leading to the ligand-occupied active conformation (C), is able to trigger further signaling cascades and can function as a mechano-sensor with the help of actin.

Ligand binding

Typical ligands of αIIbβ3 are fibrinogen, fibrin, vWF and fibronectin, but their binding to integrin requires divalent ions. Most ligands contain an RGD motif or additional binding motifs, as in the γ-chain of fibrinogen which contains the KQAGDV motif. RGD binds the interface of the β3 A-domain and the αIIb β-propeller, whereby the acidic residues coordinate the divalent cation. Fibrinogen is a major αIIbβ3 ligand and consists of Aα, Bβ and γ chains formed into three nodular domains. It intermediates integrin-integrin interaction and thus, promotes platelet aggregation. Upon ligand binding, ligand-induced binding sites can be exposed and can induce neoepitopes (i.e. new antibody-binding sites) being a cause of ITP (Bennett 2005; Campbell and Humphries 2011). Bhoria et al. used the conformation-specific antibody PAC-1, which exclusively recognizes the active state of integrin αIIbβ3, and observed binding to platelets from patients suffering from ITP and thus, suggested that integrin αIIbβ3 exists in an active state upon circulation (Bhoria et al. 2015). PAC-1 binds at the fibrinogen binding site formed by the head domain (Taub et al. 1989). Other ligands, specifically several clinically used drugs, are able to bind to αIIbβ3 and could induce conformational changes and even secondary drug-induced autoantibodies. Potential candidates are αIIbβ3 inhibitors such as tirofiban, eptifibatide or abciximab, but also the anti-malaria drug quinine (Visentin and Liu 2007). In addition, the anticoagulant unfractionated heparin (UFH) is able to induce platelet aggregation and αIIbβ3 affinity changes (Xiao and Théroux 1998; Yagi et al. 2012; Gao et al. 2011). Interestingly, also low-molecular weight heparins can affect integrin outside-in signaling, induce conformational changes and platelet activation, which can be blocked by αIIbβ3 antagonists (Hashemzadeh et al. 2008).

Outside-in signaling

The outside-in signaling initiates complex pathways that act as a signal transducer to the cell cytoplasm causing multiple cellular responses ranging from platelet spreading, clot formation, cytoskeletal rearrangements and force sensing. The key players are members of the Src-family and Syk kinases that are activated by tyrosine phosphorylation, as it is the case for various proteins as well as the β3-tail. Downstream of the mentioned kinases phospholipase C, focal adhesion kinase and protein kinase C are activated. Moreover calcium- and integrin-binding protein 1 binds to the αIIb cytoplasmic tail and acts, among others as a negative regulator. It should also be mentioned that Rho GTPase and Arp2/3 complex are part of the actin machinery (Durrant et al. 2017).

1.5.4. The role of divalent cations in integrin activation

In the human blood, 1 mM Ca^{2+} and 1 mM Mg^{2+} concentrations are observed that keep the integrin in an inactive state and stabilize its structure. Intracellularly, integrins are activated through inside-out activation by talin inducing the switchblade opening resulting in extension of the head domain away from the plasma membrane. The equilibrium of the cell surface integrins can be shifted by various stimuli, such as metal ions (Michelson et al. 2019).

There are several cation binding-sites throughout the integrin. The β-propeller of the αIIb-subunit employs four divalent ion binding sites that are within the blades and coordinated aspartic acid and asparagine residues giving rigidity to the structure. Mutagenesis analyses show their importance for ligand recognition and heterodimer formation in integrin biogenesis (Zhang and Chen 2012; Campbell and Humphries 2011). An additional Ca^{2+} binding site is located at the “knee” between thigh and calf-1 domain, formed by highly acidic amino acids and stabilizes the structure in both bent and extended conformation. Additionally, β3-subunit A-domain consists of a metal ion cluster that consists of three metal ion binding sites. At the center is the metal ion-dependent adhesion site (MIDAS), which is coordinated by Asp119, Ser121, Ser123, Glu220 and Asp251. This region is responsible for signals from the integrin head to other integrin domains and crucial for ligand binding, especially RGD-containing ligands (Michelson et al. 2019; Zhang and Chen 2012). The MIDAS is flanked by two other metal ion binding sites: the ADMIDAS and the SyMBS. Together with MIDAS, these regions in the α7 helix support swing-out motion of the hybrid domain resulting in the transition from low to a high-affinity state (Figure 5B). ADMIDAS inhibits the activation at high Ca^{2+} levels, whereas Mn^{2+} compete with Ca^{2+} and increases ligand binding. Similarly, the SyMBS is a positive regulator for increased ligand affinity (Michelson et al. 2019; Campbell and Humphries 2011). Exogenously, integrins can be activated by specific antibodies, reducing agents and divalent ions. Mn^{2+} increases the affinity to fibronectin of all β1-and β3-integrins. Almost all integrins show an increased ligand affinity upon removal of Ca^{2+} but rise of Mn^{2+}. Generally, Mn^{2+} and Mg^{2+} supports ligand binding while Ca^{2+} inhibits binding. The affinities of the respective ions to the metal ion binding sites are $Mn^{2+}>Mg^{2+}>Ca^{2+}$. The non-physiological stimulus of Mn^{2+} shifts the conformation equilibrium towards the active form. However, various experiments ranging from studies with liposomes (Ye et al. 2008), FRET (Förster Resonance Energy Transfer) (Zhang and Chen 2012) to cryo-EM (Ye et al. 2012) show controversial results concerning the question, whether Mn^{2+} leads in fact to increased ligand affinity, but no maximal extension.

1.6. Biomimetic membrane systems

1.6.1. Model membranes

Biological membranes play a crucial role in life, display a site of communication and a barrier between the inside and the outside of the cell. Many groundbreaking findings were achieved over the past century, starting in 1916 with the study of surface chemistry by Langmuir (Langmuir 1916), continuing with the discovery of the cell membrane by Gorter and Grendel (Gorter and Grendel 1925), followed by the ultrastructure of a bilayer (Robertson 1959) and the fluid mosaic model of cell membranes by Singer and Nicolson in the 70’s (Singer and Nicolson 1972).

The design of biomimetic surfaces and the construction of model membranes enable the elucidation of the basic principles of membrane biophysics. The investigation of membrane proteins *in vivo* is impaired by multiple associated proteins and signaling pathways that might interfere (Zhao and Lappalainen 2012). To study individual embedded proteins and their activity, several biomimetic model membranes are suitable and allow the investigation under physiological conditions. Transmembrane proteins conformation and activity can be modulated by the lipid composition, e.g. hydrophilic and hydrophobic properties. Therefore, creation of appropriate model membranes requires optimization to retain protein stability and activity.

Various model membranes were studied in the past. First, Langmuir monolayers should be mentioned, where lipids self-assemble at the air-water interface. With this technique, surface pressure, thickness and area can be controlled, but bilayer formation is only possible *via* transfer to a solid substrate in air. Second, the formation of liposomes, a self-closed lipid bilayer, can easily be formed by extrusion and sonication techniques. Protein reconstitution requires detergents, that are forming phospholipid-protein-detergents mixtures. Detergents are then slowly removed by dialysis, gel filtration or biobeads adsorption. Upon reaching the lipid critical micelle concentration (CMC), the protein will spontaneously interact with the lipid membrane and create proteoliposomes. Unfortunately, final orientation of the reconstituted protein is only subject to limited control (Shen et al. 2013).

By vesicle fusion on hydrophilic supports due to van-der-Waals, electrostatic, hydration and steric forces, supported lipid bilayers (SLB) are formed. Hence, numerous processes are possible when liposomes meet a surface. Adsorption alone could already deform the membrane leading to formation of bilayer disks. This deformation could be also induced by neighboring vesicles, that fuse and rupture. Additionally, these patches could encourage more vesicle fusion. These events are dependent on membrane-surface, intermembrane and intra-membrane forces. Moreover, factors such as surface charge and roughness as well as vesicle composition, concentration, charge and environmental conditions (pH, osmotic pressure, temperature and ionic strength) play a critical role (Richter et al. 2006; Hardy et al. 2013).

However, in SLB formation one side of the hydrophilic head groups are tightly attached to the surface, which affects the fluidity and orientation of the protein. Hence, tethered polymer SLB systems were developed, e.g. with polyethylene glycol (PEG), creating space between protein/membrane and support (Jackman et al. 2012). Lastly, nanodiscs shall be mentioned, which make the study of individual particles and activity assays feasible. They are characterized by self-assembly of lipids, that are surrounded by a membrane scaffold protein. Such studies were already performed with various membrane proteins, e.g. G-protein coupled receptors (Leitz et al. 2006), cytochrome molecules (Davydov et al. 2005) and insulin receptor (Gutmann et al. 2020).

1.6.2. Liposomes

Liposomes are vesicles consisting of one or more concentric bilayers enclosing aqueous solution, which are presented as multilamellar vesicles (MLV) or unilamellar vesicles (ULV). Further subgroups can be formed into small, large and giant ULV (Dimova 2019).

The reconstitution system strongly influences the activity of proteins. Thus, reconstitution protocols require optimization. For integrin αIIbβ3, numerous studies were carried out using liposomes (Ye et al. 2010), nanodiscs (Choi et al. 2013) and lipid bilayers (Frohnmayer et al.

2015). This PhD thesis focuses on protein reconstitution into liposomes. Basically, the production of proteoliposomes is carried out by addition of detergents, followed by their slow removal *via* addition of biobeads or extensive dialysis. There are several studies with liposomes and reconstituted integrin molecules using lipids such as DMPC, DMPG (Erb and Engel 2000), egg PC, PS (Ye et al. 2012), DOPC, 1,2-dipalmitoyl-sn-glycero-3-phosphocholine (DPPC) and cholesterol (Ge et al. 2018).

Since 1960, liposomes find an application in nanomedicine, especially cancer therapy, due to their improved bioavailability, decreased toxicity, increased circulation time, a targeted controlled release of their core content, stability of drugs and enhanced solubility (Bozzuto and Molinari 2015). Additionally, the amphiphilic phospholipid bilayer represents similarities to the mammalian membrane, which improves cellular uptake in drug delivery systems. Encapsulated hydrophobic or hydrophilic drugs are targeted released and properties of liposomes can be easily controlled and modified (Figure 7).

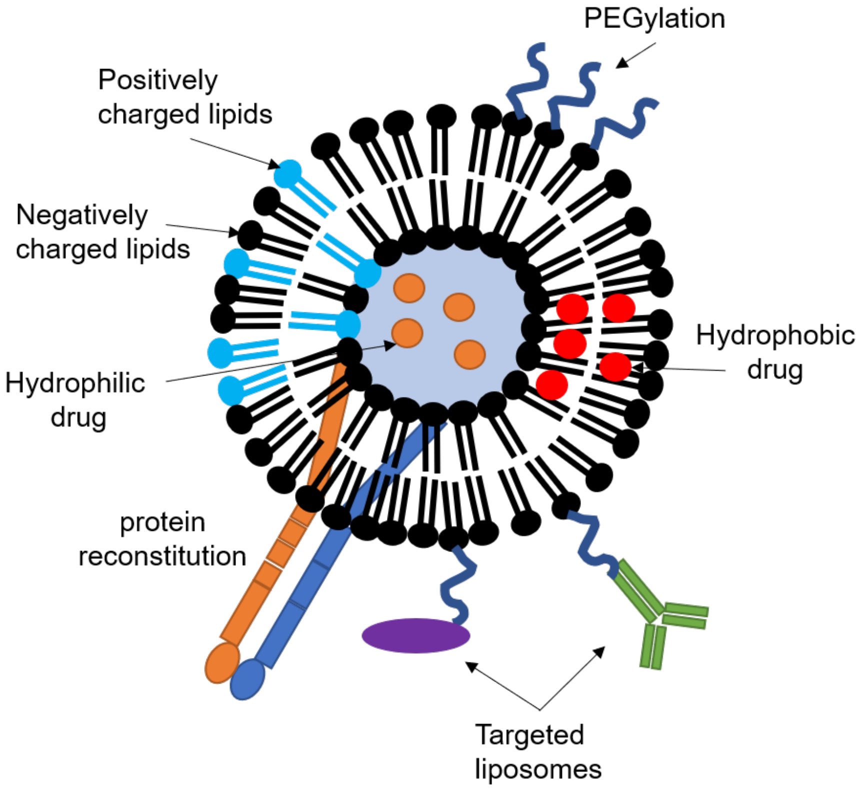

Figure 7: Liposomes and their modifications. Liposomes can carry hydrophobic and hydrophilic drugs. They can be modulated by polymer coating (e.g. PEG) and proteins can be reconstituted or attached to the surface covalently. Lipid composition can be easily controlled. Depiction is adapted from (Beltrán-Gracia et al. 2019)

For instance, circulation time can be prolonged by polyethylenglycol binding (PEGylation) (Suk et al. 2016); immune response and phagocytosis are modulated by lipid charge; and fluidity as well as permeability are affected by lipid transition temperature (Kraft et al. 2014). Proteins can be attached to the liposomes surface and transmembrane proteins can be reconstituted into the liposome membrane. Moreover, increased cholesterol content stabilizes the liposomes and reduces unspecific protein interactions (Beltrán-Gracia et al. 2019).

1.7. Nanoparticles and their applications

In addition to liposomes, that are nanoparticles (NPs) due to their size ranging from 1 nm to 1 µm, other NPs find their way in the field of biomedical applications. They are classified in carbon-based, metal, ceramic, polymeric and lipid-based NPs (Khan et al. 2019).

Nanoparticles can be synthesized with favored chemical compositions, shape, roughness, surface charge, size and coating, dependent on their specific application. Either targeted drug delivery or imaging utilization involve blood contact. The resulting interplay of blood components with the highly active NP surface leads to a formation of a protein corona, which decreases the surface energy (Vilanova et al. 2016; Auría-Soro et al. 2019). However, alterations in protein structure upon NP-protein interaction may induce an immune response and activate the complement system. Furthermore, these bioconjugates could result in penetration of cell membranes, which in turn changes cell properties, receptors and signaling pathways (Di Silvio et al. 2017). The effect is desired in targeted drug delivery, but should be prevented for unspecific reactions. Due to this, NPs are coated with biocompatible materials, such as dextran or PEG. Especially PEGylation prolongs circulation time and stabilization of NPs in the blood stream. In this PhD thesis, properties of maghemite NPs (Fe_2O_3) and their interaction with biomimetic platelet membranes are studied. Nanoparticles are applied in several medical fields, e.g. magnetic resonance imaging, targeted drug delivery due to magnetism and hyperthermia as a therapeutic procedure (Múzquiz-Ramos et al. 2015).

1.8. Biophysical tools to study proteins and their interactions with lipids, drugs and nanoparticles

Biophysics displays an interface of various interdisciplinary fields coming from biology, physics, mathematics and chemistry to understand biological functions. Already Leonardo da Vinci utilized the mechanism behind the bird flight to construct flying devices in the 16th century. Moreover, Giovanni Alfonso Borelli used mathematics to prove biological theories and Luigi Galvani laid the foundations for electrical potentials in the human body, and therefore, the mechanism of muscle contraction and nerve stimulation. In the field of biophysics, groundbreaking characters such as Schrödinger, van't Hoff, Delbrück, and Einstein characterize fundamental understanding of thermodynamics and kinetics, optics, osmotic pressure, molecular Brownian motion, radiation and nuclear magnetic resonance (NMR).

Resulting instrument development for biological questions is nowadays called applied biophysics and contributes to the knowledge of e.g. protein and deoxyribonucleic acid structure determination, electrical impulses in cells, biological membranes and biomechanics.

Currently, biophysical tools can be used to study proteins, membranes and properties of cells. For instance, structure of proteins can be characterized by circular dichroism (CD) spectroscopy. Although CD spectroscopy results are limited compared to other techniques such as X-ray, NMR or cryo-EM, CD spectroscopy has many advantages such as label-free and material saving analysis. It uses ultraviolet wavelengths in the range of 240-190 nm to display peptide bonds, protein folding and unfolding, which leads to specific spectra for detailed secondary structures of proteins (Miles and Wallace 2016). Another promising technique to study proteins in solution is dynamic light scattering (DLS). With DLS diffusion coefficient and hydrodynamic radii can be calculated. Fundamental theories are Rayleigh scattering and the Mie theory describing the scattering effects of particles in solution. Thereby, the Stokes-Einstein equation describes that the friction exerted by a particle is proportional to its radius and to the viscosity of the solvent surrounding the particles (Stetefeld et al. 2016). Biofunctionalized surfaces have been elucidated by the appearance of multiple surface-sensitive techniques e.g. atomic force microscopy (AFM), surface plasmon resonance (SPR), ellipsometry and quartz-crystal microbalance (QCM). The latter is suitable for the study of processes within thin films on different surfaces. It is a real-time measurement detecting changes in the frequency of an oscillating piezoelectric quartz sensor, which can be converted to mass adsorption. Additionally, viscoelastic properties of adsorbed material can be measured with dissipation monitoring. This technique offers the opportunity to analyze biosensors, multilayers of polymers and proteins, cell surfaces and its interaction as well as membranes and cell toxicity (Tonda-Turo et al. 2018; Dixon 2008).

AFM monitors among imaging techniques combined with FRET and others, mechanical properties of cell and their elasticity, as well as single molecule force microscopy and microfluidics (Krieg et al. 2019). Other techniques were developed recently such as real-time deformability cytometry (RT-DC) which promotes biomechanical studies in solution (Otto et al. 2015).

In this PhD thesis, a combination of biophysical, molecular biology techniques and molecular dynamic simulations were used to elucidate the impact of integrin dynamics in a biomimetic liposome- and cellular-system.

1.9. Aim of this thesis

Membrane receptors of the integrin family have been intensively studied over the last decades, indicating their important role in health and disease. Integrin αIIbβ3 is crucial for platelet aggregation, whose loss or impaired function leads to the disease Glanzmann thrombasthenia. Additionally, the potential risk of interaction with drugs, but also abnormal conformational changes within the integrin lead to generation of autoantibodies characteristic for the autoimmune disorder immune thrombocytopenia (ITP). To gain insights into the mechanisms behind these diseases, it is essential to study the transmembrane protein αIIbβ3 primarily under physiological conditions. The complexity and heterogeneity of individual platelets make the study of distinct proteins intricate demonstrating the necessity of a controlled system. Hence, in this thesis experiments were designed to establish a platelet-mimicking membrane system and reconstitution of the purified platelet receptor integrin αIIbβ3. After proving its applicability, the system should be utilized for studying the conformational landscape of αIIbβ3 under artificial, physiological and clinically relevant conditions.

Furthermore, these experiments are aligned with studies of HEK293 cells co-expressing both integrin subunits and conformation-related mutations. Cell studies facilitates the evaluation of downstream effects of integrin activation and its impact on the cytoskeleton or cell mechanical properties in general.

Aforementioned experiments are intended to advance the understanding of integrin activation and its mechanism of action in diseases such as Glanzmann thrombasthenia or Immune thrombocytopenia.

2. Materials

2.1. General equipment

Name	Manufacturer
AcCellerator	Zell Mechanik, Dresden, Germany
ÄKTA Explorer	GE Healthcare, Chicago, USA – now Cytiva, Washington, USA
ÄKTA Micro	GE Healthcare, Chicago, USA
ÄKTA Pure	GE Healthcare, Chicago, USA – now Cytiva, Washington, USA
Amnis Imaging Flow Cytometer	Luminex Corporation, Austin, USA
AFM Nanowizard 3	JPK BioAFM – Bruker Nano GmbH, Berlin, Germany
Bacterial shaker innova 40	New Brunswick Scientific, Nurtingen, Germany
BD FACS Aria III sorter	Becton Dickinson, Franklin Lakes, USA
BD LSR II flow cytometer	Becton Dickinson, Franklin Lakes, USA
CCD camera Sharpeye	Tröndle, Moorenweis, Germany
Centrifuge Allegra X-15R	Beckman Coulter, Krefeld, Germany
Centrifuge Heraeus Fresco 21	Thermo Fisher, Darmstadt, Germany
Chirascan CD spectrometer	Applied Photophysics, Leatherhead, UK
Cytation 5 Plate Reader	Biotek Instruments, Winooski, USA
DS-11 Spectrophotometer/Fluorometer	DeNovix Inc., Wilmington, USA
Easycast Mini Gel Electrophoresis tank	Thermo Fisher, Darmstadt, Germany
Elmasonic S 30 H	Elma Schmidbauer GmbH, Singen, Germany
Gel Dock XR imaging system	Bio-Rad, Munich, Germany
iBright FL1500	Invitrogen, Carlsbad, USA
Incubator	BINDER, Tuttlingen, Germany
Ismatec IPC-NP4 peristaltic pump	Idex Health & Science, Wertheim-Mondfeld, Germany
JS-4.750 Swinging bucket rotor	Beckman Coulter, Krefeld, Germany
Leica TCS Sp5 confocal microscope	Leica Camera AG, Wetzlar, Germany
Microscope Eclipse 50i	Nikon, Minato, Japan
Microscope Eclipse TS100	Nikon, Minato, Japan
Microscope ix 81	Olympus, Shinjuku, Japan
Microscope Axio Observer Z1	Zeiss, Oberkochen, Germany

Mini Gel Tank	Invitrogen, Carlsbad, USA
MiniMACS Separator	Miltenyi Biotec GmbH, Bergisch Gladbach, Germany
Mini Protean tetra vertical electrophoresis cell	Bio-Rad, Munich, Germany
MLS-50 Rotor	Beckman Coulter, Krefeld, Germany
OptimaTM MAX-XP Ultracentrifuge	Beckman Coulter, Krefeld, Germany
Paradigm Plate Reader	Beckman Coulter, Krefeld, Germany
PCR thermocycler C1000 touch thermal cycler	Bio-Rad, Munich, Germany
pH meter Seven Easy	Mettler Toledo, Gießen, Germany
Photometer NanoDrop 2000c	Thermo Fisher, Darmstadt, Germany
Q-Sense Analyzer	Biolin Scientific Holding AB, Västra Frölunda, Sweden
SiO_2-coated quartz crystal sensor	Biolin Scientific Holding AB, Västra Frölunda, Sweden
Scale Excellence XS64	Mettler Toledo, Gießen, Germany
Scale KERN EW 1500-2M	Kern & Sohn, Balingen, Germany
Sorvall RC5C Plus Refrigerated Centrifuge	Thermo Fisher, Darmstadt, Germany
Sorvall Rotor SS34	Thermo Fisher, Darmstadt, Germany
Sterile Bench Mars Safety Class 2	LaboGene, Lillerod, Denmark
TECAN infinite M200Pro plate reader	Tecan group, Männedorf, Switzerland
Thermomixer Comfort	Eppendorf, Hamburg, Germany
TransBlot SD Transfer Cell	BioRad, Hercules, USA
Transmission electron microscope LEO 906	Carl Zeiss Microscopy GmbH, Oberkochen, Germany
UV Ozone Pro Cleaner Plus	Bioforce Nanoscience, Ames, USA
VWR Power Source	VWR, Mönchweiler, Germany
Western Blot Imager Chemiluminescence detector ChemiSmart 5100	PEQLAB Biotechnologie GmbH, Erlangen, Germany
XCell SureLockTM Electrophoresis Cell	Invitrogen, Carlsbad, USA
Zetasizer Nano ZS	Malvern Instruments, Herrenberg, Germany
Zetasizer Ultra	Malvern Instruments, Herrenberg, Germany

2.2. Chemicals, kits and consumables

Name	Manufacturer
Acetic acid	Carl Roth GmbH, Karlsruhe, Germany
Agarose	Biozym Scientific GmbH, Hessisch Oldendorf, Germany
Protein A and Leupeptide (A/L)	Thermo Fisher, Darmstadt, Germany
Ammonium molybdate tetrahydrate	Carl Roth GmbH, Karlsruhe, Germany
aqueous phosphotungistic acid	VWR, Radnor, USA
Ammonium persulfate (APS)	Sigma Aldrich, Taufkirchen, Germany
Ascorbic acid	Merck KgaA, Darmstadt, Germany
Bicinchoninic acid (BCA) assay kit	Sigma Aldrich, Taufkirchen, Germany
Bisacrylamide	Carl Roth GmbH, Karlsruhe, Germany
Bromphenol blue	Fisher Scientific, Leics, UK
Buffer 2 (50 mM NaCl, 10 mM Tris-HCl, 10 mM $MgCl_2$, 1 mM DTT) and buffer 4 (50 mM potassium Acetate, 20 nM Tris-acetate, 10 mM Magnesium Acetate, 1mM DTT) for 1 x digestion buffer	NEB, Ipswich, USA
$CaCl_2$	Carl Roth GmbH, Karlsruhe, Germany
Cantilever, tipless, CSC38	MikroMasch, Sofia, Bulgaria
Cell Carrier	Zell Mechanik, Dresden, Germany
3-[(3-Cholamidopropyl)dimethylammonio]-1-propanesulfonate (CHAPS)	Carl Roth GmbH, Karlsruhe, Germany
Chloroform	Carl Roth GmbH, Karlsruhe, Germany
Coomassie Blue G- and R-250	Thermo Fisher, Darmstadt, Germany
Cuvettes, various	Zetasizer Nano Series, Malvern, Worcestershire, UK
Dextran-6 (6 kDa)	Carl Roth GmbH, Karlsruhe, Germany
Dithiothreitol	Carl Roth GmbH, Karlsruhe, Germany
Ethylenediaminetetraacetic acid (EDTA)	Sigma Aldrich, Taufkirchen, Germany
Ethanol, 99,8 %	Carl Roth GmbH, Karlsruhe, Germany
FACS tubes, Falcon	Fisher Scientific, Leics, UK
Formalin	Sigma Aldrich, Taufkirchen, Germany
GeneJET plasmid Miniprep Kit	Thermo Fisher, Darmstadt, Germany
Glue Optical Adhesive 68	Norland, Cranbury, USA
Glutaraldehyde	Agar Scientific, Stansted, UK

Gycerol	Sigma Aldrich, Taufkirchen, Germany
HCl	Carl Roth GmbH, Karlsruhe, Germany
Hellmanex III	Hellma, Müllheim, DEU
4-(2-Hydroxyethyl)piperazine-1-ethanesulfonic acid (HEPES)	Carl Roth GmbH, Karlsruhe, Germany
8 well µ-Slides	Ibidi, Gräfelfing, Germany
Instant Skim Milk Powder	Safeway, Pleasanton, USA
Isopropanol	Carl Roth GmbH, Karlsruhe, Germany
KCl	Fisher Scientific, Loughborough, UK
KH_2PO_4	Fisher Scientific, Loughborough, UK
Leupeptin	Thermo Fisher, Darmstadt, Germany
Methanol	Carl Roth GmbH, Karlsruhe, Germany
Methyl α-D mannopyranoside	Carl Roth GmbH, Karlsruhe, Germany
$MgCl_2$	AppliChem GmbH, Darmstadt, Germany
Microfluidic Chips FlicXX, 30 µm	Zell Mechanik, Dresden, Germany
$MnCl_2$ tetrahydrate	Carl Roth GmbH, Karlsruhe, Germany
MS Column	Miltenyi Biotec GmbH, Bergisch Gladbach, Germany
NaCl	Carl Roth GmbH, Karlsruhe, Germany
NaOH	Fisher Scientific, Hampton, USA
$Na_4P_2O_7$	Fisher Scientific, Hampton, USA
NP-40	Sigma Aldrich, Taufkirchen, Germany
Nitrocellulose membrane	GE Healthcare, Chicago, USA
Novex Sharp Unstained Protein Standard	Thermo Fisher, Darmstadt, Germany
NuPAGE 4-12% Bis-Tris Protein Gels	Thermo Fisher, Darmstadt, Germany
NuPAGE MES SDS Running Buffer (20X)	Thermo Fisher, Darmstadt, Germany
NuPAGE Transfer Buffer	Thermo Fisher, Darmstadt, Germany
PMSF	AppliChem GmbH, Darmstadt, Germany
PureLink HiPure Plasmid Maxiprep Kit	Invitrogen, Carlsbad, Germany
DNA Stain G	Serva, Heidelberg, Germany
Sodiumdodecyl sulfate (SDS)	Merck KgaA, Darmstadt, Germany
Silica Beds 5 µm	Bangs Laboratories, Fishers, USA
TLC plates, silica gel 60G, glass backed	Merck KgaA, Darmstadt, Germany
Tris-Base	Sigma Aldrich, Taufkirchen, Germany
Triton X-100	Carl Roth GmbH, Karlsruhe, Germany

Tween 20	AppliChem GmbH, Darmstadt, Germany
Tetramethylethylendiamin (TEMED)	Carl Roth GmbH, Karlsruhe, Germany
TMB (3,3', 5,5' Tetramethylbenzidine) substrate	Becton Dickinson, Franklin Lakes, USA
Tris-Glycine SDS Running Buffer	Invitrogen, Carlsbad, USA
QuikChange II Site-Directed Mutagenesis Kit	Agilent Technologies, Santa Clara, USA
West Pico Chemiluminescent substrate	Thermo Fisher, Darmstadt, Germany
5 mm path length cuvette	110-QS; Hellma Analytics, Müllheim, Germany

2.3. Proteins, enzymes, nanoparticles and antibodies

Name	**Manufacturer**
α-helical (AH) peptide (sequence taken from (Cho et al. 2007b))	GenScript Biotech, New Jersey, USA
Alexa Fluor® 647 anti-human CD41/CD61 antibody	BioLegend, SanDiego, USA
Anti-human β-actin antibody for WB	Cell Signaling, Danvers, USA
Anti-human αβ-tubulin antibody for WB	Cell Signaling, Danvers, USA
Anti-human CD41	Bio-Techne Holding, Minneapolis, USA
Anti-human CD61 antibody-HRP	BioLegend, SanDiego, USA
Anti-human GAPDH antibody	HyTest, Turku, Finland
Anti-rabbit IgG antibody-HRP	Jackson ImmunoResearch Laboratories, West Grove, USA
Anti-mouse IgG antibody-HRP	Jackson ImmunoResearch Laboratories, West Grove, USA
Anti-mouse IgG-Alexa Fluor 647	Thermo Fisher, Darmstadt, Germany
Alexa Fluor® 488 anti-human CD41 antibody	BioLegend, SanDiego, USA
Alexa Fluor® 647 anti-human CD61 antibody	BioLegend, SanDiego, USA
Bovine Serum Albumin	Sigma Aldrich, Taufkirchen, Germany
Fibrinogen	Merck KgaA, Darmstadt, Germany
Fibronectin	Merck KgaA, Darmstadt, Germany
FITC anti-mouse IgM antibody	BioLegend, SanDiego, USA
FITC anti-human CD41/CD61 antibody PAC-1	BioLegend, SanDiego, USA
GeneRuler 1 kb DNA ladder	Thermo Fisher, Darmstadt, Germany

GPIIbIIIa Integrin, αIIbβ3	Enzyme Research Laboratories, South Bend, USA
Microstandard	Sigma Aldrich, Taufkirchen, Germany
γ-Fe_2O_3 Nanoparticles	Alli Abou-Hassan, Sorbonne Université, Paris, France
Purified anti-human CD41/CD61 antibody PAC-1	BioLegend, SanDiego, USA
Phalloidin CF 647	Biotium, Fremont, USA
PNGase F	NEB, Ipswich, USA
Restriction enzymes: Bgl II, Hind III, Xho I, EcoR I	NEB, Ipswich, USA
SeeBlue Plus2 Prestained Standard	Thermo Fisher, Darmstadt, Germany

2.4. Purification procedures

Name	**Manufacturer**
Affinity column HiTrap Con A 4B Columns 5mL	GE Healthcare, Freiburg, Germany
Size exclusion column HiPrep 16/60 Sephacryl S-300 HR column, 16 mm × 600 mm	GE Healthcare, Freiburg, Germany
Affinity column HiTrap Heparin HP 5mL	GE Healthcare, Freiburg, Germany
Amicon Ultra-15 Centrifugal Filter Unit	Merck KgaA, Darmstadt, Germany

2.5. Liposome preparation

Name	**Manufacturer**
Bio-Beads SM-2 Resin	Bio-Rad, Munich, Germany
Cholesterol (ovine)	Avanti Polar Lipids Inc., Alabaster, USA
1,2-dimyristoyl-sn-glycero-3-phosphocholine (DMPC)	Avanti Polar Lipids Inc., Alabaster, USA
1,2-Dimyristoyl-sn-glycero-3-phospho-rac-(1-glycerol) sodium salt (DMPG)	Avanti Polar Lipids Inc., Alabaster, USA
1,2-dioleoyl-sn-glycero-3-phosphocholine (DOPC)	Avanti Polar Lipids Inc., Alabaster, USA
Extruder Set	Avanti Polar Lipids Inc., Alabaster, USA

Mini Dialysis Kit 1 kDa cut-off	GE Healthcare, Freiburg, Germany
Mini Dialysis Kit 8 kDa cut-off	GE Healthcare, Freiburg, Germany
Optiprep	STEMCELL Technologies Inc., Vancouver, Canada
Polycarbonate Membrane (pore size 100 nm)	Avanti Polar Lipids Inc., Alabaster, USA
Pyrextubes	Sigma Aldrich, Taufkirchen, Germany
Spectra/Por 6 Dialysis Membranes, 10 kDa, 50 kDa	Spectrumchemical, New Brunswick, USA
N-stearoyl-D-erythro-sphingosylphosphorylcholine (d18:1/18:0) (SM)	Avanti Polar Lipids Inc., Alabaster, USA
Sucrose	Merck KgaA, Darmstadt, Germany

2.6. Cell and bacterial culture

Name	**Manufacturer**
Ampicillin	Sigma Aldrich, Taufkirchen, Germany
Dimethyl sulfoxide (DMSO)	Roth, Karlsruhe, Germany
Dulbecco´s Modified Eagles medium (DMEM) high glucose	Biowest, Nuaille, France
Dulbecco´s Phosphate Buffer Saline w/o Ca^{2+}, Mg^{2+}	Biowest, Nuaille, France
Dulbecco´s Phosphate Buffer Saline with Ca^{2+}, Mg^{2+}, 10 x	Biowest, Nuaille, France
Fetal bovine serum (FBS), Qualified, H	Biowest, Nuaille, France
Geneticin 418 (G-418) solution	Biowest, Nuaille, France
Human Embryonic Kidney (HEK) 293 cell line	FLI, Riems, Germany
HEK293 αIIbβ3 wildtype	Biophysical chemistry, Greifswald, Germany
HEK293 αIIbβ3 active (C560R)	Biophysical chemistry, Greifswald, Germany
HEK293 αIIbβ3 inactive (β3-R563C/αIIb-R320C)	Biophysical chemistry, Greifswald, Germany
L-Glutamine 100x	Biowest, Nuaille, France
NEB® 5-alpha Competent *E. coli*	NEB, Ipswich, USA

LB Agar	Carl Roth GmbH, Karlsruhe, Germany
LB Medium	Carl Roth GmbH, Karlsruhe, Germany
pcDNA3.1. *ITGA2B* WT	Biophysical Chemistry, Greifswald, Germany (modified from Prof. Karen Vanhoorelbeke, Kortrijk, Belgium)
pcDNA3.1. *ITGA2B* R320C	Biophysical Chemistry, Greifswald, Germany
pcDNA3.1. *ITGB3* WT	Biophysical Chemistry, Greifswald, Germany (modified from Prof. Karen Vanhoorelbeke, Kortrijk, Belgium)
pcDNA3.1. *ITGB3* C560R	Biophysical Chemistry, Greifswald, Germany
pcDNA3.1. *ITGB3* R563C	Biophysical Chemistry, Greifswald, Germany
Penicillin/Streptavidin 100x	Biowest, Nuaille, France
Transit-LT1 Transfection agent	Mirus Bio, Madison, USA
Trypan Blue	VWR International, Radnor, USA
Trypsin/EDTA 1x	Biowest, Nuaille, France

2.7. Software

Name	Manufacturer
Adobe Photoshop CS6	Adobe System Software, Dublin, Ireland
CD Pro-Data SX Chirascan	Applied Photophysics, Leatherhead, UK
CD Pro-Data Viewer	Applied Photophysics, Leatherhead, UK
Chemsketch	ACD/Labs, Toronto, Canada
Expasy.org/protparam	(Gasteiger et al. 2003)
FlowJo	FlowJo LLC, Ashland, USA
GIMP 2.10.14	GIMP Development Team
i-control	TECAN, Männedorf, Switzerland
Image-Lab	Bio-Rad Laboratories, Hercules, USA
ImageSP software	SYSPROG, Minsk, Belarus
JPK Software	JPK BioAFM – Bruker Nano GmbH, Berlin, Germany
JPK Data Processing	JPK BioAFM – Bruker Nano GmbH, Berlin, Germany
Microsoft Office 2016	Microsoft, Redmond, USA
Origin 2020	OriginLab, Northhampton, USA
PyMol 2.3	DeLano Scientific, San Fransisco, USA

Shape-In	Zell Mechanik, Dresden, Germany
Shape-Out	Zell Mechanik, Dresden, Germany
Snapgene 5.0.7.	GSL Biotech LLC, San Diego, USA
Q-Soft401 V2.5	Biolin Scientific Holding AB, Västra Frölunda, Sweden
Q-Tools V.3.0	Biolin Scientific Holding AB, Västra Frölunda, Sweden
R	R Core Team (2017). R: A language and environment for statistical computing. R Foundation for Statistical Computing, Vienna, Austria. - https://www.R-project.org/
RStudio	RStudio Team (2020). RStudio: Integrated Development for R. RStudio, PBC, Boston, USA- http://www.rstudio.com/
Unicorn 7.0	GE Healthcare, Freiburg, Germany
VMD 1.9	University of Illinois, Urbana-Champaign, USA
Zetasizer Nano Software	Malvern Instruments, Herrenberg, Germany
Zetasizer Ultra Software	Malvern Instruments, Herrenberg, Germany

3. Experimental procedures

3.1. Enzyme-linked immunosorbent assay (ELISA)

Enzyme-linked immunosorbent assay detects antigens, proteins or antibodies bound to a solid phase, i.e. a microtiter plate. Enzyme-conjugated antibodies bind specifically to the antigen and enzyme-substrate reaction leads to a color change, which identifies the presence of the antigen.

Microtiter plates were coated with 100 ng/µL integrin αIIbβ3 in coating buffer consisting of 15 mM sodium bicarbonate, pH 9.5, incubated 12 h at 4 °C and washed with washing buffer containing PBS with 0.05% Tween 20. After blocking for 2 h with 3 % bovine serum albumin in PBS at 37°C, the plates were washed five times with washing buffer and were incubated for 1 h at room temperature (RT) with different antibody dilutions (mouse anti-human CD61 or rabbit anti-human CD41). Plates were washed again five times with washing buffer and 70 ng/mL of the specific horseradish peroxidase (HRP)-coupled antibody (anti-rabbit IgG-HRP and anti-mouse IgG-HRP) was added and incubated at RT for 45 min. After five times washing, the plate was incubated with TMB (3,3', 5,5' Tetramethylbenzidine) substrate reagent for 5 min at RT. The reaction was stopped by adding 100 µL 0.5 M H_2SO_4 and the optical density (OD) was measured at 450 nm with a Tecan infinite 200 absorbance reader. For evaluation, the values of a blank control, without integrin, were subtracted from the samples.

3.2. Integrin purification

The purification of integrin αIIbβ3 followed a protocol adapted from Ye et al. (Ye et al. 2010). For liposome preparation with Triton X-100, the used integrin αIIbβ3 was purchased from Enzyme Research laboratories. However, integrin reconstitution following the protocol with CHAPS was carried out with purified integrin from outdated human plasma.

Generally, the used buffers listed in Table 1 were filtered through a 0.22 µm membrane filter and degassed by sonication for 30 min. Purification was performed with an ÄKTA Explorer or an ÄKTA Pure System.

Briefly, 500 mL of platelet rich plasma were obtained from AG Cardiovascular Cell Research at the University Medicine Greifswald and pelletized at 1,800 x g for 30 min at RT. The pellet was dissolved in 50 mL wash buffer and centrifuged again to remove plasma proteins. The pellet was dissolved in 50 mL lysis buffer and stirred carefully overnight at 4°C.

The mixture was centrifuged at 12,000 x g for 1 h at 4 °C. The filtered clear supernatant was loaded onto a concanavalin A (ConA) column to separate the glycoproteins from the other platelet proteins. The ConA column was equilibrated at a flow rate of 1 mL/min with integrin buffer for five column volumes. After lysate injection, the column was washed extensively with CHAPS buffer for at least ten column volumes to remove most of the Triton X-100. The elution was initialized by ConA elution buffer. The eluate was collected in 5 mL tubes and the elution peak fractions were analyzed *via* SDS-PAGE and integrin-containing fractions were pooled for further steps.

To remove fibrinogen and thrombospondin 1, the ConA eluate was passed through a heparin column using a flow rate of 1 mL/min after equilibration with CHAPS buffer. The flow through was then concentrated to a volume of 2 mL with an Amicon Ultra-15 Centrifugal Filter Unit and further purified by SEC using a HiPrep 16/60 Sephacryl S-300 column. The sample was loaded onto the SEC column and eluted at 0.5 mL/min. Integrin-containing fractions were identified by SDS-PAGE and respective protein content was determined by spectrophotometric measurements.

Table 1: Buffer compositions for integrin purification. The pH was adjusted to 7.4 using NaOH or HCl.

Buffer Name	Composition
Integrin buffer	20 mM Tris, 150 mM NaCl, 1 mM $CaCl_2$, 1 mM $MgCl_2$, 0.1 % Triton X-100
CHAPS buffer	20 mM HEPES, 150 mM NaCl, 1 mM $CaCl_2$, 1 mM $MgCl_2$, 1 % CHAPS
Wash buffer	20 mM Tris, 150 mM NaCl
Lysis buffer	20 mM Tris, 150 mM NaCl, 0.5 mM $CaCl_2$, 1 % Triton X-100, 5 mM PMSF, 10 µmol Leupeptin
ConA elution buffer	20 mM Tris, 150 mM NaCl, 1 mM $CaCl_2$, 1 mM MgCl2, 1 % CHAPS, 5 µmol Leupeptin, 200 mM methyl α-D mannopyranoside
Heparin column elution buffer	20 mM Tris, 1M NaCl

3.3. Integrin reconstitution into liposomes

3.3.1. Reconstitution protocol with Triton X-100

The preparation of liposomes followed an adapted protocol from Erb and Engel (Erb and Engel 2000). The liposome buffer consisting of 20 mM Tris, 50 mM NaCl, and 1 mM $CaCl_2$ was adjusted to pH 7.4 with HCl. A final amount of 800 nmol DMPG:DMPC (ratio 1:20) or DOPC:SM:cholesterol (ratio 37.5:37.5:25) was dried under a stream of nitrogen and incubated under vacuum overnight. Dried lipids were dissolved in liposome buffer containing 0.1 % Triton X-100 and 0.2 mg of αIIbβ3 in liposome buffer and incubated for 2 h at 37 °C. Afterwards, Triton X-100 was removed by adding twice 70 mg SM-2 biobeads for 3 h at 37 °C. To separate free (non-reconstituted) protein from the synthesized liposomes, the sample was added on a four-step sucrose gradient (2 M, 1.2 M, 0.8 M, 0.4 M) and ultracentrifuged at 4 °C and 268,000 x g for 24 h. The liposome fraction was then dialyzed for three days against liposome buffer, stored at 4 °C and used within four days.

3.3.2. Reconstitution protocol with CHAPS

Liposomes were prepared following a protocol adapted from Coskun et al. (Coskun et al. 2011). Briefly, HEPES liposome buffer contained of 25 mM HEPES, 150 mM NaCl, 1 mM $CaCl_2$ with pH adjusted to 7.4 by HCl. 1.6 µmol lipid mixture consisting of DOPC:SM:cholesterol (different ratios are indicated in the respective graphs), was dried under a stream of nitrogen and vacuum overnight. Then, dried lipids were dissolved in HEPES liposome buffer and incubated under shaking for 20 min at 54 °C. Unilamellar vesicles were formed by freeze-thaw cycles (10 cycles) and subsequent extrusion at 54 °C through a 100 nm pore size membrane. Afterwards, the liposomes were solubilized with CHAPS (approximately 0.9%), which was monitored by DLS as well as turbidity measurements, and incubated with 0.25 mg αIIbβ3 for 20 min at 30 °C. The sample was then dialyzed (four times against 2 L of HEPES liposome buffer) for two days at 4 °C. Non-reconstituted protein was removed from liposome fraction by a three step Optiprep gradient (30%, 10%, 5%) at 208,000 x g for 2 h. The liposome fraction was collected and dialyzed for two days against HEPES liposome buffer.

3.4. Characterization of liposomes

3.4.1. Phosphate assay

Phosphate Assay was crucial for determination of phospholipid content after integrin reconstitution into liposomes. A calibration standard curve was prepared with respective buffer and 50 µL of the dilutions as well as the sample were transferred into glass tubes. After addition of 500 µL 70 % perchloric acid the mixture was covered with glass marbles and incubated for 3 h at 200 °C. Subsequently, 1 mL of 10 % ammonium molybdate tetrahydrate solution and 1 mL 10 % ascorbic acid were added, mixed and incubated for 1 h at 37°C. From each tube 200 µL were added to a microtiter plate and absorbance was measured at 820 nm to detect the emerged phosphomolybdic acid (Morrison 1964).

3.4.2. Thin-layer chromatography (TLC)

TLC measurements were carried out to determine the presence of intact lipids in the liposome and proteoliposome samples. Silica gel function as the stationary phase on a glass plate whereas the solvent, which is the mobile phase, migrates because of capillary forces to the top of the plate. The solvent meets the sample and carries it to the top of the plate as well. For silica gel non-polar substances migrate faster to the top as polar substances, which causes separation of different mixtures (Fuchs et al. 2011).

Lipids were extracted using a two-step extraction protocol established by Bligh and Dyer (Bligh and Dyer 1959). First step was the addition of three volumes of chloroform:methanol 10:1 mixture, which was followed by 20 min incubation on ice and centrifugation at 1,000 x g at 4 °C. The organic phase was then collected and the first step was repeated with a chloroform: methanol (2:1) mixture. The lipid containing organic phase was then dried under a stream of nitrogen and the lipids were resuspended in 30 µL chloroform:methanol (2:1) mixture and applied on a TLC plate silica gel 60G. TLC chamber as well as the TLC plate was washed and equilibrated with methanol:chloroform (2:1) mixture. For TLC analysis chloroform:methanol:water (65:25:4) was used as running solution. Lipids were stained by 20 min incubation in Coomassie Blue R-250 dissolved in 20% methanol and washed for 5 min with 20 % methanol. Images were taken using a iBright FL1500 Imaging System.

3.4.3. Transmission electron microscopy (TEM) – Negative staining

TEM is a powerful microscopy technique that overcomes the resolution limitations of light microscopy. Electrons are emitted by an electron gun and accelerated. After passing through electromagnetic lenses, the electron beam is focused onto the sample and shines through the very thin specimen. The transmitted beam is recombined and magnified to form a picture on the image plane. The impact of electrons excites the screen and a magnified image of the sample is visible (Williams and Carter 1996). For the visualization of small biological structures such as proteins or lipids, negative staining with phosphotungstic acid was used, which stains the background to create higher contrast.

TEM samples preparation and imaging were carried out in the Imaging lab of Dr. Rabea Schlüter at the University of Greifswald (Germany). Proteoliposomes were allowed to adsorb onto a glow discharged carbon-coated holey Pioloform film on a 400-mesh grid for 5 min. For the negative stain, the grid was transferred onto two droplets of deionized water and subsequently on a droplet of 2 % aqueous phosphotungistic acid (pH 7.4) for 30 s and finally on a second droplet for 4 min. Next, samples were blotted with filter paper, air-dried and analyzed using a transmission electron microscope LEO 906 at an acceleration voltage of 80 kV. Pictures were taken with flat films with a magnification of 60,000-times or with a wide-angle dual speed CCD camera Sharpeye, which was operated by the ImageSP software. Afterwards, the micrographs were analyzed using Adobe Photoshop CS6.

3.4.4. Sodium dodecylsulfate-polyacrylamide gel electrophoresis (SDS-PAGE)

In SDS-PAGE, proteins are separated in a polyacrylamide gel by their size. Under denaturating conditions, internal charges are covered by an overall negative charge caused by SDS in the added loading dye containing also dithiothreitol (DTT) as reducing agent (Table 2).

SDS-PAGE was carried out to detect the integrin subunits under reductive conditions upon protein purification, as well as reconstitution into liposomes. Samples were incubated 5 min at 95 °C and loaded to Tris-Glycine gels (12%). The gels were run in Tris-Gylcine Buffer for 35 – 55 min at 150-200 V, visualized with Coomassie blue G-250 and imaged in an iBright FL1500.

Table 2: Composition of loading dye for SDS-PAGE.

Ingredient	Amount for 10 mL
Tris/HCl 0.5 M pH 6.8	7 mL
Gylcerol	3 mL
SDS	1 g
DTT	0.93 g
Bromphenol Blue	1.2 mg

3.4.5. Determination of protein concentration

Determination of protein concentration of purified protein was measured using a spectrophotometer. The protein content was calculated using the absorbance at 280 nm (Simonian 2002), with a theoretical extinction coefficient and molecular weight obtained from the expasy.org/protparam webtool (Gasteiger et al. 2003).

Determination of protein concentration in proteoliposomes was done by a modified bicinchonic acid (BCA) assay adapted from Parmar et al. (Parmar et al. 1999). Protein microstandards or 25 µL proteoliposome samples were pipetted into a microtiter plate. After addition of 25 µL of 0.5 % SDS, 50 µL of working BCA reagent was added to each well. The plate was incubated for 2 h at 37 °C and the absorbance was measured at 562 nm. The protein concentration in the samples was determined from a standard curve with the mentioned protein standard. Due to peptide bonds in the protein, Cu^{2+} ions are reduced to Cu^{+} ions, during the reaction of the BCA assay. The Cu^{+} ions are forming a violet complex with the BCA, whose absorbance can be measured at 562 nm (Smith et al. 1985).

3.4.6. Dynamic light scattering (DLS)

Generally, in DLS, known also as photon correlation spectroscopy, a monochromatic beam of light encounters a solution containing macromolecules, resulting in the detection of the scattered light as function of the size of macromolecules. Due to Rayleigh scattering, larger molecules will scatter the light more strongly than a small molecule at a given wavelength.

DLS enables the measurement of the size of macromolecules due to its Brownian motion, which is dependent on the solvent's viscosity and, by temperature as well. The scattering intensity fluctuates over time due to the Brownian motion of particles in solution, which can be characterized by a specific autocorrelation function at a specific detection angle. By fitting the correlation curve to an exponential function, the diffusion coefficient (D_f) can be calculated (Stetefeld et al. 2016).

Assuming that the macromolecules form a perfect sphere, their size can be calculated from the hydrodynamic diameter (R_H) obtained from the Stokes-Einstein equation (1) where K_B= *the* Boltzmann constant, T= temperature in K, η= viscosity (Stetefeld et al. 2016):

$$D_f = \frac{k_B T}{6\pi\eta R_H} \tag{1}$$

DLS measurements were carried out on a Zetasizer Nano ZS or Ultra and the hydrodynamic diameter data was analyzed with the corresponding Zetasizer software. Liposome and proteoliposome samples were diluted in respective liposome buffer (1:10) and 500 µL were transferred to a 10 mm path length cuvette. After an equilibration time of 2 min at 37 °C measurements were performed at a detector angle of 173° with a refractive index of 1.45 and absorption of 0.001 with standard solvent parameters as referred to water or PBS. Each measurement included at least 10 runs and was repeated three times.

In addition to size measurements, the same instrument can measure the charge of small particles. Therefore, zeta potential was calculated for nanoparticle experiments. Charged ions produce an electrical double layer comprising Stern layer (containing oppositely charged ions as the particle) and the diffuse layer (containing both oppositely and same ion species). By applying an electric field, the charged particles move towards the counter electrode, which is affected by the diffuse layer, where the zeta potential describes the potential at this particle-dispersant interface. Here, the Hückel approximation is used, which assumes that the electrical double layer is thicker than the particle (Bhattacharjee 2016).

Zeta potential measurements of nanoparticles were performed in disposable folded capillary cells with an equilibration time of 2 min at 37°C. The intensity of the backscatters 638-nm-laser beam of four independent samples was measured in automatic mode. The electrostatic stability of the colloidal suspension *via* zeta potential measurements was carried out with 20 runs and three measurements in monomodal mode with a maximum voltage of 10 V.

3.5. Activation of integrin

Experiments of integrin activation, that are described in the following chapters, were carried out with several techniques. The conformation specific antibody PAC-1 only binds to the active conformation of integrin αIIbβ3 (Taub et al. 1989) and is used as a marker for active integrin. Activation was attempted to be induced with divalent ions or with different clinically relevant drugs.

3.5.1. Flow cytometry of liposomes

This high-throughput technique is explained more detailed in Chapter 3.6.4. For the validation of successful integrin reconstitution into liposomes flow cytometry experiments were carried out. For integrin detection, the monoclonal antibodies anti-CD61-Alexa 647 and anti-CD41 were used. For antibody binding, 10 µL of purified PE CF-fluorescently labelled liposomes were mixed with 1 µL of 200 µg/mL anti-CD61-Alexa 647 and 1 µL of 500 µg/mL anti-CD41 for 30 min at RT. Afterwards, the anti-CD41 antibody samples were incubated with 1 µL of the secondary goat anti-mouse IgG-Alexa Fluor 647 antibody for 10 min at RT. Samples were then diluted with 290 µL liposome buffer and analyzed in a BD LSR II Flow Cytometer. By addition of 1 µL of 100 mg/mL conformation-specific Alexa 647-labelled PAC-1 IgM antibody to PE CF-liposomes in buffer, with 1 mM $MnCl_2$ (control for activation) or EDTA (negative control) integrin activation was detected. The FlowJo 7.6.5 software was used for evaluation. Gating strategy is described in Figure S1.

3.5.2. Quartz crystal microbalance with dissipation (QCM-D) monitoring

QCM-D theory. Quartz crystal microbalance with dissipation (QCM-D) monitoring is a real time and label-free technique to characterize the mass and viscoelastic properties of an adsorbed layer on a crystal. With a mass sensitivity in the ng/cm^2 range in liquid it can be utilized for a broad range of research fields (Höök et al. 1998), such as membrane-protein (Marx 2003) or protein-protein interactions (Oom et al. 2012). Additionally, QCM-D has been shown to be a useful tool to study the formation of supported lipid bilayers (SLB) (Richter et al. 2003).

This biophysical technique uses acoustic waves generated by an oscillating piezoelectric quartz crystal, by applying an electric field to the quartz, which is sandwiched between two electrodes. When a sufficient voltage is applied close to the resonant frequency (f_0 = *5 MHz*) of the crystal, it results in oscillation and several harmonics (n = 3,5,7,9,11,13). The linear relationship between changes in the frequency of the oscillation (Δf) due to adsorbed mass (Δm) on the surface of the crystal was demonstrated by Sauerbrey in 1959 (Sauerbrey 1959) and is given by equation (2):

$$\Delta m = -\frac{C}{\mathrm{n}}\Delta f \qquad (2)$$

Where n is the harmonic number and

$$C = \frac{t_q \rho_q}{f_0} \tag{3}$$

With t_q is the thickness of the quartz and ρ_q being the density of the quartz. To hold the Sauerbrey relationship three assumptions must be fulfilled. First, the adsorbed mass has to be smaller relative to the mass of the crystal. Second, the adsorbed mass is rigid and third, the adsorbed mass is consistently distributed over the surface of the crystal. For viscous and elastic contributions, which is mostly the case for studies with liquid phases, the Sauerbrey assumption cannot be hold. Therefore, dissipation (*D*) monitoring of the mass deposits with viscoelastic character is addressed to interpret the data. The decay of a crystal's oscillation occurs when the applied voltage is stopped and the softness of the adsorbed material dampens the crystals remaining oscillation. *D* is defined as:

$$D = \frac{E_{Dissipated}}{2\pi E_{Stored}} \tag{4}$$

With $E_{dissipated}$ being the energy dissipated during one oscillatory cycle and E_{stored} being the energy stored in the oscillating system (Dixon 2008).

Experimental details. QCM-D measurements were carried out with a Q-sense Analyzer under continuous flow of 25 µL/min driven by a peristaltic pump at 37 °C. The SiO_2-coated quartz crystal sensors were cleaned using a 2 % SDS solution for at least 30 min at RT followed by rinsing with ultrapure water. Then, crystals were dried under a stream of nitrogen and exposed for 20 min to UV-ozone. Resonance frequency and dissipation were measured at several harmonics (15, 25, 35, 45, 55, 65 MHz) simultaneously. Changes in dissipation (ΔD) and frequency (Δf) of the seventh overtone (35 MHz) are presented in the QCM graphs. After equilibration of the system with liposome buffer (15 min), liposomes or proteoliposomes were injected into the system. After surface adsorption, the system was washed for at least 20 min with liposome buffer. For integrin activation experiments, liposome buffer containing 1 mM $MnCl_2$ or 5 mM EDTA was loaded into the system and incubated under continuous flow for approximately 1 h. PAC-1 was finally added at a concentration of 5 µg/mL for interaction analysis followed by rinsing with the respective buffer.

For drug interaction analyses, Mn^{2+} treatment was replaced by clinically relevant drugs: 250 µg/mL UFH, 250 µg/mL fondaparinux or 50 µg/mL quinine sulfate diluted in liposome buffer were introduced into the system for 10 min after washing and PAC-1 injection was performed, subsequently. Measurement with different lipid ratios of DOPC, SM and cholesterol was adapted by usage of 13 µM α-helical (AH) peptide to force vesicle fusion (Cho et al. 2007b).

For QCM measurements with nanoparticles, the system was changed to PBS buffer due to enhanced aggregation of nanoparticles in other buffer systems. After equilibrating the system with PBS buffer for 10 min, liposomes or proteoliposomes were injected into the system as described above. After bilayer formation, the system was treated with PBS buffer containing 1 mM $MnCl_2$, 1 mM $MgCl_2$ and 1 mM $CaCl_2$ and incubated under continuous flow for approximately 30 min. NPs or purified bioconjugates were added (~2 x 10^{11} citrate particles/mL, ~5.8 x 10^{10} dextran-modified/mL and ~6.5 x 10^{10} PEG-particles/mL) followed by rinsing with the respective PBS buffer. Data analysis was achieved using Q-Tools V.3.0 and QSoft401 V2.5. Frequency and dissipation changes of the 7th overtone between time of injection (Δf_7inject; ΔD_7inject) of PAC-1 or NPs and 10 min after rinsing with buffer (Δf_7rinse; ΔD_7rinse) were calculated as shown in (5):

$$\Delta f_7 inject - \Delta f_7 rinse = \Delta f \quad \text{and} \quad \Delta D_7 inject - \Delta D_7 rinse = \Delta D \qquad (5)$$

The difference is plotted as Δf or ΔD in the respective graphs.

3.5.3. Nanoparticle synthesis and modification

Nanoparticle synthesis was performed as described by Martens and Janke et al. (Martens et al. 2020). Briefly, a mixture of 20 % ammonium hydroxide, 1.8 mol ferric and ferrous chlorides was oxidized by addition of a 1.3 mol iron nitrate solution and heated to 80 °C. After washing and suspension in 2 M nitric acid solution, the mixture was magnetically decanted and 5 % nitric acid were added and stirred for 10 min. For citrate coating, sodium citrate was added with a molar ratio of Fe/Citrate = 0.13 and heated to 80 °C for 30 min followed by decantation and suspension in water.

3.5.4. Activation assay

Activation assay for proteoliposomes was performed following a protocol adapted from Ye et al. (Ye et al. 2010). Anti-human CD41/61 PAC-1 antibody (PAC-1 antibody) was coated on a 96 well microtiter plate at 4 °C overnight. Afterwards, the plate was blocked with liposome buffer containing 30 mg/mL bovine serum albumin and PE CF-fluorescently labelled liposomes or proteoliposomes were added under different conditions, which are indicated in the respective graphs. The plate was then incubated for 4 h at 37 °C and unattached liposomes were washed away with liposome buffer. After addition of 100 µL 1 % Triton X-100 in liposome buffer, fluorescence was detected in a microplate reader at ex485/em535 nm. The respective liposome fluorescence signal was subtracted from the proteoliposome signal.

3.5.5. Molecular dynamic simulations (MDS)

Integrin model. MDS were carried out following a published protocol (Janke et al. 2019). Briefly, a complete model was built from the X-ray structure of the ectodomain (PDB-code: 3fcs), the NMR structure of the transmembrane domain (PDB-code: 2k9j) and missing residues were added as random coil (Zhu et al. 2008), as well as modifications such as glycosylations and ions were considered. After energy minimization, overstretched bonds were relaxed. The integrin was then embedded in a DMPC:DMPG (20:1 ratio) membrane equilibrated for 350 ns in an isothermal-isobaric (NPT) ensemble. An open conformation of integrin was obtained with steered MD by constant velocity pulling.

Detailed simulation parameters are described by Janke et al (Janke et al. 2019). For the simulation of the ion effect on the integrin structure the following conditions were tested: i) seven Ca^{2+} and one Mg^{2+} ion as present in the X-ray structure (Zhu et al. 2008), ii) three structural ions in the proximity of the active center were replaced with Mn^{2+}, and iii) all structure ions were removed. Each system was first equilibrated for 350 ns in the NPT, followed by 100 ns production trajectory, and conformations were collected every 700 ps. The structural distribution and MDS secondary structure were analyzed and predicted with the AmberTools program CppTraj (Roe and Cheatham 2013) over the whole trajectory.

3.5.6. Circular dichroism (CD) spectroscopy

CD-theory. CD spectroscopy is a biophysical method to determine the secondary and tertiary structure of proteins in solution due to their chirality. Differential absorbed left (L)- and right (R)-handed circularly polarized light by chiral molecules leads to an elliptical polarized radiation as long as its difference in absorption (ΔA) is not zero (Kelly et al. 2005):

$$\Delta A = A_L - A_R \tag{6}$$

The difference in A, which is elliptical polarized radiation, is measured as ellipticity (θ) in degrees, both have a numerical relationship namely (Kelly et al. 2005; Johnson 1988):

$$\theta = 32.98 \cdot \Delta A \tag{7}$$

The CD spectrum is obtained when the dichroism is measured as a function of wavelength. The intensity of the CD signal is directly proportional to the concentration (c) of the determined protein and the pathlength (d), which is characterized by the Lambert-Beer law (Kelly et al. 2005; Swinehart 1962):

$$\Delta A = \Delta\varepsilon \cdot c \cdot d \quad \text{with } \Delta\varepsilon = \varepsilon_L - \varepsilon_R \tag{8}$$

Here, the specific extinction coefficient ($\Delta\varepsilon$) is the difference between the one from left (ε_L) and right polarized light (ε_R).

A CD signal can be negative or positive and is observed when a protein is optically active mostly due to the amide chromophores of the peptide bonds. The chiral center contains a C atom with four different substituents (below 240 nm). Additionally, proteins comprise also aromatic amino acids (260-320 nm) or disulfide bonds (~260 nm), that absorb at different wavelengths and the sum results in specific protein structures that give a unique CD signal. Far UV spectra (180-260 nm) associate with various types of secondary structures such as α-helix, β-sheets or random-coil (Figure 8). Besides, spectra in the region 260-320 nm arise from the aromatic amino acids and can indicate changes in the tertiary structure (Kelly et al. 2005; Miles and Wallace 2016).

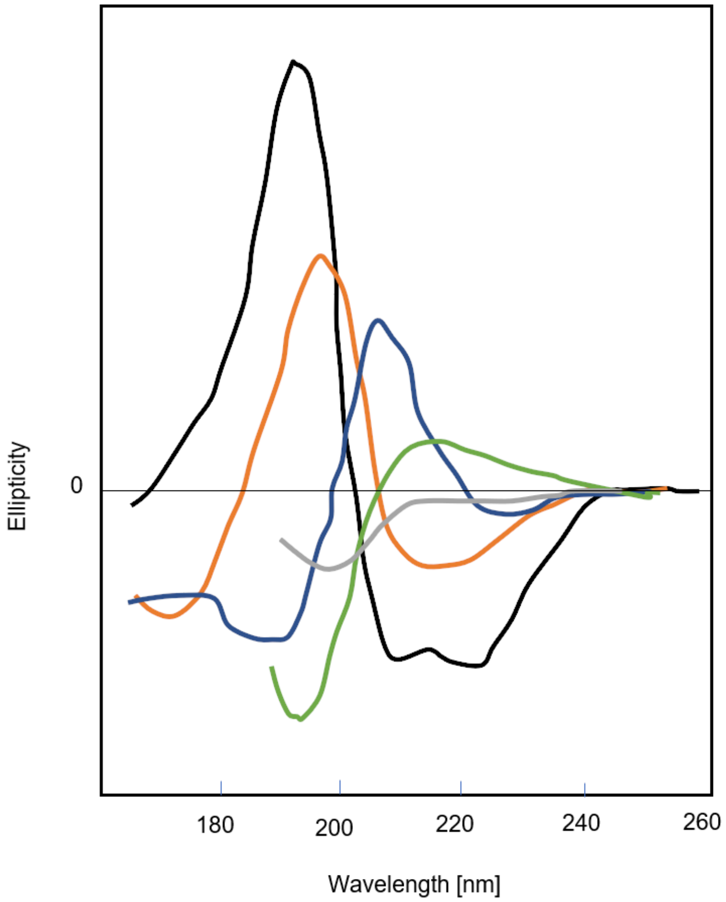

Figure 8: Far UV CD spectra associated with various types of secondary structure. Black curve-α-helix; orange curve-anti-parallel β-sheet; blue curve-type I β-turn; green curve-extended 31-helix or poly (Pro) II helix; grey curve-irregular structure. Adapted from (Kelly et al. 2005).

In this PhD thesis, CD experiments were carried out for determination of secondary protein structural changes upon treatment with different ions and drugs.

Experimental details. CD spectra were measured in a Chirascan CD spectrometer equipped with a temperature control unit at 37 °C. A 5 mm path length cuvette with integrin concentration of 0.4 µM incorporated into liposomes was used for measurements at wavelengths in the range of 195-360 nm. Spectra were recorded with a bandwidth of 1.0 nm, a scanning speed of 15 nm/min and three repetitions. Spectra of liposomes were subtracted from proteoliposomes for the data analysis. For determination of Mn^{2+}- and EDTA- induced changes in the secondary structure of αIIbβ3, the sample was first measured in liposome buffer, afterwards $MnCl_2$ was added to a final concentration of 1 mM and the sample was incubated 45 min before measurement. Next, 50 mM EDTA was added to the same cuvette to a final concentration of 5 mM and incubated for 45 min at RT. For drug treatment experiments, respective volume of UFH (0-295 µg/mL), fondaparinux (0-122 µg/mL) or quinine sulfate (0-1.5 µg/mL) were titrated to the cuvette and equilibrated for 5 min at 37 °C before each measurement. Normalization of the data was calculated by the wavelength dependent mean residue delta epsilon (MRDE) that consists of concentration *c*, number of amino acids *AA*, path length of the cuvette *d* and the constant resulting from the conversion of differential absorbance to ellipticity:

$$MRDE = \frac{CD\ [mdeg]}{c[M] \times AA \times d[cm] \times 32{,}982} \tag{9}$$

3.6. HEK293 cells as integrin expression platform

3.6.1. Cell culture and transfection

Human embryonic kidney cells (HEK293), wild type (WT) integrin $\alpha_{IIb}\beta_3$ expressing HEK293 cells (HEK αIIbβ3 WT) and its mutants HEK293 αIIbβ3 active (C560R) (Ruiz et al. 2001), as well as HEK293 αIIbβ3 inactive (β3-R563C/αIIb-R320C) (Takagi et al. 2002) were grown in T25/T75 cell culture flasks in DMEM with high glucose concentration supplemented with 10 % FCS, 1% Pen-Strep and 1% L-glutamine at 37°C and 5% CO_2 atmosphere. Media for integrin WT and mutant expressing cells contained 2.5 mg/mL G-418 additionally. Cell passaging was performed three times a week. The medium was removed and cells were washed with 5 mL PBS, followed by digestion with Trypsin/EDTA. After 2 min, detachment of the cells was stopped by addition of cell culture medium. The cell suspension was centrifuged at 250 x g for 5 min and 10^5 cells/mL were resuspended in an appropriate amount of fresh media, respectively. For cell counting, 10 µL of the cell suspension were mixed with 90 µL Trypan Blue and transferred into a Neubauer chamber and cell number per mL was calculated according to the following equation:

$$\frac{(cells\ counted)}{4} \cdot 10\ \cdot 1000 = {}^{cells}/_{mL} \tag{10}$$

For transfection experiments, lipofection was carried out with TransIT-LT1 transfection reagent, where the complex consisting of plasmid DNA and lipids forming liposomes enters the cells. This technique is used to introduce purified nucleic acids, especially plasmid DNA, into eukaryotic cells, resulting in expression of the favored protein *via* translation and transcription. For this purpose, HEK293 cells were seeded in a 24-well plate, in such a way that they were grown sub-confluently (70 %) at the moment of transfection. Further procedure followed manufacturer's instructions and the cells were transfected with the vectors pcDNA 3.1. *ITGA2B* WT, pcDNA 3.1 *ITGB3* WT, pcDNA3.1. *ITGA2B* R320C, pcDNA3.1. *ITGB3* C560R and pcDNA3.1. *ITGB3* R563C, respectively. After the transfected cells were grown for 24 h, selection media containing 2.5 mg/mL G-418 replaced the regular media (all expression plasmids used in this work contain a G-418 resistance sequence as selection marker). For generation of a homogenous cell line fluorescence activated cell sorting (FACS) was carried out (Chapter 3.6.4).

3.6.2. Mutagenesis and isolation of plasmid DNA

Mutagenesis of integrin αIIbβ3 plasmid DNA

For the generation of HEK293 cells expressing integrin αIIbβ3 wildtype (WT) as well as for the mutants HEK293 αIIbβ3 active and HEK293 αIIbβ3 inactive several plasmids were used.

The constructs pcDNA3.1(-)GPIIb and GPIIIa, which were a kind gift from Prof. Karen Vanhoorelbeke, were used as templates for the mutagenesis. First, polymorphisms in the GPIIIa plasmid (c. 1043G>A/p. R348Q [M1] and c. 1459G>A/p. A487T [M2]) were mutated back to the WT NCBI sequence ID: NM_000419.4), from now on namely pcDNA 3.1 *ITGA2B* WT. For the constitutively active integrin construct, the mutation C560R (Ruiz et al. 2001) was introduced in pcDNA3.1 *ITGB3* WT plasmid. For the constitutively inactive integrin, two mutations were inserted: R563C to the *ITGB3* WT plasmid and R320C to the *ITGA2B* plasmid resulting in the mutant constructs pcDNA3.1. *ITGA2B* R320C and pcDNA3.1. *ITGB3* R563C respectively (Takagi et al. 2002).

Mutagenesis is used for the introduction of targeted mutations in the plasmid DNA sequence and was performed with the QuikChange II Site-Directed Mutagenesis Kit following manufacturer's instructions. The utilized primers are listed in Table 3.

Table 3: Mutagenesis and Sequencing Primer Sequences.

Name	Sequence 5'-3'
ITGB3 R563C forward	TACTGCAACTGTACCACGTGTACTGACACCTGCAT
ITGB3 R563C reverse	ATGCAGGTGTCAGTACACGTGGTACAGTTGCAGT
ITGB3 C560R forward	GACCGGCTACTACTGCAACCGTACCACGCGTACTG
ITGB3 C560R reverse	CAGTACGCGTGGTACGGTTGCAGTAGTAGCCGGTC
ITGA2B R320C forward	ATGGAGAGCCGGGCAGACTGTAAACTGGCCGAAGT
ITGA2B R320C forward	ACTTCGGCCAGTTTACAGTCTGCCCGGCTCTCCAT
ITGA2B M1 forward	CTGTATATGGAGAGCCGGGCAGACCGAAAACTG
ITGA2B M1 reverse	CAGTTTTCGGTCTGCCCGGCTCTCCATATACAG
ITGA2B M2 forward	CAGCCAGTGGTGAAGGCCTCTGTCCAGCTAC
ITGA2B M2 reverse	GTAGCTGGACAGAGGCCTTCACCACTGGCTG
ITGA2B-F1	CCTCTCCTTTGACTCCAGCA
ITGA2B-R1	CAAAATTTCCACCGCTCCCA
ITGA2B-F2	TCGAGATGAGGCAGACTTCC
ITGA2B-R2	GGCACACATACGTCATCTTC
ITGA2B-F3	GTGAATGGTCTTCACCTCAG
ITGA2B-R3	CAGCTTACGAGAACTGGATC
ITGB3-R1	ACTGACTTGAGTGACCTGGG
ITGB3-F1	GCAGGCTACAGTCTGTGATG

ITGB3-R2	GCAGGCACAGTCACAATCAA
ITGB3-F2	CCCTGGCCTCAAGTCTTGTA
ITGB3-F3	TGACGACTTCTCCTGTGTCC
ITGB3-R3	CTACCACATACAGGATGGAC
bGH-R	TTGTCTTCCCAATCCTCCCC
T7	TAATACGACTCACTATAGGG

The mutagenesis polymerase chain reaction (PCR) contained the ingredients listed in Table 4.

Table 4: PCR reaction mixture.

Template DNA	40 ng
dNTPs	1 µL (10 mM)
5x amplification buffer	5 µL
Mutagenesis primer fw	10 pmol
Mutagenesis primer rev	10 pmol
Polymerase	1 µL
DMSO	5 µL
Deionized water	To 50 µL

The reaction mixture was shortly mixed and incubated in a thermocycler as shown in Table 5.

Table 5: PCR conditions

Step	Temperature	Time	Cycles
Denaturation	95 °C	30 sec	1
Denaturation	95 °C	30 sec	16
Annealing	55 °C	1 min	
Elongation	68 °C	8 min	
Cooling	4 °C	Infinite (not longer than 12 hours)	1

Afterwards, the reaction mixture was incubated with 1 µL of the restriction enzyme *DpnI* to remove the template DNA, which is *dam*-methylated, different from the new amplified DNA. Finally, the mixture was transformed in *Escherichia coli* (*E. coli*) NEB 5 alpha.

Transformation in competent *Escherichia coli*

During transformation, free DNA is introduced to competent bacterial cells. For this purpose, competent *E. coli* (NEB 5 alpha) were thawed on ice for 10 min and mixed with 1 µL of the *DpnI* digested PCR reaction solution for 30 min. After a heat shock at 42 °C for 30 s the mixture was incubated on ice for 5 min. Next, 950 µL LB-Media was added and incubated at 37 °C for 1 h. Finally, 10, 100 and 500 µL were added to LB-agar plates containing 100 µg/mL of the selective antibiotic ampicillin (Amp) and incubated overnight at 37 °C. Grown colonies were picked, transferred to 2 mL LB-media and incubated at 37 °C in a bacterial shaker overnight.

Plasmid DNA isolation and sequencing

Plasmid DNA was isolated directly from the transformed bacteria after growing overnight in LB-Media supplemented with ampicillin by the GeneJET plasmid Miniprep Kit following manufacturer's instructions. 500 µL of the remaining bacteria culture were frozen in 25 % glycerol at -80 °C. The obtained plasmid DNA was sent to Microsynth SEQlab GmbH (Göttingen, Germany) and the sequence was verified by Sanger-Sequencing by usage of the primers mentioned in Table 3. Results were evaluated using Snapgene. When the desired mutations were introduced, 250 mL LB Media with Amp were inoculated with 500 µL of overnight culture and incubated at 37 °C in a bacterial shaker overnight, to obtain more plasmid DNA for further experiments. The plasmid DNA was isolated by usage of the PureLink HiPure Plasmid Maxiprep Kit following manufacturer's instructions. Concentration of the prepared plasmid DNA was determined with a spectrophotometer (A260 nm) and DNA was stored at -20 °C.

Agarose gel electrophoresis

DNA fragments can be separated by their size *via* agarose gel electrophoresis. Therefore, DNA sample with loading dye (0.03% bromphenol blue, 0.03 % xylene cyanol FF, 30 % glycerol, 10 mM Tris HCl, 50 mM EDTA) was loaded onto a 1 % agarose gel mixed with 0.5 µL DNA Stain G. The fragments were separated by 100 V for 50 min in a mini electrophoresis system with 1 x TAE buffer (40 mM Tris, 1 mM EDTA, 20 mM acetic acid, pH 8). For guidance, a DNA ladder (GeneRuler 1 kb) was also loaded onto the gel. Finally, the gel was imaged under UV-light in a Gel Dock XR imaging system.

Restriction digestion

Restriction endonucleases cut DNA at specific sequences and enables thereby the evaluation of produced Plasmid DNA. The batch was mixed as follows:

Template DNA	4 µL
10 x Buffer 2 or Buffer 4	2 µL
Enzyme	1 µL
Deionized water	13 µL

Buffer was applied following manufacturer's instruction for the respective enzyme. The mixture was incubated for at least 1 h at 37 °C. Afterwards, the samples were loaded onto an agarose gel for electrophoretic separation.

3.6.3. Confocal microscopy

Confocal microscopy theory. The confocal microscopy provides various advantages towards conventional light microscopy such as a controlled strait focus depth and the removal of non-focused light. A laser is reflected by a dichroic mirror and focused on the specimen through a water or oil immersion objective. Fluorescent or reflected light is collected by the same objective lens and directed through the detector. A pinhole allows only in focus light and eliminates the scattered out-focused light, which reduces the background generally. Several layers can be imaged which enables the depiction of 3D objects (Diaspro 2002).

Sample preparation. The cells were grown on 8 well µ-Slides, incubated 20 min with media or media containing 1 mM $MnCl_2$. Then cells were washed three times and fixed using 4 % paraformaldehyde for 30 min at RT. Afterwards, cells were permeabilized for 4 min with 0.1 % Triton X-100. 3 % BSA blocking solution was added for 30 min, followed by addition of respective primary antibody for 1 h at RT. Secondary antibody was then added in the dilutions indicated in the graphs for 45 min. Samples were washed in between the incubation steps three times with PBS containing 0.05 % Tween-20, respectively. Finally, slides were covered with PBS and visualized in a Leica TCS Sp5 confocal microscope. The representative pictures were taken at 40x magnification and 5x zoom. Picture assessment was performed with GIMP 2.10.14.

3.6.4. Flow cytometry and fluorescence-activated cell sorting (FACS)

FACS theory. Differently from the microscope, a flow cytometer quantifies a set of parameters from particles or cells in suspension in a high-throughput manner. Fluorescently-labeled suspended particles in a continuous flow pass a beam of light of a single wavelength performed by optical filters that block certain wavelengths. Thereby, every particle scatter in a distinct way the light, that is detected by a photodiode as well as a photomultiplier tube and converted into electrical signals. Additionally, the conjugated fluorescent substance emits, after excitation, light which can be detected as well. Therefore, flow cytometry is applied for research, but also for various diagnostic tests in the clinics.

According to morphological and structural characteristics, the light is scattered differently: the forward scatter (FSC) is associated with the cell size, whereas the lateral side scatter (SSC) depends on the cytoplasmic granularity of the cell. Fluorescent light, e.g. bound monoclonal antibodies conjugated with a fluorophore, is emitted and a series of lenses collects the scattered light (Errante 2016).

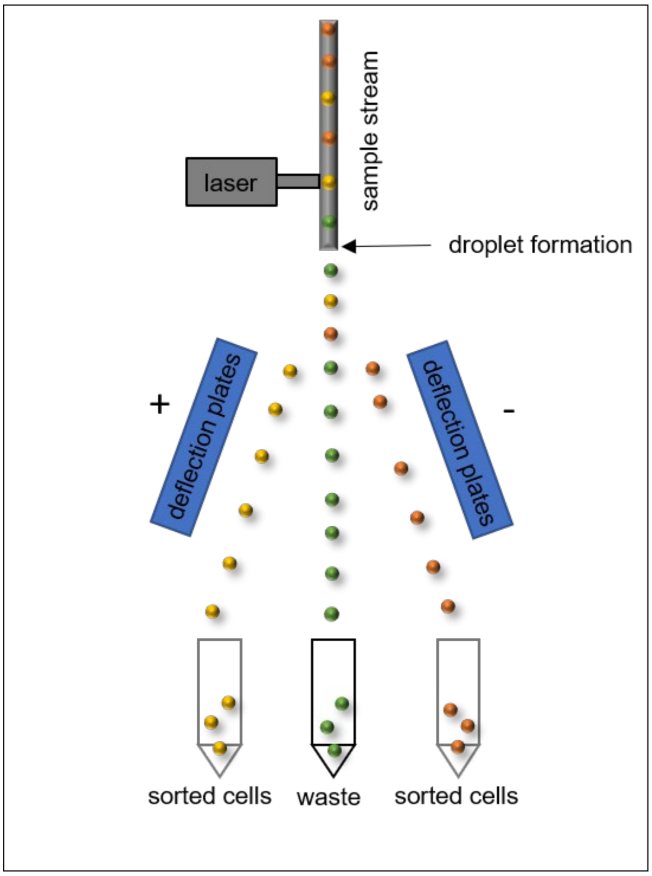

Figure 9: FACS setup. Adapted from (Rowley, 2012).

In order to sort cells, a gate is applied to the desired population of cells. By usage of a conductive sheath fluid, the sample stream is vibrated in the moment it exits the nozzle, causing stream brake- up into droplets with each containing one cell (Figure 9). Negatively and positively charged plates on either side of the stream cause deflection of the droplets that meet the sorting gate criteria by applying of charge. The cells are collected in specific containers and can be used for further experiments. Cell sorting enables the synthesis of homogenous cell culture samples with a high degree of purity (Rowley 2012).

Sample preparation of cells. Cells were incubated on a 6-well plate with media, activation medium containing 1mM $MnCl_2$, or activation media with added 5 mM EDTA for 20 min and detached with Trypsin/EDTA for 2 min. After stopping detachment with media, the sample was transferred into a FACS tube and centrifuged at 250 x g for 5 min. The supernatant was discarded and the pellet washed with PBS and centrifuged at 250 x g for 5 min. Next, pellet was solved in 300 µL PBS and fluorescently-labeled antibodies were added according manufacturer's instructions for 15 min. Finally, the sample was washed with PBS and measured in a BD LSR II flow cytometer.

For sorting experiments 1 x 10^5 CD41 and CD61 positive (+) cells were collected in a BD FACS Aria III and seeded in a 12-well plate for further experiments. Sorting was carried out until a 98% homogenous cell culture was reached. Respective antibodies are indicated in the graphs. Evaluation of the data was carried out using the software FlowJo V10. First, the cell region was marked in the side scatter area (SSC-A) *versus* front scatter area (FSC-A) plot. Then, the cells were pictured in the front scatter height (FSC-H) *versus* FCS-A plot. Afterwards, from the single cells, the mean fluorescence intensity was plotted by using the histogram of the corresponding fluorescence channel. Data processing is representatively demonstrated in Figure S2.

3.6.5. Atomic force microscopy (AFM)

AFM theory. The AFM was invented in the 1980s by Binnig, Quate and Gerber and has become a relevant tool in different research fields such as surface science, material science or medical biology. This imaging technique allows resolution of surfaces on atomic level. Basically, a sharp tip mounted at the end of a cantilever, scans the surface of the sample line-by-line. Thereby, the cantilever is deflected and a feedback system adjusts the distance between sample and cantilever tip to keep a constant deflection. According to Hook's law, a force is needed to extent the spring with a specific spring constant *k*, and the distance that is extended *x* depends linearly on the applied force *F* (Giuliodori et al. 2009):

$$F = k \cdot x \tag{11}$$

A laser beam is reflected from the back side of the cantilever onto a position sensitive photodetector (Figure 10). Deflection of the laser beam on the detector is utilized to measure the deflection of the cantilever. By plotting the deflection of the cantilever *versus* its position on the surface a three-dimensional image of the surface is obtained.

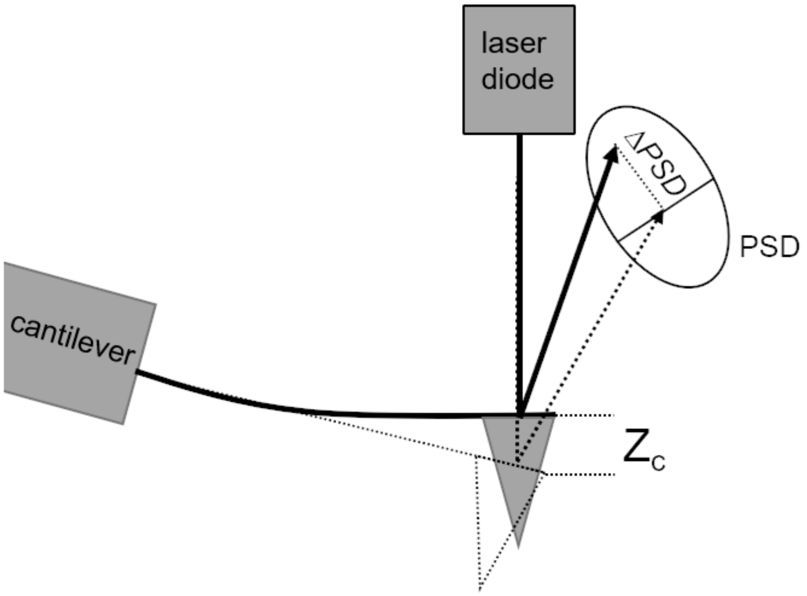

Figure 10: Schematic of the cantilever deflection. The position sensitive device (PSD) is indicated as a photodiode. ∆PSD is the distance of the movement of the the laser spot, Zc is the cantilever deflection. Adapted from (Butt et al., 2005).

Generally, two operating modes are used for imaging: the contact mode where the tip is in contact with the surface with a distance less than a few angstroms and the tapping mode, in which the tip is vibrating in its resonant frequency, due to its piezoelectric characteristics, with spacing to the sample of tens to hundreds of angstroms. The resonant frequency of the oscillation decreases as the sample is approached due to forces (e.g. van der Waals forces) that tend to be quite small in the range of 10^{-12} N, which in turn makes a non-destructive imaging possible (Butt et al. 2005).

Besides imaging of surfaces, AFM can be used to measure force-*versus*-distance curves. Here, the cantilever is moved towards the surface and retracted again. The vertical deflection is recorded and converted to a force-distance curve (Senden 2001; Maghsoudy-Louyeh et al. 2018; Butt et al. 2005).

By knowing the mechanical properties of the cantilever, sample elasticity (Young's Modulus-YM) can be calculated using the Hertz model. The Young Modulus is defined as the ratio between the applied forces (F) per unit surface to the material and its deformation. The higher the YM, the stiffer the material. The Hertz Model describes elastic deformation when an applied force causes an indentation depth when pressing a probe into a soft surface. It assumes: i) an isotropic and linear elastic solid having a half spherical shape, ii) the indenter must have a spherical shape and iii) the indented sample is assumed to be thicker in comparison to the indentation depth. The Poisson's ratio (ν) depends on the used material and is set to 0.5 for soft biological samples. Additionally, different indenter geometries (includes also α = face angle given by the cantilever) lead to different radii of the contact circle (R) and indention depth (δ).

The YM is calculated for spherical probes using the following equation (Kuznetsova et al. 2007; NanoWizard 2014):

$$F = \frac{YM}{1-\nu^2}\left[\frac{a^2+R^2}{2} ln\frac{R+a}{R-a} - aR\right] \tag{12}$$

$$\delta = \frac{a}{2} ln\frac{R+a}{R-a}$$

Even intra- and intermolecular forces of biomolecules can be measured when a tip is functionalized with biomolecules that interact with molecules on the surface. The required force to pull the interaction molecules apart can be determined and displayed in a force-distance curve (Figure 11).

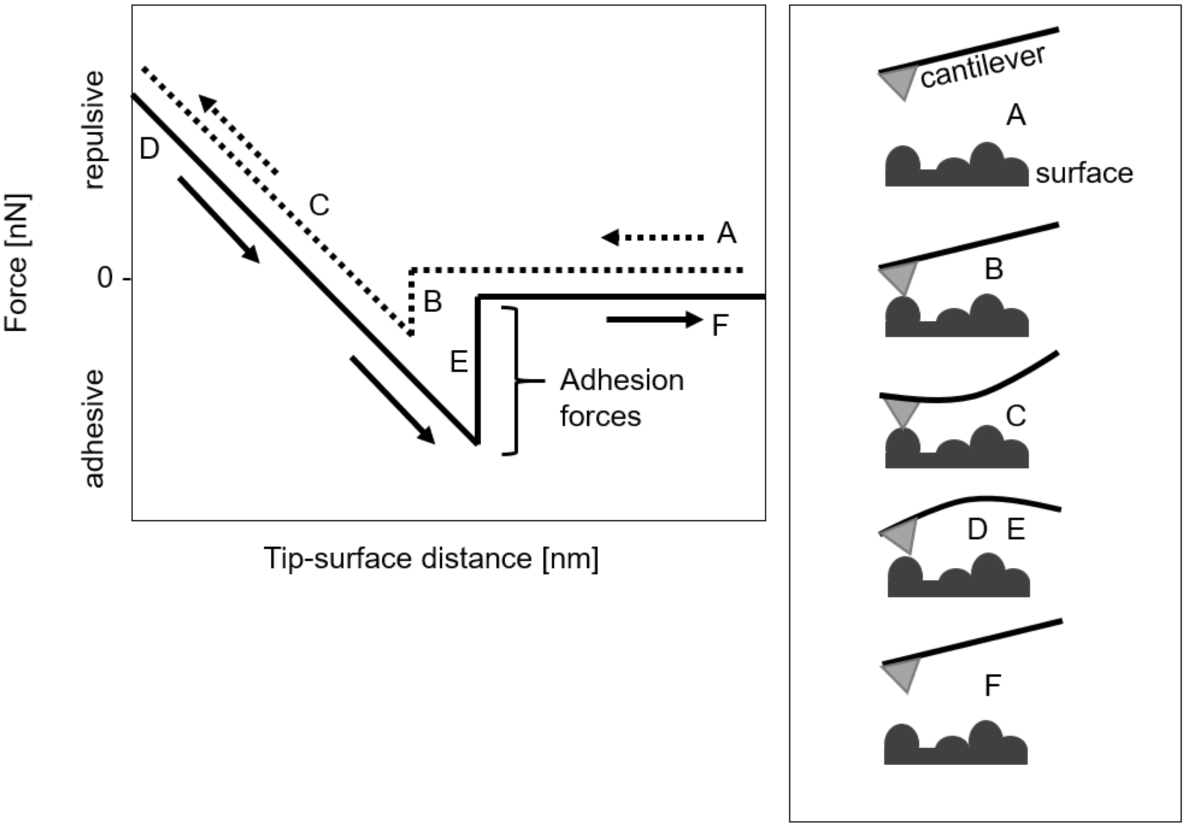

Figure 11: Ideal force-distance curve. Ideal force-distance curve describing a single approach-retract cycle of the AFM tip. The Cantilever is approaching the sample surface (A). The first contact between the tip and the surface is characterized by van der Waals forces that causes an attraction of the tip towards the surface (B). Thus, the tip applies a force upon the surface that causes to sample indentation and cantilever deflection (C). Then, the cantilever tries to retract and to break off from the surface (D). Various adhesive forces between the sample and the AFM tip impair tip retraction. The force-distance curves give the values of adhesive forces (E). The tip is removed and loses contact to the surface by exceeding the adhesive forces (F). Adapted from (Shahin et al. 2005).

Experimental details. All cell AFM experiments were performed by Theresa Brinker, Master student between 04.2019-06.2020 in the Biophysical Chemistry group of Prof. Delcea, at the University of Greifswald. For measurements, an AFM Nanowizard 3 AFM System with an inverted Olympus ix81 microscope was used.

5 µm silica beads were attached to a tip-less silicon cantilevers called colloidal probes. A thin stripe of UV glue was placed on a clean glass slide. The cantilever was dipped into the glue and excessive glue was removed by dipping on the glass surface. Afterwards, the cantilever was pressed onto a single silica bead in water. After the attachment, the glue was exposed to UV-light for 30 min for hardening. A side view image of the cantilever depicts effective attachment of the bead (Figure 12).

Glass slides where prior to use cleaned using RCA cleaning solution containing NH_3:H_2O_2: H_2O (1:1:6) at 70 °C for 10 min. Next, slides were rinsed extensively with water and dried under nitrogen. The cantilever was calibrated using mica surfaces with the JPK SPM Control Software using the thermal noise method, which allows the conversion of the nanometer deflection of the cantilever into force by usage of the Hooke's law (see equation 11). The thermal noise method plots the cantilever fluctuations as a function of frequency. At the resonance frequency, the cantilever will have the greatest amplitude and its curve can be fitted with a Lorentz function. Determined spring constants show a range provided by the manufacturer of 0.003 – 0.13 N/m.

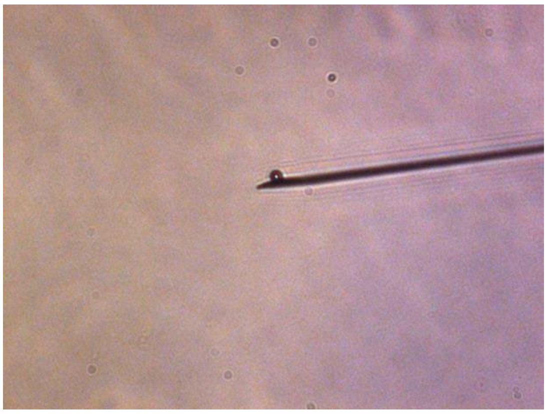

Figure 12: AFM cantilever with attached silica bead. Picture was taken by T. Brinker, Greifswald.

Force measurements were carried out with a force set point of 1 nN and a velocity of 5 µm/s on a 5x5 grid with 25 points across an area of 5x5 µm. Each measurement was repeated three times at RT before a new cell was selected. Force-*versus*-distance curves from at least 20 cells were acquired.

The cells were seeded in a 6-well plate containing the rinsed glass slides with a cell count of 1 x 10^6. For activation experiments with divalent ions, cells were incubated with 1mM $MnCl_2$, for 1 h at 37°C prior to measurement the AFM.

Measurements of sample surface topology were carried out in tapping mode AFM using the JPK AFM as well as Multimode AFM equipped with Nanoscope IIIa controller. For imaging in air Nanoscope AFM and OMCL-AC160TS cantilevers (42 N/m spring constant, 8 nm tip curvature) were used, while images in solution were recorded with JPK AFM and Econo-FESP-Au cantilevers (3 N/m spring constant, < 10 nm tip curvature). Alignment of AFM piezo scanners was confirmed by imaging calibration grating TGZ01 and TGG01. Image processing including line-by-line polynomial flattening and plane subtraction was carried out to account for sample tilting.

The AFM imaging of liposomes was carried out by Dr. Peter Nestler from the University of Greifswald. Tapping mode AFM images were taken in buffer solution after collapse of liposomes or proteoliposomes on a QCM crystal (SiO_2). Height profiles of the DMPG:DMPC bilayer before and after AFM tip-scratching were evaluated. The same area was imaged again after applying AFM tip-scratch technique. Therefore, a 3 µm x 3 µm subarea was scanned in AFM contact mode using 0.5 µN vertical force in order to reveal the QCM crystal surface. Afterwards tapping mode image of both samples before and after tip-scratching were scanned for an area of 10 µm x 10 µm for liposomes and 7 µm x 7 µm for proteoliposomes. Histograms of height distributions were evaluated using JPK software and are fitted using Gaussian distribution. JPK Data Processing software was used for AFM force curve processing. The force curves were fitted to the Hertz Model indicated above (12). Inadequately data fitting due to disturbed measurements were excluded from data processing.

3.6.6. Real time-deformability cytometry (RT-DC)

RT-DC theory. Cell deformability can be used as an indicator for changes in the cytoskeleton and enables a label-free method in various areas of research and diagnostics, e.g. cell cycle phase analysis or stem cell differentiation (Otto et al. 2015). In 2012, Gosset et al. showed a high-throughput deformability cytography technique (Gossett et al. 2012), which was advanced by O. Otto et al. three years later by processing the data simultaneously to the measurement (Otto et al. 2015). Cells were flown through a microfluidic channel constriction and deformed (Figure 13A). This deformation is illuminated with a pulsed high-power LED captured by a high-speed metal-oxide semiconductor camera and the shape change is further analyzed with an image analysis algorithm in the software. The results are displayed in a scatter plot with the deformation and the size of the cell (Figure 13B).

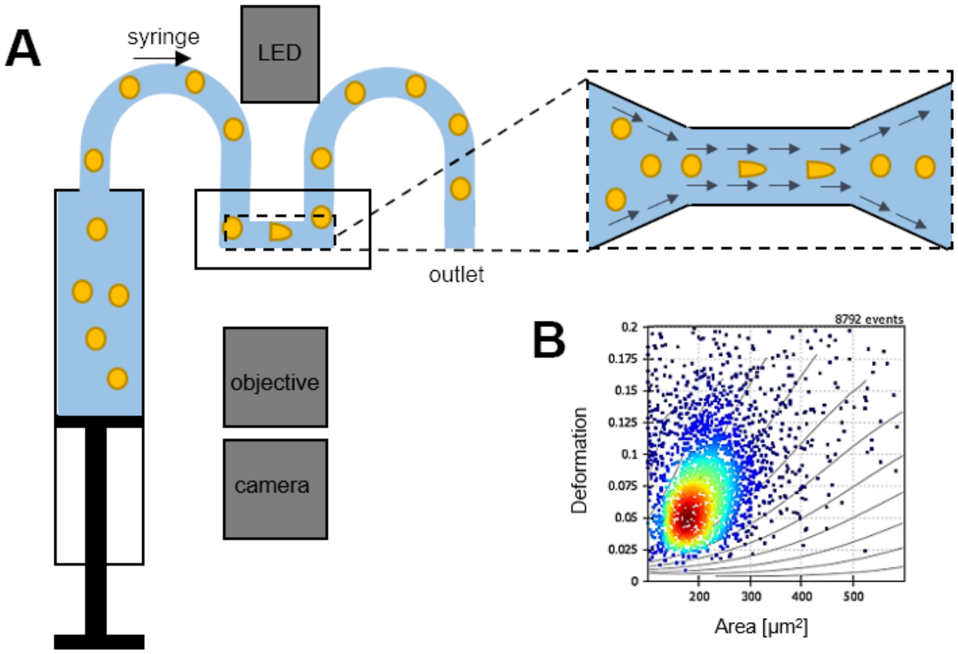

Figure 13: RT-DC setup. A) Setup and measurement principle (inset shows top view of constriction). B) Scatter dot plot of deformation *versus* cell size (cross-sectional area) of 8792 cells (dots). Color indicates a linear density of events. Adapted from (Otto et al. 2015)

Experimental details. For the RT-DC measurements, cells were transferred in cell carrier (<1% methyl cellulose in PBS) to adjust the viscosity. For this, cells were grown on 6 well plate and detached with trypsin/EDTA for 2 min. New media was added and cells were centrifuged at 250 x g for 5 min. The cell pellet was then resuspended in 80-100 µL cell carrier.

For activation experiments with divalent ions, cells were incubated with 1mM $MnCl_2$, or 5mM EDTA for 30 min prior to measurement in RT-DC.

Measurements were performed in a microfluidic chip with a 30 µm channel width. The sheath and sample tubes were added to 1 mL syringes and filled with cell carrier. Sample was then added to the chip. Once cells were detected in the flow channel, flow rate was set to 0.16 µL/s and measurements was taken, followed by a second measurement at 0.32 µL/s. Finally, measurements at the reservoir was carried out that acts as a shape control without shear stress. For data processing flow rate 0.16 µL/s was used.

RT-DC data was processed using the Shape-Out software. Upper limit for range area ratio is set to 1.05. The value refers to the ratio of convex hull area to cell area and all cells with a difference greater than 5% of those areas are excluded from further analysis. Young’s Modulus was calculated from analytical model within the Shape-Out software.

3.6.7. Statistical analysis

Statistical analysis was performed by Theresa Brinker, Master student between 04.2019-06.2020 in the Biophysical Chemistry group of Prof. Delcea, University of Greifswald. Analysis of processed AFM and RT-DC data was performed using R and RStudio. Data sets were collected and exported as .txt file for usage in R.

The 5th and 95th percentile were calculated and only data points inside these boundaries were used for further analysis.

For the use of linear mixed models (LMM), normal distribution of residuals is assumed by creation of Q-Q-Plot of the residuals. Best distribution of residuals in Q-Q-Plots was displayed after log-transformation. Therefore, statistical analysis was carried out with the linear mixed effects model with log-transformed data.

From fitted models, estimated marginal means (emmeans) were calculated. Emmeans correct imbalance by giving each group an equal weight, if data is imbalanced due to different groups with varying number of data points.

Statistical significance has been calculated on three experimental replicates carried out on separate measurement days. For LMM, a pair-wise comparison is performed where the data is split into a fixed effect, a random effect and random fluctuations. The fixed effects describe the statistical difference between two groups (e.g. control and treatments), whereas random effect and random fluctuations account for systemic and random influences such as heterogeneous cell populations or temperature fluctuations.

4. Results

4.1. Integrin αIIbβ3 in biomimetic systems

Integrin αIIbβ3 was reconstituted in a biomimetic membrane system, in particular liposomes, to allow studies under physiological conditions, as shown schematically in Figure 14. Subsequently, integrin was treated with ions, drugs or specific ligands and potential activation of integrin was determined by the binding of the conformation-specific IgM antibody PAC-1, which is only binding to the extended, opened integrin αIIbβ3 (Taub et al. 1989). For generation of the biomimetic system several steps were taken: i) pure integrin characterization, ii) bilayer formation of different lipids by vesicle fusion technique, iii) reconstitution of integrin into liposomes, and iv) integrin-containing lipid bilayer characterization on SiO_2 quartz crystals.

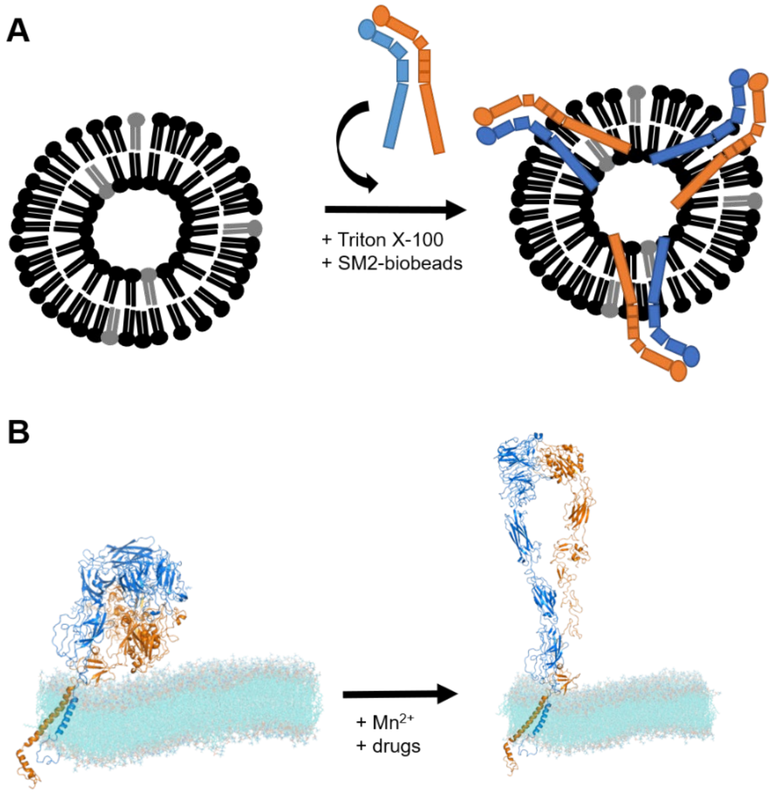

Figure 14: Schematic illustration of the proteoliposomes and structure of integrin αIIbβ3. A) Proteoliposomes after the reconstitution procedure. αIIbβ3 (αIIb-subunit in blue and β3-subunit in orange) is reconstituted into liposomes and treated with Triton X-100 as well as biobeads and used for further experiments. B) Structure of αIIbβ3 in bent (left) and open/active (right) conformation in a DMPG:DMPC (1:20) lipid membrane (cyan). The integrin model combines the αIIbβ3 transmembrane domain (PDB-code 2k9j) and ectodomain (PDB-code 3fcs), missing residues were added as random coils (αIIb-subunit in blue and β3-subunit in orange) Adapted from (Janke et al. 2019)

4.1.1. Integrin characterization

Pure integrin αIIbβ3 (commercially available) was characterized, prior to activation measurements, by several biophysical and molecular biology methods. Results are displayed in Figure 15. An ELISA assay with specific antibodies for the respective subunit was carried out and the results are shown in Figure 15A. For the αIIb-(CD41), as well as for the β3- subunit (CD61) the ELISA shows positive signal with an increasing absorbance up to 1 AU. The purchased antibodies have a different affinity to their respective subunits, which results in varying antibody concentrations to reach potential saturation of binding. Additionally, the presence of both subunits was verified by a reductive SDS-PAGE (Figure 15B). The protein migrated as two visible bands at 110 kDa (blue arrow; αIIb-subunit heavy chain) and 90 kDa (orange arrow, β3-subunit). Additionally, a band appears at 18 kDa. Moreover, protein stability was determined by heating the protein in HEPES buffer containing detergent. Thermal denaturation of proteins induces aggregation, which in turn, results in an increase in size, observed here at 50.4 °C (Figure 15C). The red line shows a fitting curve applied from the Thermal Denaturation Plugin from Origin software using a two-state denaturation model (Niklasson et al. 2015).

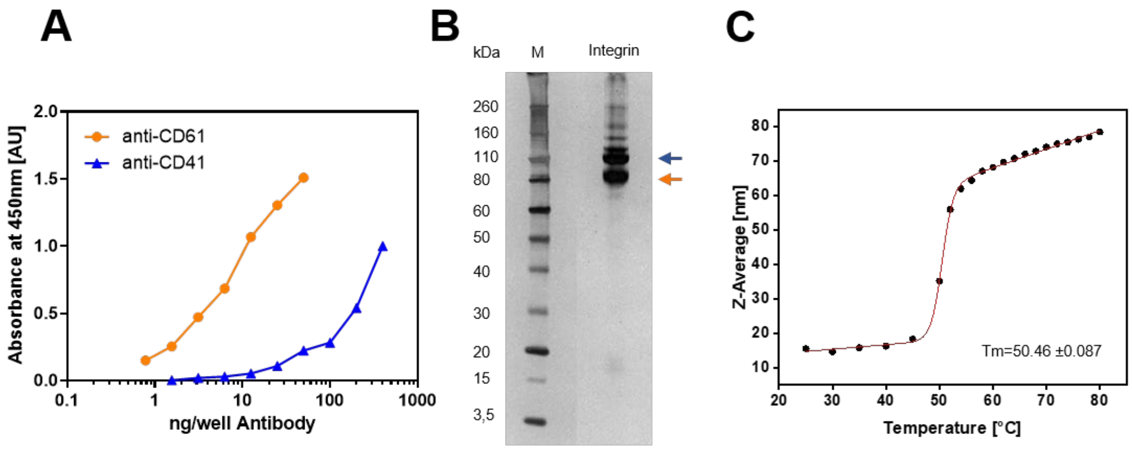

Figure 15: Pure integrin αIIbβ3 characterization. A) ELISA for αIIbβ3 integrin subunit detection. 100 ng/well integrin αIIbβ3 are coated on a microtiter plate and different dilutions of antibodies against αIIb-subunit (blue) and β3-subunit (orange) were added. B) Reductive SDS-PAGE gel of pure integrin protein showing protein molecular weight standard (M) and both integrin bands corresponding to the αIIb- (blue) and β3-subunit (orange) C) Protein stability measurements in Zetasizer Ultra. Z-Average of 0.5 mg/mL Integrin αIIbβ3 was measured with increasing temperature. For fitting, *ThermDena* denaturation plugin using a two-state model of Origin software was used.

4.1.2. Bilayer formation of liposomes with various lipidic systems

Integrin containing lipid bilayer should be treated with different drugs, ions or ligands and the integrin activation state was probed using the conformation specific PAC-1 antibody. For QCM-D activation experiments supported lipid bilayers (SLBs) can be formed *via* vesicle fusion technique. This makes the analysis of membrane proteins and their interaction behavior in a biomimetic system feasible.

For lipid bilayer formation on SiO_2 sensor crystals, first, several lipid compositions were examined for analysis of vesicle rupture events. Therefore, egg phosphatidylcholine (PC) and phosphatidylglycerol (PG) were mixed in different ratios and were run over a SiO_2 sensor surface (Figure 16). QCM-D detects mass adsorption (changes in frequency Δ*f*) and the viscoelastic properties (changes in dissipation Δ*D*) of adsorbed material. For an excess of PC

(PC:PG 4:1, Figure 16A) as well as balanced amounts of PC and PG (1:1, Figure 16B) the QCM-D graph show typical bilayer formation: after a baseline was reached liposomes show a strong binding to the SiO_2 substrate, as indicated by the decrease in Δf and increase in ΔD. Both changes reach a peak and then return back again oppositely to a stable value of Δf with -25 Hz and ΔD with 0.5 x 10^{-6} due to release of enclosed aqueous buffer. However, excess amounts of PG (Figure 16C) show a constant decrease in *f* that stabilizes at -150 Hz and an increase in *D* up to 36 x 10^{-6}.

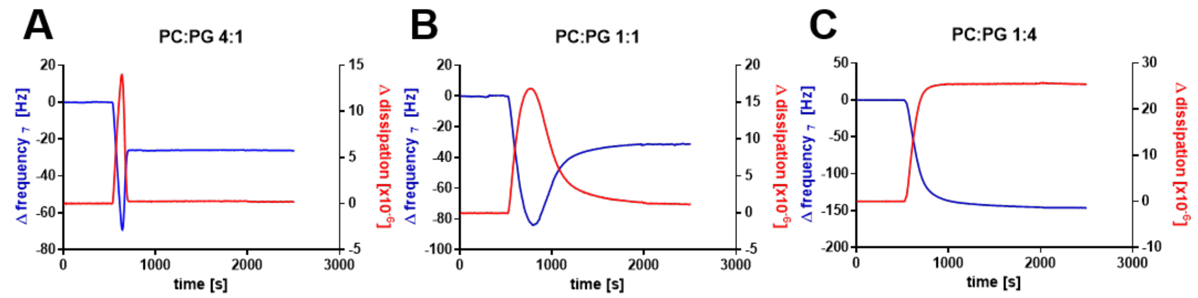

Figure 16: Representative QCM-D data showing the changes in frequency f (blue) and dissipation D (red) of the seventh overtone after injection of egg PC:egg PG liposomes with various lipid ratios at 37°C on a SiO_2 sensor. A) 0.8 µM egg PC and egg PG ratio 4:1. B) 0.8 µM egg PC and egg PG ratio 1:1. C) 0.8 µM egg PC and egg PG ratio 1:4.

Egg PC and egg PG were not suitable for successful integrin reconstitution as indicated by our results, where no integrin could be shown after reconstitution (data not shown), and by another protocol e.g. from Erb and Engel (Erb and Engel 2000). Therefore, other lipids were selected. DMPG and DMPC liposomes show comparative bilayer formation behavior as egg PC and egg PG (Figure 17). Only DMPC or a high ratio of DMPC:DMPG display typical vesicle rupture and bilayer formation, where its baseline levels out at values of Δf with -25 Hz and ΔD with 0.5 x 10^{-6} (Figure 17A and Figure 17B). A balanced ratio of DMPC:DMPG from 1:1 leads to low adsorption of liposomes, reaching a baseline at Δf of -10 Hz and ΔD of 1 x 10^{-6}, whereas smaller amounts as well as total absence of DMPC (Figure 17D and Figure 17E) reach comparable Δf values, but changes in dissipation up to 15 x 10^{-6}. Finally, the DMPC:DMPG ratio 20:1 was chosen for integrin αIIbβ3 reconstitution into liposomes.

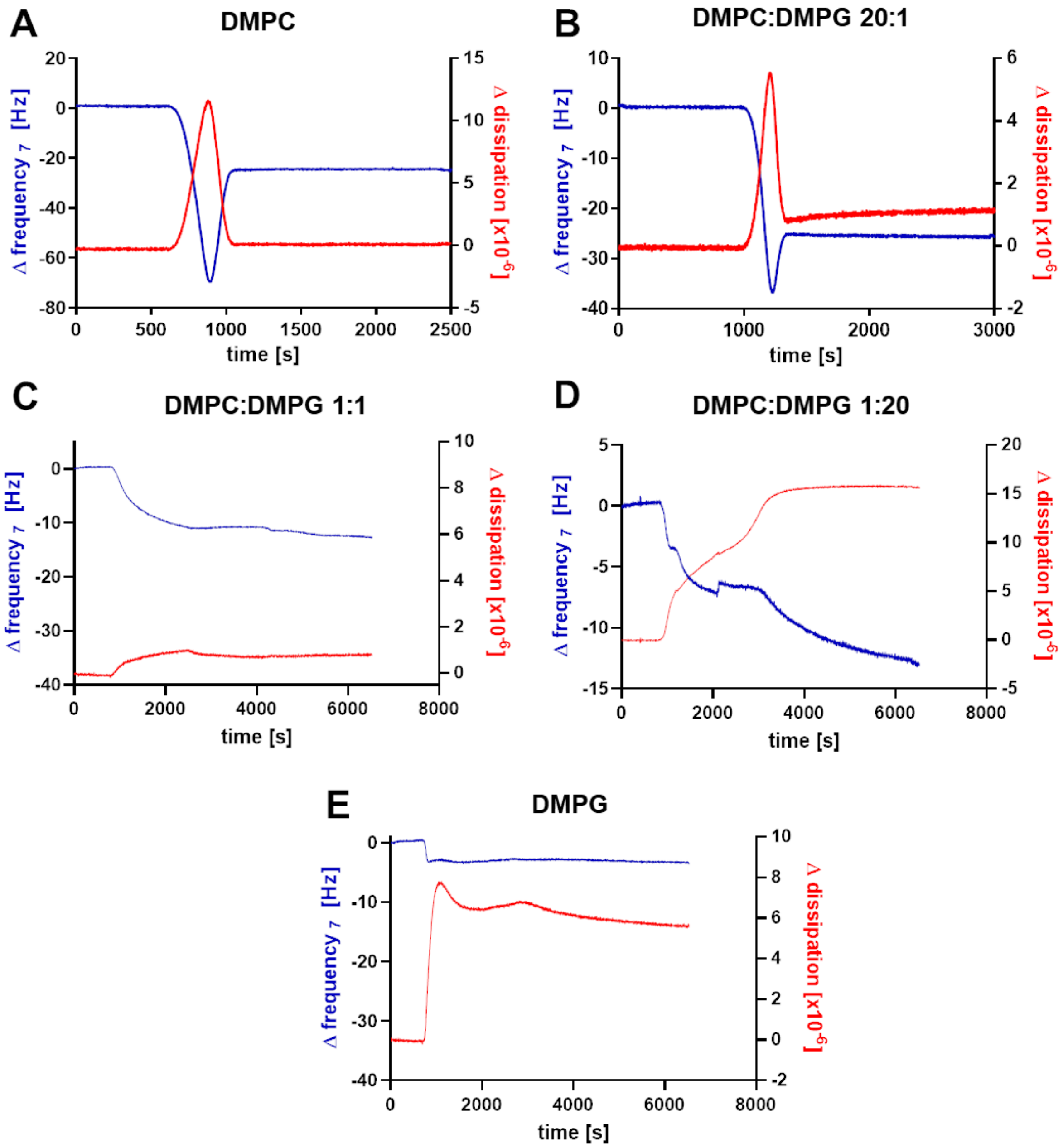

Figure 17: Representative QCM-D data showing the changes in frequency *f* (blue) and dissipation *D* (red) of the seventh overtone after injection of DMPC:DMPG liposomes with various lipid ratios at 37°C on a SiO_2 sensor. A) 0.8 µM DMPC. B) 0.8 µM DMPC:DMPG ratio 20:1 C) 0.8 µM DMPC:DMPG ratio 1:1. D) 0.8 µM DMPC:DMPG ratio 1:20. E) 0.8 µM DMPG.

4.1.3. Reconstitution of integrin into liposomes

Various techniques were used for validation of successful integrin reconstitution into liposomes. Figure 18A shows the hydrodynamic diameter of integrin-containing liposomes, namely proteoliposomes, as well as liposomes measured by DLS. The diameter of proteoliposomes (255 ± 16.6 nm) was substantially larger than that of liposomes (161 ± 1.3 nm). The presence of the two integrin subunits was verified by flow cytometry of fluorescently labeled PE CF proteoliposomes (Figure 18B). Over 80 % CD41 (αIIb-subunit) and CD61 (β3-sununit) positive events were detected, whereas bare liposomes showed no staining by anti-CD41 or anti-CD61 antibodies. TEM images of DMPG:DMPC vesicles in Figure 18C show the globular proteoliposomes with the integrin ectodomain showing a clearly distinguishable spherical head and a stalk domain at the rim of the membrane, which is indicated by a black arrow. Moreover, a reducing SDS-PAGE shows two visible bands in the proteoliposomes sample, corresponding to the two integrin subunits and no migrating protein bands for bare liposomes (Figure 18D).

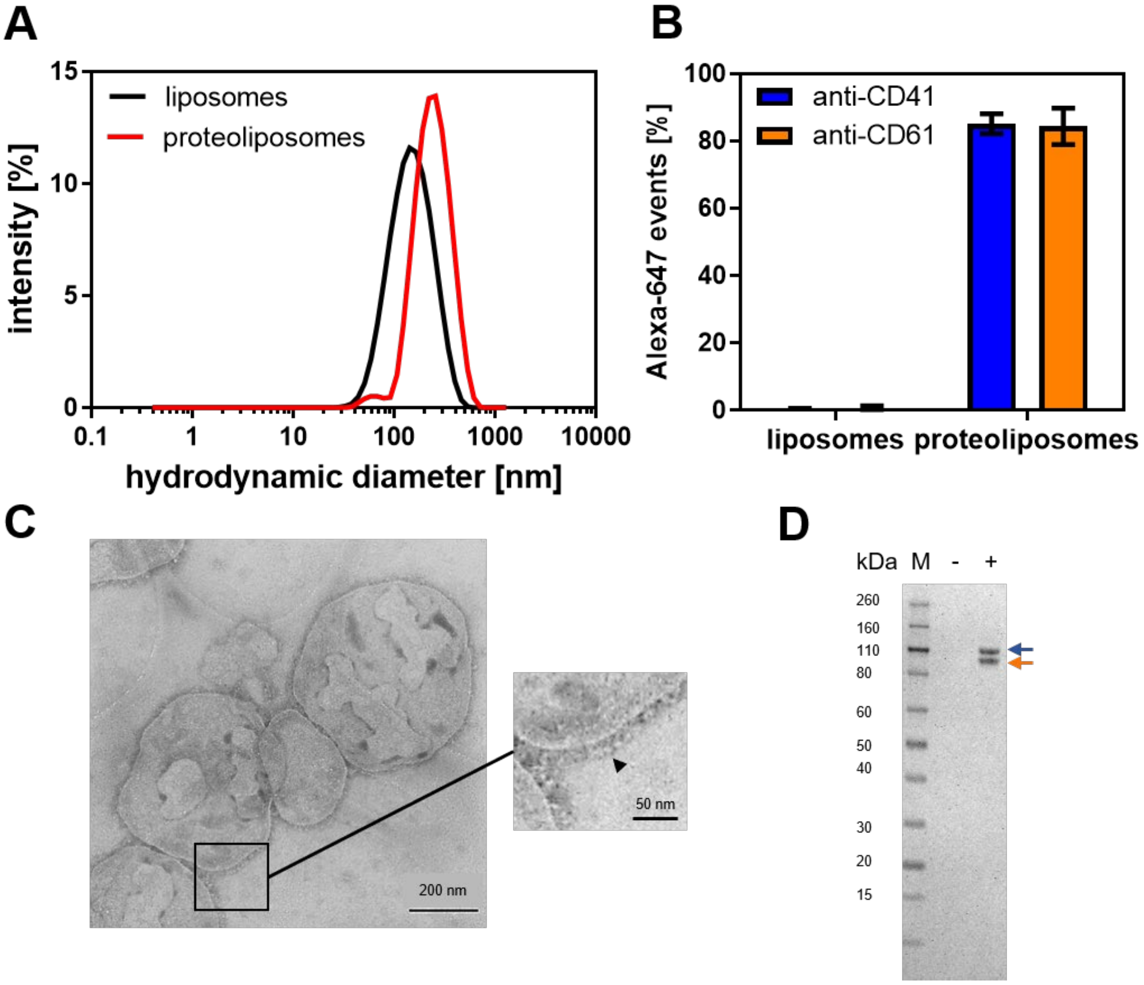

Figure 18: Validation of αIIbβ3 reconstitution into liposomes. A) DLS data showing the hydrodynamic diameter of liposomes (black) and proteoliposomes (red) of three replicate experiments measured in liposome buffer at 37 °C. B) FACS-plots with liposomes and proteoliposomes from three independent measurements. Percentages of the mean ± standard error of the mean (SEM) of anti-CD41 (blue) and anti-CD61 binding (orange) on PE CF- liposomes were statistically analyzed. C) TEM images of proteoliposomes. The inset presents a close-up view of integrin αIIbβ3 (indicated by arrow) reconstituted in a membrane. D) Reductive Tris-Glycine SDS-PAGE showing liposomes (-) and proteoliposomes (+) and protein molecular weight standard (M). The bands corresponding to the αIIb-(blue) and β3-subunit (orange) are specified by arrows. Adapted from (Janke et al. 2019).

4.1.4. Proteoliposome-derived bilayer formation

Contrary to blank liposomes, as it was depicted in Figure 17C, the injection of the proteoliposomes lead to a strong increase in the dissipation (12 x 10^{-6}), but only slightly higher changes in frequency (-50 Hz), which is displayed in Figure 19 as a representative experimental QCM-D profile. However, the increase in *D* is not as high as it would be predicted for a vesicle layer with such large liposomes (Richter et al. 2006), which indicates a SLB with higher dissipation due to the huge ectodomain of the integrin and remaining liposomes on the bilayer.

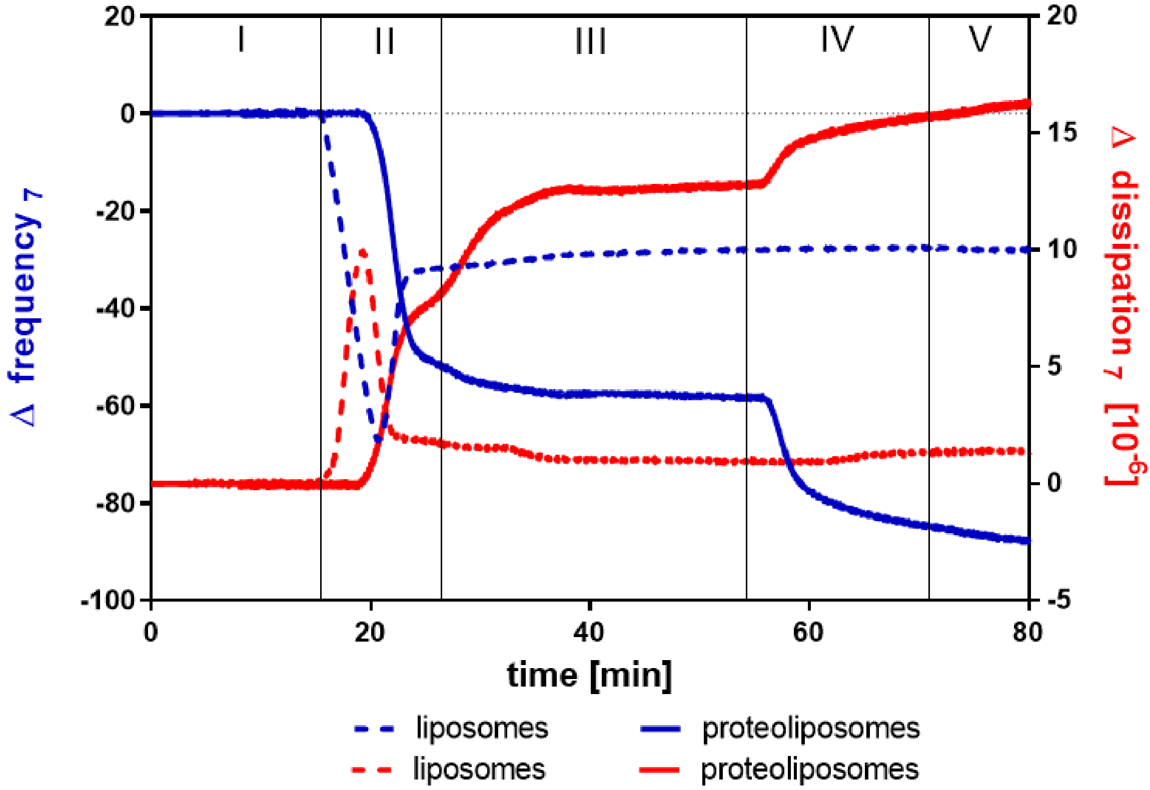

Figure 19: Representative QCM-D experimental profile of changes in dissipation (D-red) and frequency f (blue) of the seventh overtone at 37 °C. Respective buffer was injected over the SiO_2 surface (phase I). After reaching a baseline, liposomes (dashed line) or proteoliposomes (solid line) were added and the formation of a bilayer is presented (phase II). After washing with the respective buffer e.g. containing 1 mM Mn^{2+} (phase III), ligands (drugs, antibodies or nanoparticles) were injected (phase IV). Rinsing with buffer followed (phase V). Adapted from (Martens et al. 2019).

A specific procedure was applied for the QCM-D experiments for integrin activation (Figure 19). After reaching a baseline (phase I), liposomes or proteoliposomes formed a SLB (phase II) and were then washed with the respective buffer. Different treatments are run over the surface, e.g. divalent ions or drugs (phase III), followed by injection of antibodies and different ligands (phase IV). The equilibrium shift in *f* and *D* between time of injection in phase IV (Δf_7 *inject*; ΔD_7 *inject*) and the time of rinsing in phase V (Δf_7 *rinse*; ΔD_7 *rinse*) was calculated and correspond to the adsorbed mass(Δm). Eventually, the obtained values are indicators for interaction and binding to the bare SLB or SLB containing integrin.

To confirm the homogenous formation of SLB or integrin-containing SLB, AFM measurements of the QCM crystal surface were carried out, as depicted in Figure 20. Tapping mode images were taken of a liposome- or proteoliposome derived bilayer fused on a SiO_2 QCM crystal. Contact mode was then applied to the bilayer *via* AFM tip-scratch technique and the height profile was measured again by tapping mode, subsequently. Figure 20A and Figure 20B show the liposome-derived bilayer before and after scratching, respectively, as well as corresponding height profiles. Before scratching, the surface is homogenously covered and saturated, no blank substrate is visible, which would be indicated by dark color. The corresponding height profile fluctuates between -2 and + 2 nm representing a height of the covering of approximately 4 nm.

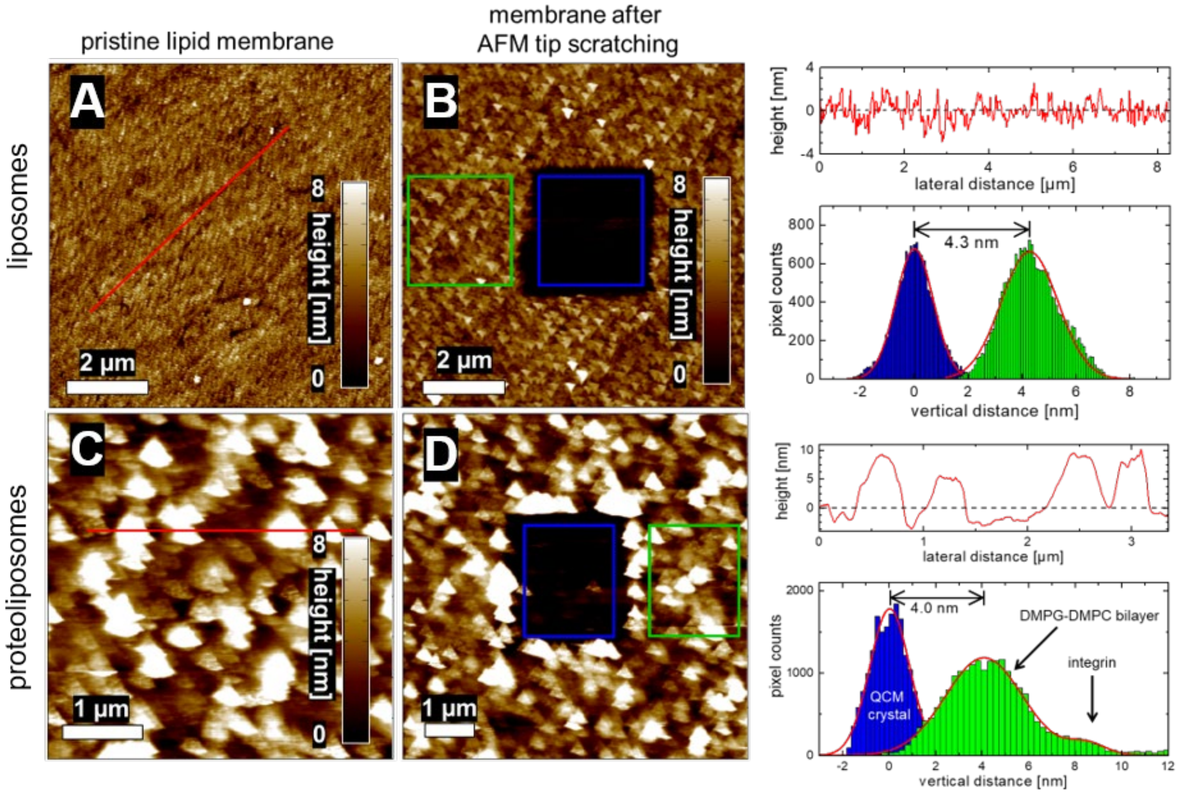

Figure 20: Tapping mode AFM image of DMPG:DMPC bilayers with and without integrin αIIbβ3. A) Image of a QCM SiO_2 crystal in buffer solution after collapse of liposomes. Height profile of bilayer before AFM tip-scratching is depicted in the upper right panel. Section line corresponds to the red line in A. B) Tapping mode AFM image of the same sample area after applying AFM tip-scratch technique as described in Chapter 3.6.5. The color-coded height bar ranges 8 nm. Histograms of height distribution after AFM tip-scratching is displayed right next to the picture. Height distributions are extracted either from region with exposed QCM crystal (blue) or intact bilayer (green), corresponding to blue and green rectangles in B, respectively. Histograms are fitted using Gaussian distribution for QCM crystal and DMPG-DMPC bilayer (red lines) revealing an average bilayer thickness of 4.3 nm. C) Corresponding tapping mode AFM image of DMPG:DMPC bilayer containing integrin αIIbβ. Same setup as described in A. D) Tapping mode AFM image of the same sample area after applying AFM tip-scratch technique. Same setup as described in B.

After scratching, followed by imaging in tapping mode of a larger area, a dark colored part appeared showing the blank substrate at the scratched area. Additionally, small triangular patterns are getting visible across the homogenous layer on the substrate.

The corresponding histogram height distribution, comparing the height of the scratched area and the bilayer region, confirms a height distance of 4.3 nm. Figure 20C and Figure 20D display the same setup but with a proteoliposome-derived bilayer, expecting an integrin-containing bilayer. The sample covered the surface homogenously and bigger clusters are visible with a height of approximately 8 nm, becoming broader and rectangular after scratching and imaging.

After scratching, histogram height distribution shows a difference in height peaks between QCM crystal surface and bilayer of 4 nm. However, a second height profile peak appears at 8-10 nm.

Diluted liposome samples (1:5 in liposome buffer) show bigger structures after tapping mode imaging, with a height profile up to 60 nm, which is displayed in Figure 21A. Figure 21B depicts a pure integrin sample air dried on a mica sheet, which exhibits a spherical head domain and two stalk domains with a lateral length of approximately 30 nm.

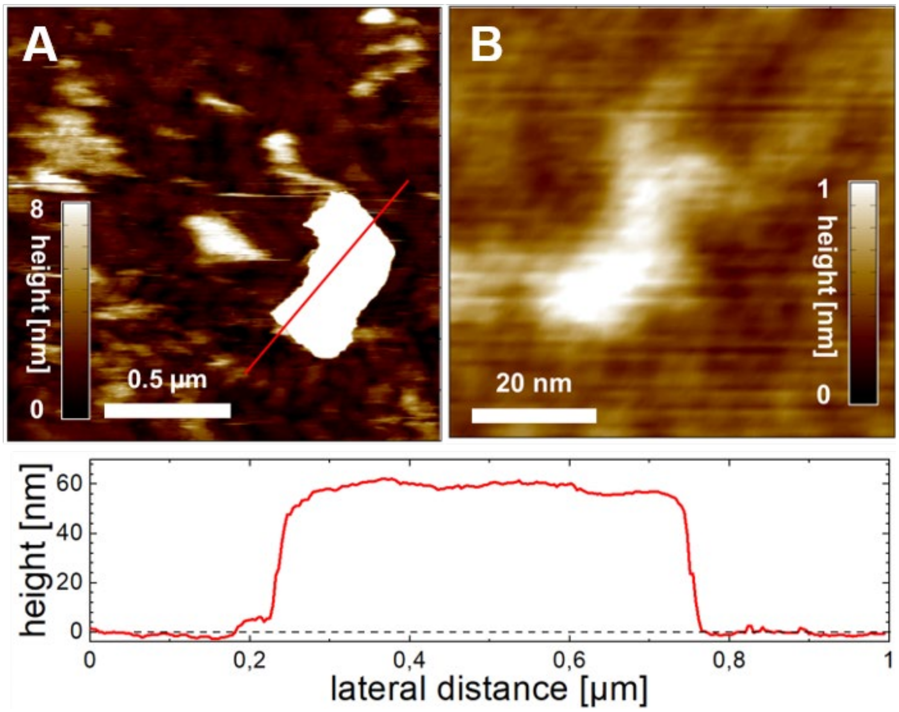

Figure 21: Tapping mode AFM image of a DMPG-DMPC liposome containing αIIbβ. A) Proteoliposomes were diluted 1:5 in liposome buffer (0.16 µM lipids). Image is taken in buffer solution after adsorption of proteoliposomes on mica. Scanned area is 2 µm x 2 µm and the color-coded height bar ranges 8 nm. The corresponding height profile of the DMPG-DMPC proteoliposome along the section line layer (red line) is depicted at the bottom. B) Tapping mode AFM image of a single αIIbβ3 integrin deposited on mica. Depicted area measures 75 nm x 75 nm and the color-coded height bar ranges 1 nm. Image is taken in air after sample drying.

4.1.5. Conformational changes of integrin upon treatment with manganese

This thesis addresses further the activation state of integrin αIIbβ3 reconstituted in liposomes by an activation assay with the conformation-specific antibody PAC-1. Figure 22 shows a schematic illustration of two experimental setups: QCM-D (A) and activation assay (B). In QCM-D, vesicles rupture on the sensor surface can be observed and PAC-1 binding to activated integrin is measured. As confirming experiment, activation assays were carried out, whereby PAC-1 antibody was immobilized on a microtiter plate and PE CF-labeled liposome binding was detected. Additionally, PE CF-labeled liposomes were incubated with fluorescently labeled PAC-1 antibody and binding was detected in a flow cytometer (not illustrated).

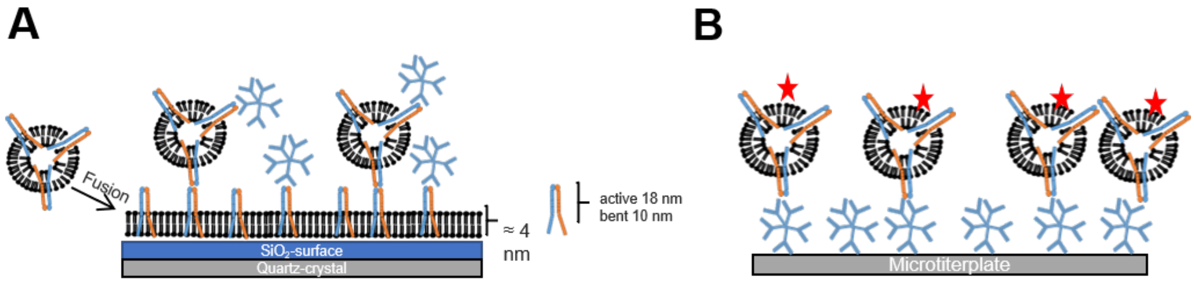

Figure 22: Integrin activation detection setup. A) Schematic illustration (not in scale) of the formation of a proteoliposome-derived bilayer with reconstituted integrin αIIbβ3 on a SiO_2 quartz sensor. We predict in our QCM-D experiments the fusion of proteoliposomes to the sensor surface to form a bilayer. Possibly, some proteoliposomes remain on the lipid bilayer. B) Schematic illustration (not in scale) for the setup of the activation assay. PAC-1 antibody is coated on a microtiter plate and differently treated PE CF-proteoliposomes bind to the antibody. Fluorescence (indicated by red stars) is then measured and evaluated. Adapted from (Janke et al. 2019).

The activation assay in Figure 23A shows substantially greater binding of PAC-1 to PE CF-labelled proteoliposomes after treatment with Mn^{2+} (red) in comparison to EDTA-treated proteoliposomes (blue). PAC-1 binding was increased without any additional ingredients (green), whereas flow cytometry measurements show only 2 % binding of PAC-1 to fluorescently-labelled proteoliposomes (Figure 23B). Mn^{2+}-treated liposomes show 25 % positive PAC-1 binding and no PAC-1 signal was observed in proteoliposomes incubated with EDTA for flow cytometry measurements.

Moreover, the complementary biophysical method QCM-D was used to address PAC-1 binding after formation of a SLB. The changes in f (top) and D (bottom) upon PAC-1 binding are depicted in Figure 23C. After the mentioned vesicle fusion, the SLB signal of bare liposomes (black) equilibrates at Δf at -26 ± 0.2 Hz and ΔD response of the opposite direction at 0.5 ± 0.1 x 10^{-6}. Proteoliposomes-created SLB (green) stabilizes at -53 Hz and rises in ΔD up to 12 x 10^{-6}. Upon rinsing in phase III with buffer containing 1 mM Mn^{2+} (red) Δf decreases approximately 5 Hz and ΔD increases 2.5 x 10^{-6}, and EDTA-treatment (blue) reaches changes of D up to 5 x 10^{-6}. For determination of integrin activation state, PAC-1 antibody was injected, subsequently (phase IV). Integrin-containing bilayer treated with Mn^{2+} (red) showed a reduction in Δf of 4 ± 0.3 Hz, while regular buffer treatment induces only 1.9 ± 0.7 Hz. Incubation of integrin-containing bilayer with EDTA led to even lower changes in f. Corresponding response in ΔD increases conversely. Control measurements without protein (pink, light blue, black) show neither changes in f, nor in D in phase IV.

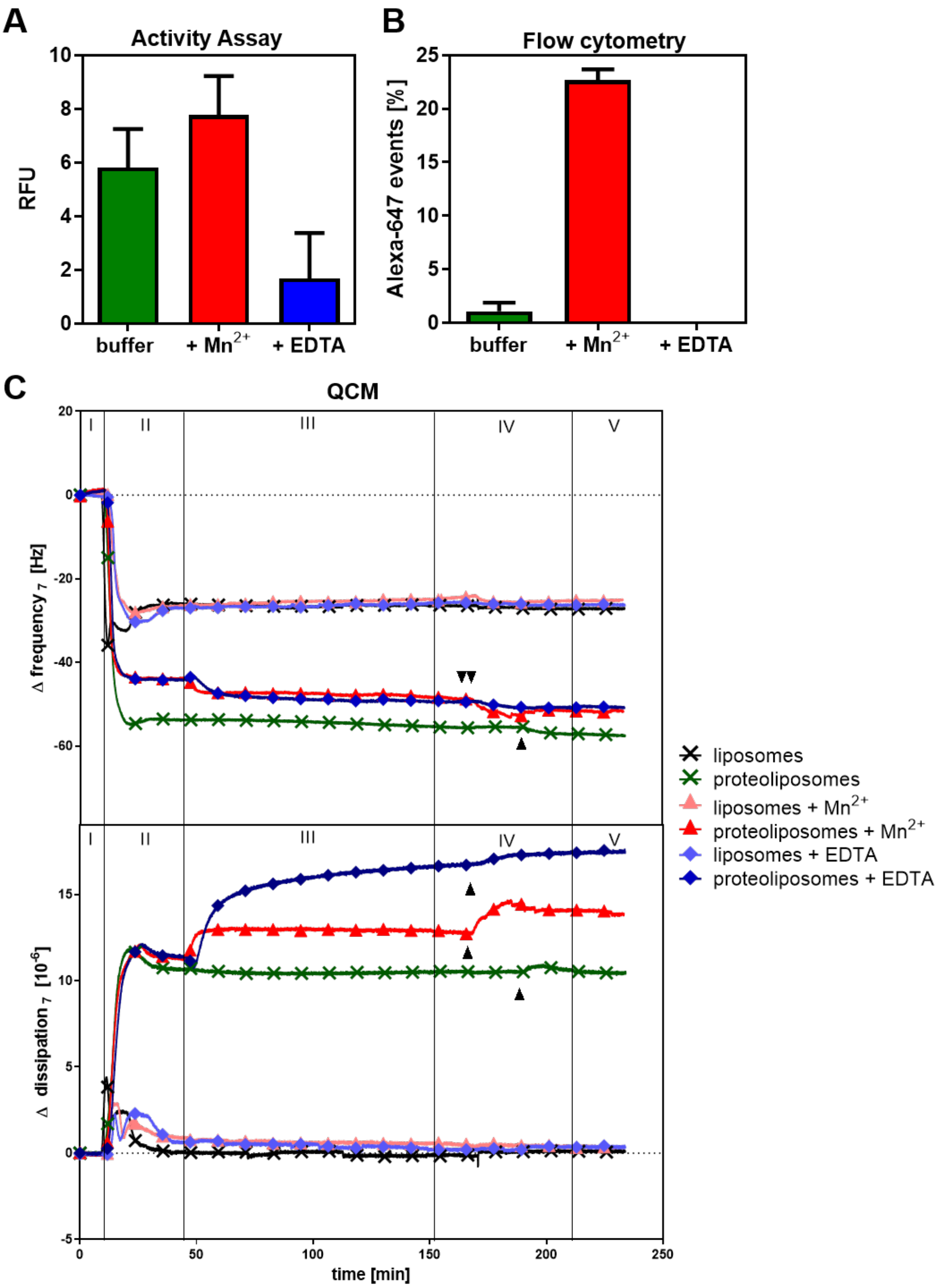

Figure 23: Activation of integrin αIIbβ3. A) Activation assay with PAC-1 antibody. Each value is the mean of three independent measurements ± SEM. Binding of PE CF-(proteo)liposomes to 5 µg/mL PAC-1 coated on a microtiter plate was analyzed after incubation with buffer (green), 1 mM Mn^{2+} (red) and 5 mM EDTA (blue). Signal of bare liposome samples were subtracted from proteoliposome results. Relative fluorescence units (RFU) specify PE CF fluorescence. B) Integrin activation was investigated by flow cytometry with PE CF-labelled liposomes subtracted from proteoliposomes signal. PAC-1-Alexa 647-coupled antibody was added and percentages of the mean ± SEM of Alexa-647 signal of PE positive events treated with buffer (green), Mn^{2+} (red) and EDTA (blue) are shown. C) Representative QCM-D data displaying the changes in frequency f (top) and dissipation D (bottom) of the seventh overtone for the binding of PAC-1 antibody at 37 °C. Buffer was injected trough the SiO_2 sensors (phase I) and after achieving a baseline (proteo)liposomes were injected. The formation of a bilayer is displayed (phase II). After washing with either liposome buffer, liposome buffer containing 1 mM Mn^{2+}, or 5 mM EDTA (phase III), PAC-1 antibody was inserted (phase IV) and binding was detected (indicated by arrows). Rinsing with the respective buffer followed (phase V). Adapted from (Janke et al. 2019).

4.1.6. Secondary structure changes upon manganese-induced integrin activation

To study potential changes in αIIbβ3 secondary structures and its correlation to the activation state of the protein, CD spectroscopy measurements were carried out. Figure 24A shows representative far-UV CD spectra of proteoliposomes (green), 1 mM Mn^{2+}-treated proteoliposomes (red) and after addition of 5 mM EDTA (blue).

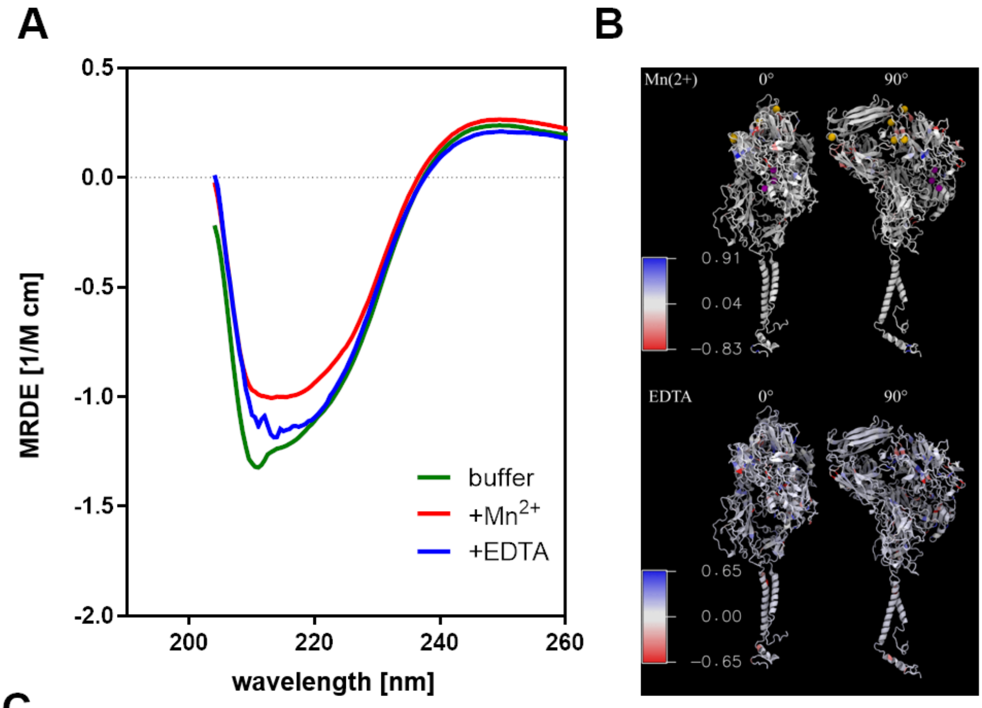

C

Structure content [%] \ Treatment	Buffer		Mn^{2+}		EDTA	
	experimental	*MDS*	*experimental*	*MDS*	*experimental*	*MDS*
Helix	9.0 ± 0.7	10.3 ± 1.1	8.4 ± 0.3	10.1 ± 0.9	8.9 ± 0.4	10.0 ± 1.1
Antiparallel beta-sheet	32.0 ± 1.3	21.9 ± 0.4	33.0 ± 0.6	22.3 ± 0.4	32.0 ± 0.7	22.6 ± 0.5
Parallel beta-sheet	5.5 ± 0	4.1 ± 0.2	5.5 ± 0	4.1 ± 0.2	5.5 ± 0	3.95 ± 0.2
Beta turn	19.5 ± 0.1	14.1 ± 0.7	19.5 ± 0	13.7 ± 0.7	19.4 ± 0.1	13.7 ± 0.9
Random coil	35.6 ± 0.1	49.8	35.5 ±0	49.8	35.5 ± 0.1	49.8

Figure 24: CD spectra and MDS of αIIbβ3 A) Far-UV region CD spectra of αIIbβ3 reconstituted into liposomes in buffer (green), with addition of 1 mM Mn^{2+} (red) or 5 mM EDTA (blue). Representative spectrum recorded with proteoliposomes (protein concentration of ~0.4 µM) or liposomes in 5 mm path length cuvettes at 37 °C is displayed. Liposome spectra were subtracted from the respective proteoliposome spectra. B) MDS representing the regions that changed in the antiparallel β-sheet probability after removal of all structural ions (bottom) or conversion of the three Ca^{2+} in the MIDAS, ADMIDAS and SyMBS to Mn^{2+} (top). The blue and red colored regions illustrate the loss or formation of β-sheets, respectively, compared to protein with Ca^{2+} and Mg^{2+} only. The β-sheet probability did not change in transparent/white regions. Mn^{2+} are colored in purple and Ca^{2+} ions in yellow C) Changes in the secondary structure distribution of integrin αIIbβ3 in buffer environment, after addition of 1 mM Mn^{2+} experimentally or converting the three ions in the MIDAS and ADMIDAS region to Mn^{2+} by MDS, and after addition of 5 mM EDTA experimentally or removal of all structural ions during MDS. The calculation of the experimental secondary structure content was carried out with the deconvolution of CD spectra using CDNN software. The MDS secondary structure was calculated with CPPTRAJ. Results correspond to three independent measurements ± SEM. Adapted from (Janke et al. 2019).

Bare liposome spectrum is subtracted from respective proteoliposome spectrum and an integrin far-UV spectrum arises, with one minimum at 210 nm. Mn^{2+} treatment leads to a decrease in amplitude, that can be nearly recovered due to EDTA addition.

Molecular dynamic simulations (MDS) studies were performed to confirm the obtained CD results. For this purpose, all divalent ions were either removed to mimic the experimental addition of EDTA or the corresponding divalent ions in MIDAS, ADMIDAS and SyMBS of the β3-subunit were altered to Mn^{2+}. Figure 24B illustrates the changes in β-sheet probability (red-less β-sheet, blue-higher β-sheet content). Without any divalent ions, various β-sheets destabilize at the PSI-domain, whereas new β-sheets are formed in the calf-1 as well as calf-2 domain and already present ones extend in the hybrid domain. Rearrangements occur also in the β-propeller of the α-subunit, which could be also observed after the exchange of the divalent ions in the metal ion-binding sides by Mn^{2+}. Additionally, elongation and formation of new β-sheets in the calf-1 and EGF2-domain arise. Changes in the secondary structure content for experimental and simulated methods are depicted in Figure 24C. Results of MDS studies support the CD results, whereby the α-helical content is decreasing with 0.6 % and β-sheet content rises by 1 % after adding Mn^{2+} in both methods.

4.1.7. Platelet integrin activation induced by clinical drugs

In addition to the treatment with ions, several drugs, that are known to interact with the integrin αIIbβ3 were tested. Changes in the secondary structure of integrin during the incubation with the anticoagulant drugs fondaparinux, unfractionated heparin (UFH) and quinine are displayed in Figure 25A where far UV spectra of liposome-subtracted proteoliposomes upon titration with rising concentrations of the respective drugs are shown. The extracted normalized CD signal as MRDE values at 210 nm wavelength are plotted in Figure 25B. The spectra show an increase in the amplitude with increasing concentration of UFH (Figure 25A) resulting in reduced MRDE values at 210 nm (blue, Figure 25B). Treatment of proteoliposomes with rising fondaparinux concentrations leads to insignificant changes of the MRDE signal (purple), which can be also observed with quinine at concentration between 0.1-1.5 µg/mL (black). A linear dependency of the MRDE at 210 nm on the logarithm of the drug concentrations, especially for UFH, can be described within the experimental error, which indicates integrin secondary structural changes upon UFH treatment.

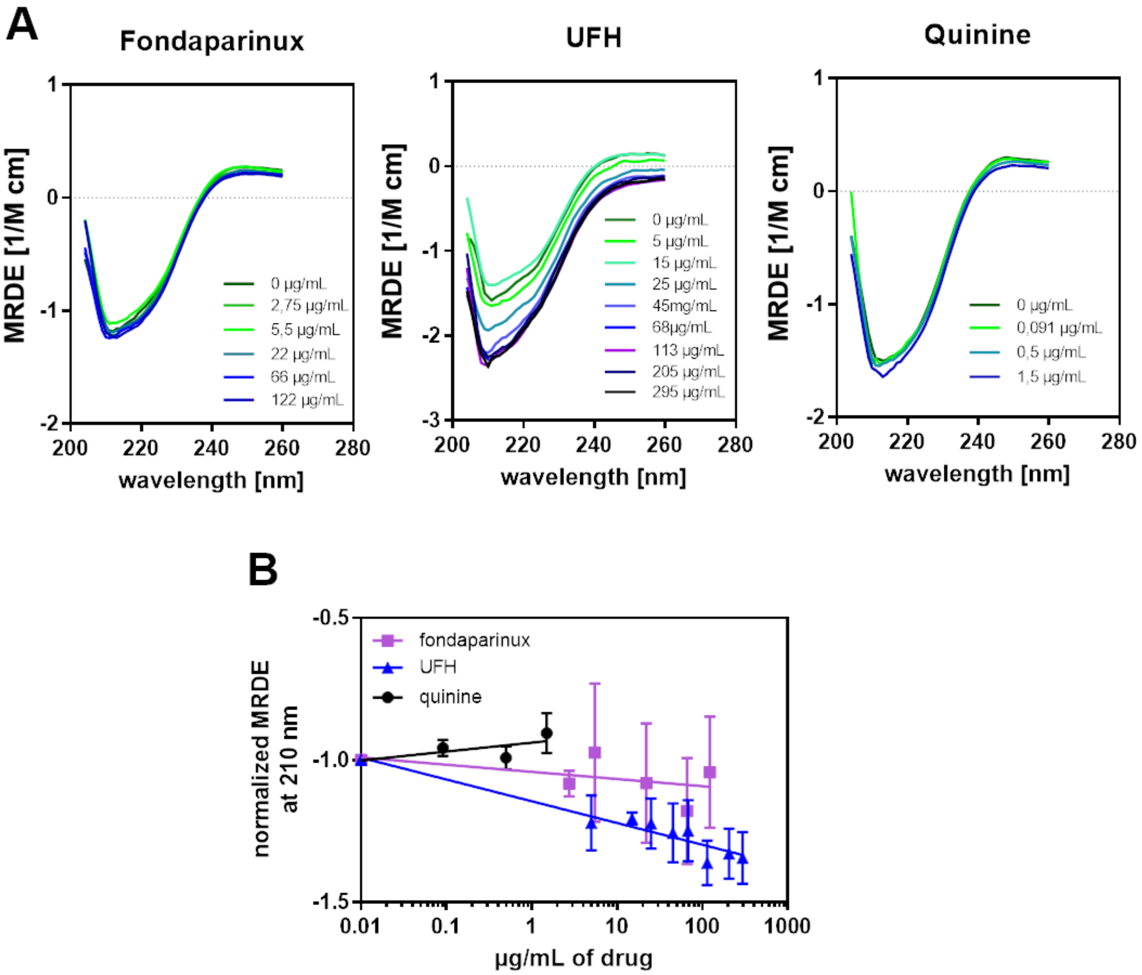

Figure 25: Integrin αIIbβ3 secondary structure after treatment with drugs. A) The far-UV region CD spectra of αIIbβ3 reconstituted into liposomes in buffer (dark green), and with increasing concentrations of fondaparinux (left), UFH (middle) and quinine (right), respectively. Representative spectra verified for proteoliposomes (protein concentration ~0.4 µM) in 5 mm path length cuvettes at 37 °C are presented. Liposome spectra were subtracted from the respective proteoliposome spectra. B) Normalized single wavelength plot for corresponding MRDE values at 210 nm from far-UV region CD spectra of αIIbβ3 reconstituted into liposomes incubated with rising concentrations of UFH (blue), fondaparinux (purple) and quinine (black), respectively. Normalized means from three independent measurements ± SEM are displayed as dots that were extracted from (A) Respective trendlines were applied to guide the reader. Adapted from (Janke et al. 2019).

QCM-D results reveal activation state detection by PAC-1 antibody to integrin-containing SLB upon treatment with fondaparinux, UFH and quinine. Figure 26A shows the representative QCM-D graphs, starting with the liposome (pink) or proteoliposome (purple) injection followed by SLB formation and treatment with the drugs, respectively. Untreated SLB and integrin-containing SLB are highlighted in grey and black, respectively. Changes in *f* (blue) and *D* (red) during PAC-1 injection indicate binding to the bilayer embedded activated αIIbβ3 and are extracted (as Δ*f* and Δ*D*) in Figure 26B. The shift in *f* and *D* for quinine (4.3 Hz; 1.1 x 10^{-6}) and Mn^{2+} (4.0 Hz; 1.4 x 10^{-6})-treated integrin containing bilayer are similar and higher than in the absence of drug or Mn^{2+} (buffer, 1.9 Hz; 0.5 x 10^{-6}).

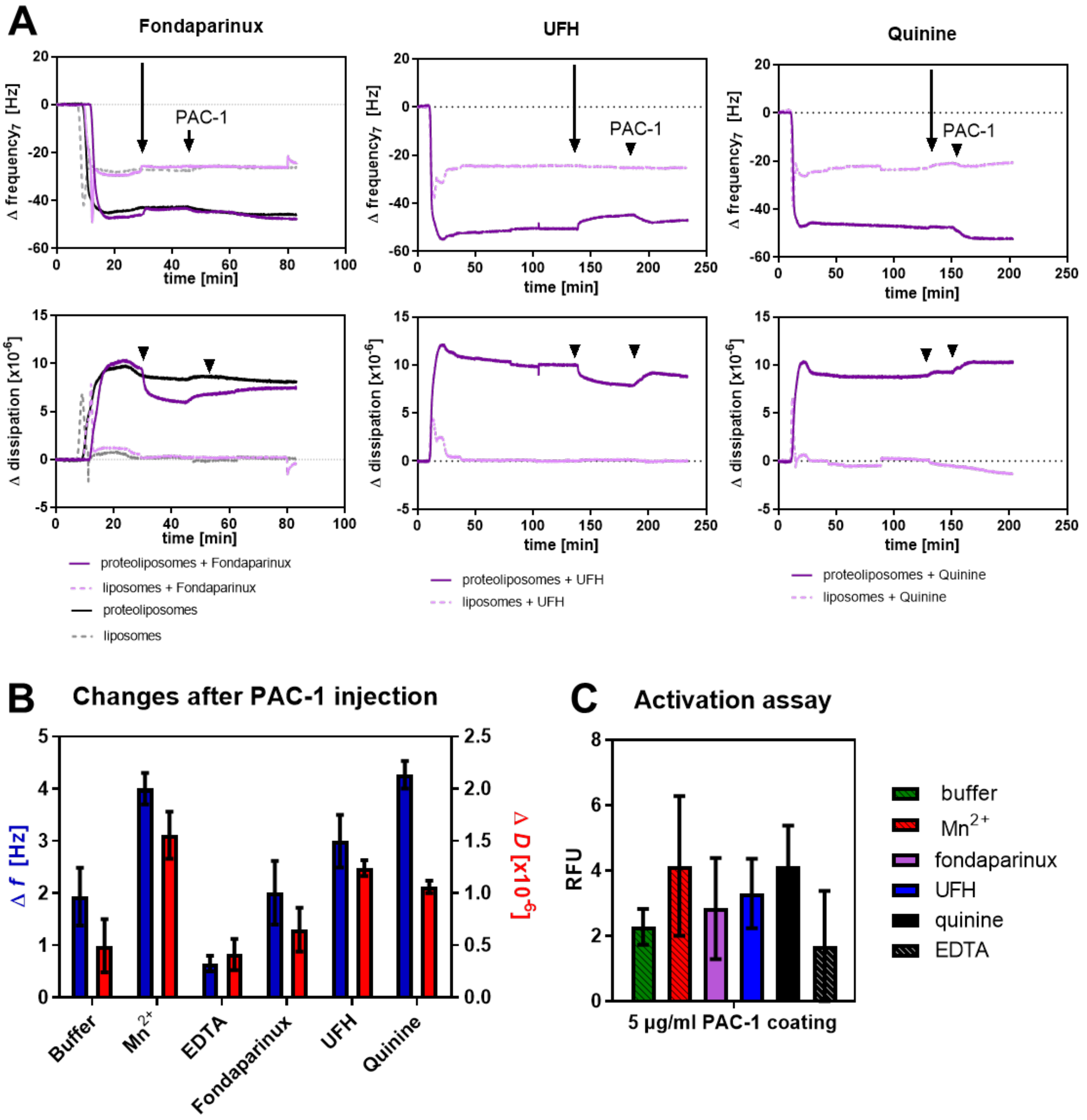

Figure 26: Integrin αIIbβ3 activation by drug treatment. A) Changes in frequency Δf (top) and dissipation ΔD (bottom) of the seventh overtone after drug treatment of liposome (pink)- and proteoliposome-derived bilayer (purple) at 37 °C. The bilayer was treated with the respective drugs (250 µg/mL fondaparinux, 250 µg/mL UFH and 50 µg/mL quinine sulfate), which is indicated by the first arrow and PAC-1 antibody was added (second arrow) followed by rinsing with liposome buffer. Buffer control treatments of liposome (grey)- and proteoliposome-derived bilayer (black) are displayed in the graph with fondaprinux B) Changes in Δf (blue) and ΔD (red) upon injection of PAC-1 were subtracted from values after rinsing. PAC-1 injection event is indicated by the respective arrows in the representative QCM graphs in (A) with proteoliposomes after treatment with buffer, 1 mM Mn^{2+}, 250 µg/mL fondaparinux, 50 µg/mL quinine, 250 µg/mL UFH and 5 mM EDTA for at least 15 min at 37°C. Results correspond to three independent measurements ± SEM C) Drug activation assay with PAC-1 antibody. Each value is the mean of three independent measurements ± SEM. PE CF-liposomes/proteoliposomes bind to 5 µg/mL PAC-1 coated to a microtiter plate. Binding was detected after the incubation with buffer (dashed, green), 1 mM Mn^{2+} (dashed, red), 5mM EDTA (dashed, blue), 250 µg/mL fondaparinux (purple), 250 µg/mL UFH (blue) and 50 µg/mL quinine (black). Liposome sample values were subtracted from proteoliposomes values. The y-axis presents relative fluorescence units (RFU). Adapted from (Janke et al. 2019).

UFH (3.0 Hz; 1.2 x 10^{-6}) and fondaparinux (2.0 Hz; 0.7 x 10^{-6}) show similar PAC-1 binding compared to buffer control. Additionally, only half of the buffer signal is found upon addition of EDTA. Furthermore, the activation assay with PAC-1 coated on a microtiter plate confirm the

QCM data (Figure 26C). After incubation with quinine (black) or Mn^{2+}(dashed, red), the highest binding tendency of PE CF-labelled proteoliposomes to PAC-1 could be detected in comparison to the buffer control (dashed, green). UFH-treated proteoliposomes (blue) display higher fluorescence signal than fondaparinux (purple) as well as the buffer control, where the latter are on the same level. Again, EDTA treatment shows the lowest binding activity of PAC-1 to proteoliposomes (dashed, blue).

4.1.8. Interaction of integrin αIIbβ3 with fibrinogen bioconjugates

An upcoming trend in biomedical research and diagnostics is the treatment with nanoparticles, whose spectrum of application reaches from imaging to targeted drug delivery. All scenarios involve blood contact, which includes high abundant proteins, e.g. the integrin αIIbβ3 ligand fibrinogen and blood cells, e.g. platelets. Therefore, the already presented biophysical setup for manipulation of activation state of integrin is applied to study the binding of differently coated fibrinogen-bioconjugated nanoparticles to integrin-containing membranes.

First, size and charge of differently coated Fe_2O_3 nanoparticles are characterized and are presented in Figure 27A and Figure 27B, respectively. Before the incubation with fibrinogen (Fb), citrate-stabilized particles (yellow) reveal a hydrodynamic diameter of 35 nm, while dextran (blue)- and polyethylene glycol (PEG, red)-coating leads to sizes of 38 nm and 42 nm, respectively (Figure 27A). After 1 h incubation of nanoparticles with Fb (dashed bars), the hydrodynamic diameter rises up to 75 nm for citrated and 100 nm for dextran modified nanoparticles. However, PEGylated nanoparticles stay at 42 nm after 1 h incubation with Fb. Moreover, zeta potential of nanoparticles was measured before and after incubation with Fb for 3 h (Figure 27B). Bioconjugate formation results in a change of the zeta potential from -38 mV to -2 mV for citrated and -37 mV to -7 mV for dextran nanoparticle, but for PEG-nanoparticles only 2 mV changes resulting in a value of -4 mV.

Finally, the behavior of citrated-, dextran- and PEGylated nanoparticles in the presence and in the absence of fibrinogen upon interaction with lipid bilayers containing integrin was analyzed (Figure 27C). A SLB out of blank liposomes or proteoliposomes was formed on a SiO_2 sensor surface by vesicle fusion technique followed by injection of different types of unconjugated or Fb-conjugated nanoparticles. The QCM-D graphs depict the equilibrium shift of f and D between NPs injection and rinsing measured in experimental phase IV (Figure 19). The acquired data corresponds to the adsorbed mass of nanoparticles during the injection period. Introduction of the SLB to a solution of unconjugated nanoparticles leads to insignificant changes in in f and D, where dextran and PEG nanoparticles reach minor changes of $\Delta f = 3$ Hz and in $\Delta D = 1 \times 10^{-6}$. Additionally, also Fb alone and Fb-conjugated nanoparticles show no changes in neither f or D. However, for integrin-containing SLB f changes to 33 Hz and D to 6×10^{-6} upon injection of unconjugated citrated- as well as dextran- coated nanoparticles. PEG coating shows tenfold less values (3 Hz in *f* and 0.5 x·10^{-6} in *D*). Conjugation of PEG nanoparticles to Fb does not change significantly these results. However, Fb-conjugated citrate and dextran nanoparticles show significant less adsorption to integrin-containing SLB (~5 Hz in *f* and 0.5·10^{-6} in *D*) compared to unconjugated nanoparticles.

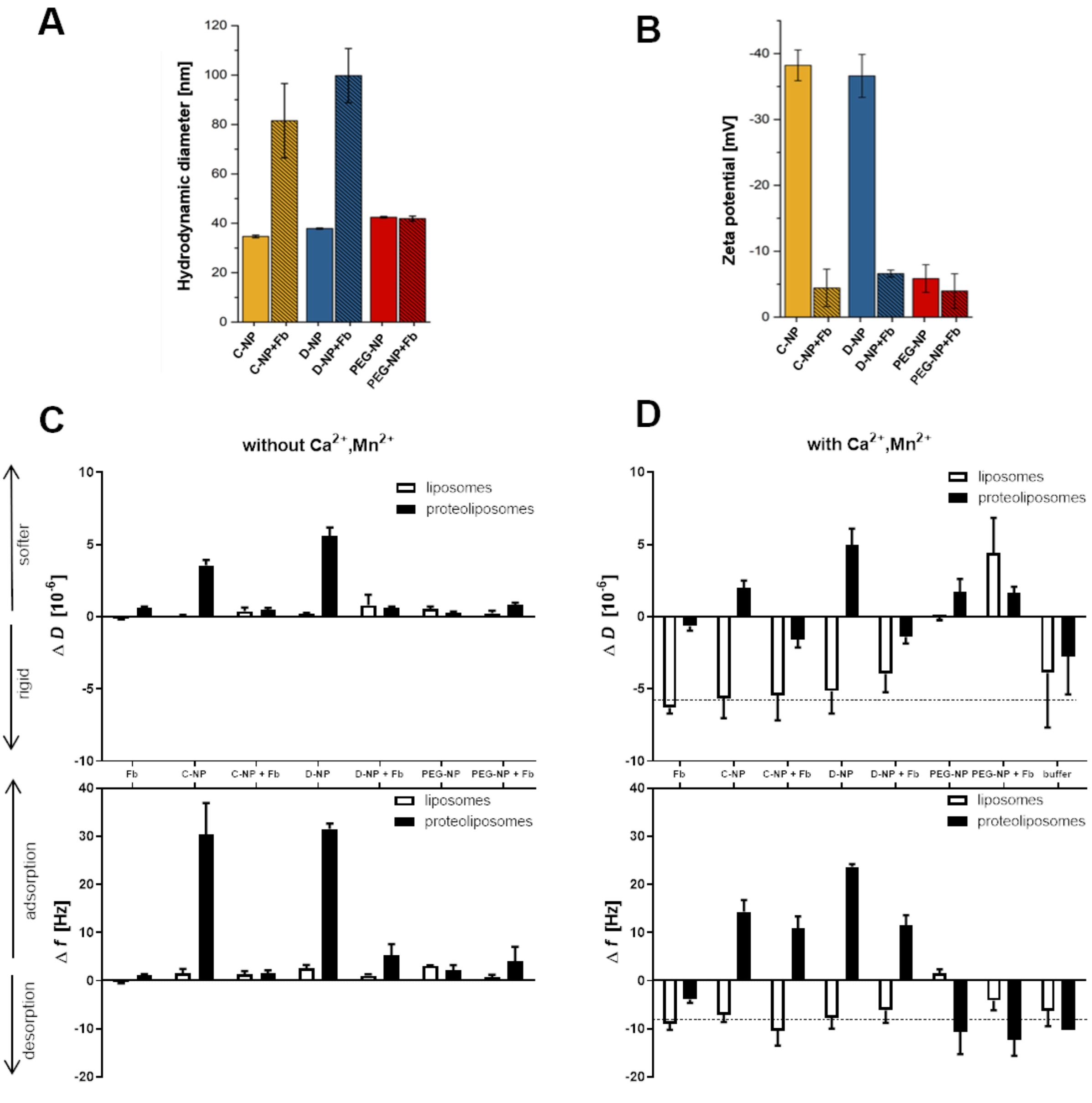

Figure 27: Fibrinogen-coated nanoparticle binding to artificial platelet membrane. A) Hydrodynamic diameter (intensity weighted distribution) and B) Zeta potential of citrate- (C-NP-yellow), dextran- (D-NP-blue) and PEG-functionalized (PEG-NP-red) maghemite nanoparticles and their bioconjugates with fibrinogen (dashed) in PBS. Results correspond to three independent measurements ± SEM C) Changes in dissipation (top) and frequency (bottom) during injection of fibrinogen (Fb), bare NP (C-citrate, D-dextran, PEG-NP) and fibrinogen-coated NPs (+Fb) received from QCM-D experiments during experimental phase IV (Figure 19). NPs and bioconjugates were added to SLB without (white) or with incorporated integrin (black). The running buffer was PBS without any divalent ions. D) Changes in dissipation (top) and frequency (bottom) during injection of fibrinogen (Fb), bare (C-citrate, D-dextran, PEG-NP) and fibrinogen-coated NPs (+Fb) after incubation with divalent ions (1 mM $CaCl_2$, $MgCl_2$, $MnCl_2$), received from QCM-D experiments during experimental phase IV. NPs and bioconjugates injected to SLB without (white) or with incorporated integrin (black). Adapted from (Martens et al. 2020).

Integrin conformation and binding behavior depend on several divalent ions, hence, SLBs were treated with Ca^{2+}, Mg^{2+} and Mn^{2+}, where the latter favors the active, ligand binding conformation of αIIbβ3. Figure 27D shows changes in *f* and *D* upon nanoparticle injection after treatment of the SLB and integrin-containing SLB with divalent ions. The first prominent variance is that only the buffer switch from divalent ion-supplemented PBS to PBS show already changes in *f* (10 Hz) and *D* (6×10^{-6}) for liposome as well as proteoliposome-derived SLB, but not for empty sensor surface (Figure S3). Due to stability of the nanoparticle conjugates, the particles are suspended in PBS without divalent ions. Consequently, the buffer switch leads to a mismatch that causes a shift in *f* and *D* upon NP injection, which is indicated by the dashed line in Figure 27D. For this reason, changes in that range have to be evaluated with care.

Injection of citrate-, dextran NPs and the respective bioconjugates to the proteoliposome-derived SLB results in high Δf (up to 25 Hz for dextran) and ΔD (6×10^{-6}), whereas no changes occur in the bare SLB sample. Fb conjugation leads to less than half of adsorption for citrate and dextran coated nanoparticles, but even more compared to no divalent ion treated integrin-membrane. By contrast, PEGylated blank and Fb-conjugated NPs show no changes in *f* after divalent ion treatment, whereas *D* increased for both SLB and integrin-containing SLB.

4.1.9. Influence of different lipidic systems on platelet integrin activation

In this chapter the effect of different lipidic systems on integrin receptor activation will be presented. For this purpose, a new reconstitution protocol for integrin αIIbβ3 into liposomes was established using lipids closer to the mammalian cell membrane, since conventional protocols use lipids with short fatty acid chains typically represented in bacterial cell membranes. For a better control of the environmental and purification conditions integrin αIIbβ3 was purified from outdated human platelets for liposome preparation with different lipids and detergents, subsequently.

After lysis of the platelets, integrin was purified following a protocol from Gingras et al. (Gingras et al. 2013). First, all glycoproteins, which includes also integrin αIIbβ3, were captured by a Concanavalin A column. The elution profile is depicted in Figure 28A and elution was induced by a buffer containing high concentrations of mannopyranoside sugar (Buffer B). Platelet lysate was loaded on the column and washed with at least 10 column volumes with CHAPS buffer, to remove Triton X-100, for the samples that should contain CHAPS. The column was then eluted, which gives peak up to 300 mAu going back to 0 until end of elution. The blue bar represents the fractions loaded onto the SDS-PAGE (Figure 28B). Both subunits are present at approximately 100 kDa and 130 kDa in the elution fractions with varying concentrations decreasing with the volume of elution buffer.

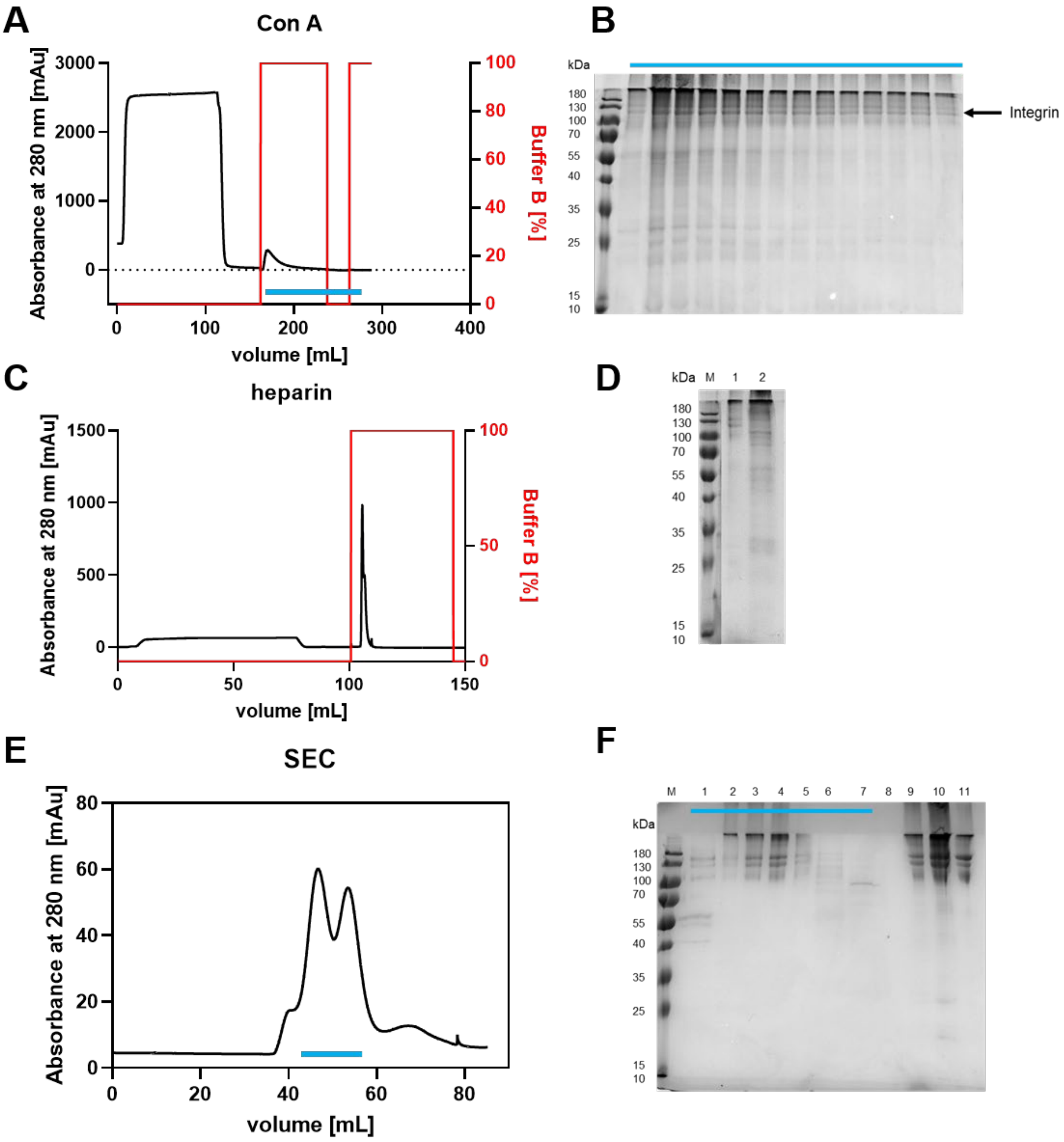

Figure 28: Purification of integrin αIIbβ3. A) Elution chromatogram of the ConA column (black) eluted with a flow rate of 1 mL/min and 100 % elution buffer (red), collected elution fractions are indicated in blue. Elution Buffer B was 20 mM HEPES, 150 mM NaCl, 1 mM $CaCl_2$, 1 mM $MgCl_2$, 1 % CHAPS, 5 µmol Leupeptin, 200 mM methyl *α*-D mannopyranoside. B) Reductive SDS-PAGE of ConA Elution factions and protein molecular weight standard (M) shown on the left. Elution fractions are indicated by a blue bar and integrin subunits are displayed by arrows. C) Chromatogram of heparin column (black) eluted with a flow rate of 1 mL/min and 100% elution buffer containing 20 mM Tris, 1M NaCl (red). D) Reductive SDS-PAGE of heparin column. Protein molecular weight marker (M), flow through (1) and elution fraction (2) E) Size exclusion chromatogram of concentrated heparin flow through with a flow rate of 0.5 mL/min, collected elution fractions are indicated in blue. F) Reductive SDS-PAGE of SEC elution factions and protein molecular weight standard (M) shown on the left, elution fractions (1-8) are indicated by a blue bar and concentrated Heparin FT is displayed (9-10). Integrin control is loaded in lane 11.

In a second step, eluted fractions were loaded on a heparin column to remove other components of the blood e.g. antithrombin III (Figure 28C), resulting in a band larger than 180 kDa and two bands between 100 and 130 kDa corresponding to integrin in the flow through of the heparin column (Figure 28D). The latter mentioned bands are not present in the elution peak fraction. The last step includes a size exclusion chromatography (SEC) to remove impurities e.g. fibrinogen or thrombospondin depicted in Figure 28E. The concentrated heparin flow through was loaded on the column and several peaks appear. The fractions were collected and analyzed in a reductive SDS-PAGE shown in Figure 28F. In the peak fractions, indicated by the blue bar, both subunits of the integrin can be detected at approximately 110 kDa and 130 kDa corresponding to the same size of the integrin control bands as well as the bands in the heparin flow through. The intensity of the bands corresponds to the height of the peaks.

This purified integrin was used further for liposome preparation following the reconstitution protocol with CHAPS, described in Chapter 3.3.2.

Different lipids and compositions were used to study its influence on the activation dynamics of integrin αIIbβ3. First, DMPC and DMPG lipids were exchanged to DOPC, SM and cholesterol in a ratio 37.5:37.5:25 and integrin was reconstituted with the already presented Triton X-100 protocol (Erb and Engel 2000).

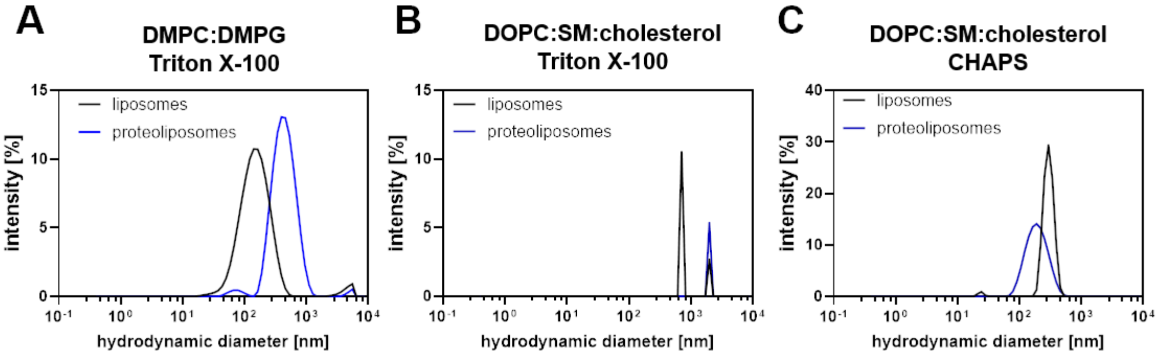

	Z-Average [d.nm]	PdI
liposomes	136,06	0,262
proteoliposomes	358,26	0,284

	Z-Average [d.nm]	PdI
liposomes	2312	0.684
proteoliposomes	1733	0.465

	Z-Average [d.nm]	PdI
liposomes	384.6	0.122
proteoliposomes	189.6	0.265

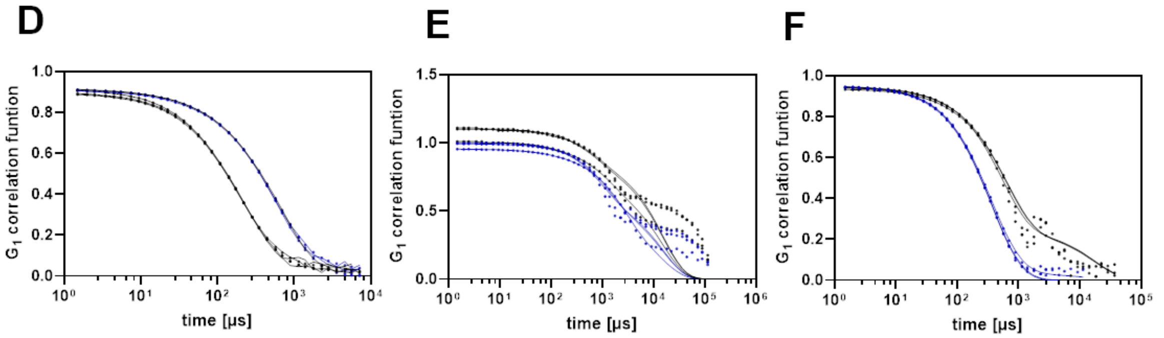

Figure 29: Characterization of integrin reconstitution into different lipid systems. A-C) DLS data showing hydrodynamic diameter of liposomes (black) and proteoliposomes (blue) of three independent measurements in respective buffer at 37°C. Liposomes are reconstituted with A) DMPG:DMPC lipids and Triton X-100 B) DOPC:SM:cholesterol and Triton X-100 and C) DOPC:SM:cholesterol and CHAPS. Corresponding Z-Average and polydispersive Index (PDI) are specified in the table under the graphs. D-F) Correlation function distribution fit (lines) of the corresponding DLS measurement (dots) for liposomes (black) and proteoliposomes (blue).

Figure 29 shows the hydrodynamic diameter of these liposomes (B) compared to the liposomes prepared with DMPG:DMPC (A). DMPG:DMPC liposomes display a hydrodynamic diameter of 136 nm for liposomes, 358 nm for proteoliposomes and a PDI around 0.27 (Figure 29A). Moreover, the corresponding correlation function distribution fit describes the data well (Figure 29D). However, same preparation method but different lipids (DOPC, SM and cholesterol) produce liposomes (2312 nm) and proteoliposomes (1733 nm) larger than 1500 nm (Figure 29B). Additionally, the PDI shows values upon 0.5 and a correlation distribution fit deviating from the measured data points (Figure 29E). Changing of the reconstitution protocol to a method based on excessive dialysis (Coskun et al. 2011) and the detergent CHAPS leads to liposomes with a hydrodynamic diameter of 384 nm and 189 nm for proteoliposomes which is depicted in Figure 29C. The PDI is under 0.3 and the fit of the correlation distribution function describes the measured data points (Figure 29F).

Additionally, reductive SDS-PAGE shows bands for all proteoliposome samples and control integrin at approximately 90 and 110 kDa (Figure 30) corresponding to the control integrin, that could be detected with highest intensity of bands for the Triton X-100 reconstitution protocol with DMPG and DMPC (Figure 30) as well as its modified version with DOPC, SM and cholesterol. Several ratios of DOPC, SM and cholesterol are applied, giving different rates of lipid-ordered and lipid-disordered phases [ratios taken from (Kaiser et al. 2009)].

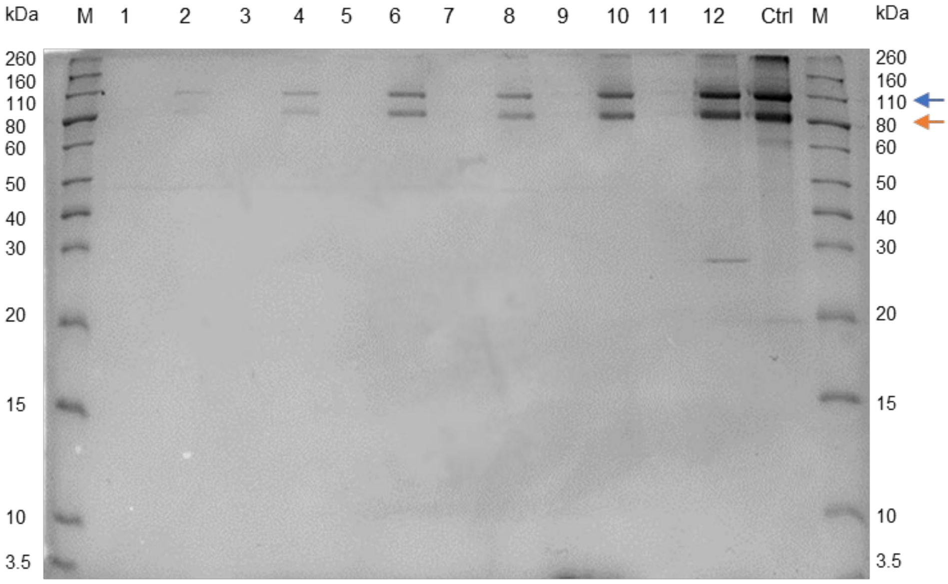

Figure 30: Reductive SDS PAGE of liposomes and proteoliposomes prepared with different lipids and lipid ratios. Reductive SDS-PAGE of protein molecular weight standard (M) and control of integrin αIIbβ3 (Ctrl). The bands corresponding to the αIIb- (blue) and β3-subunit (orange) are indicated by arrows. DOPC:SM:cholesterol proteoliposomes (even numbers) and liposomes (odd numbers) following the modified reconstitution protocol from Coskun et al. with ratios, 25:35:40 (1,2), 45:30:25 (3,4), 60:28:12 (5,6), 70:25:5 (7,8) are shown. Additionally, proteoliposomes and liposomes prepared using reconstitution procedure of Erb and Engel (Erb and Engel 2000) with Triton X-100 are shown. DOPC:SM:cholesterol in a ratio 37.5:37.5:25 (9,10) and DMPG:DMPC lipids with a ratio 1:20 (11,12) are displayed.

High amounts of cholesterol lead to less intense protein bands after reconstitution (DOPC:SM:cholesterol 25:35:40-lane 2), whereas high amounts of DOPC show more intense integrin bands (all other ratios DOPC:SM:cholesterol 37.5:37.5:25; 45:30:25; 60:28:12; 70:25:5- lane 3-10). The different lipid ratio derived (proteo-)liposome hydrodynamic diameters were measured in DLS (Table 6) and mostly, a heterogeneous size distribution was found, as indicated by high PDI values ranging from 0.363, for ratio with the maximum cholesterol concentration, to over 0.75 for high DOPC content. Size decreases upon arising DOPC content, whereas the ratio with highest cholesterol concentration are becoming larger up to sizes over 700 nm. In most samples a second peak (by intensity) appears, which is mostly under 100 nm. Bare liposomes are significantly larger compared to proteoliposomes, except for the ratio 70:25:5, where liposomes are smaller (275 nm) than proteoliposomes (337 nm). Lipid stability for every liposome ratio after reconstitution was detected in a thin layer chromatography (Figure S4).

Table 6: Hydrodynamic diameters of different DOPC:SM:cholesterol ratios after integrin reconstitution or blank liposomes. Data was collected using a Zetasizer Ultra.

DOPC:SM: cholesterol		**Peak one by intensity [d.nm]**	**Peak two by intensity [d.nm]**	**PDI**
25:35:40	liposomes	739.33	81.2	0.437
	proteoliposomes	652	111.5	0.363
45:30:25	liposomes	814.75	54.1	0.389
	proteoliposomes	580.33	68.1	0.495
60:28:12	liposomes	475.33	42.6	0.447
	proteoliposomes	320	457.8	0.441
70:25:05	liposomes	275	-	0.76
	proteoliposomes	337	41.4	0.75

The ratio with liposome sizes around 150 nm, intense protein bands in SDS-PAGE and a PDI under 0.7 was chosen for negative stain imaging in transmission electron microscopy (Figure 31). Additionally, these samples were compared to the Triton X-100 protocol derived (proteo)liposomes comprising of DOPC, SM and cholesterol. The proteoliposomes prepared with the CHAPS protocol show a spherical shape structure with size of 200 nm (Figure 31A and 31B). A close-up view allows the identification of elongated structures at the rim of the liposomes forming a head and thinner leg domain (indicated by arrows) with a size of approximately 20 nm which are not detectable in liposomes (Figure 31C and 31D). DOPC:SM:cholesterol proteoliposomes formed by the reconstitution procedure with Triton X-100 display indeed similar structures at the edge of the spherical shaped vesicles, but huge accumulations of aggregated liposome structures with various sizes (Figure 31E and 31F) which are also visible for liposomes alone (Figure 31G and 31H).

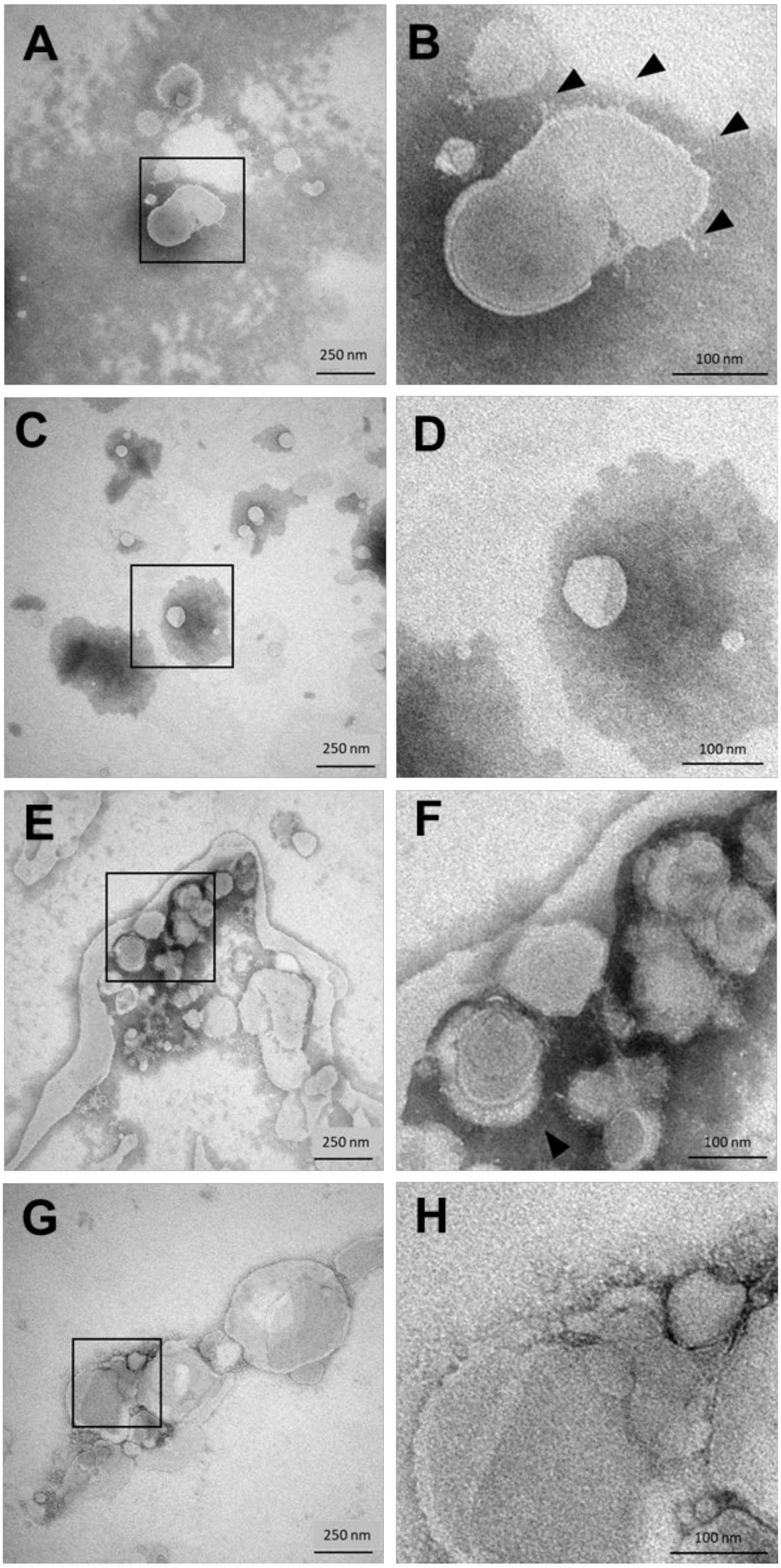

Figure 31: TEM images of (proteo)liposomes with different preparation methods. A) Proteoliposomes prepared with CHAPS protocol and DOPC:SM:cholesterol ratio 45:35:25. B) Rectangle insert close-up from A. Protein is indicated by the black arrows. C) Liposomes prepared with CHAPS protocol and DOPC:SM:cholesterol ratio 45:35:25. D) Rectangle insert close-up from C. E) Proteoliposomes prepared with Triton X-100 protocol and DOPC:SM:cholesterol ratio 45:35:25. F) Rectangle insert close-up from E. Protein is indicated by the black arrows. G) Liposomes prepared with Triton X-100 protocol and DOPC:SM:cholesterol ratio 45:35:25. H) Rectangle insert close-up from G.

The influence of varying lipid compositions on integrin activation was further analyzed using an adapted QCM-D setup which is already described in chapter 4.1.5. Briefly, blank liposomes or proteoliposomes were injected and a lipid bilayer was generated with an amphipathic, α-helical (AH) peptide derived from hepatitis C virus (Cho et al. 2007a; Cho et al. 2007b). After SLB formation, the membrane was treated with or without Mn^{2+} to induce potential integrin activation. Finally, PAC-1 antibody was injected and changes in frequency and dissipation were detected. The changes upon mass adsorption between *f* before PAC-1 injection and *f* after rinsing (Δ*f*) is displayed in Figure 32 and shows the PAC-1 binding to buffer (black)- or Mn^{2+}-treated (red) proteoliposome-derived SLB. Non-treated SLB with integrin show the highest PAC-1 binding (1.2 Hz) in the ratio 37.5:37.5:25, while 25:35:40 and 45:30:25 show the least changes in *f* (~0.2 Hz).

The question arises whether integrin activation could be impaired by the presence of different lipid ratios. Therefore, SLB was treated with Mn^{2+} to induce integrin activation and only the ratios 37.5:37.5:25 and 45:30:25, as well as the DMPG:DMPC derived SLB show high difference between Mn^{2+} treated SLB and the buffer control (>1 Hz), where the latter even increased from 1.1 to 4 Hz upon Mn^{2+} treatment. All other ratios (25:35:40, 60:28:12 and 70:25:5) display changes in *f* comparable to buffer controls. DOPC:SM:cholesterol proteoliposomes prepared with Triton X-100 exhibits vesicle fusion to the substrate, equilibrating at -150 Hz (Δ*f*) and 30 x 10^{-6} (ΔD). High changes in frequency and dissipation indicate the formation of a vesicle layer, therefore no formation of a SLB was observed, not even with AH-fusion peptide treatment, and PAC-1 binding is not reliable due to unspecific adsorption to the surface. The corresponding QCM graph is depicted in Figure S5.

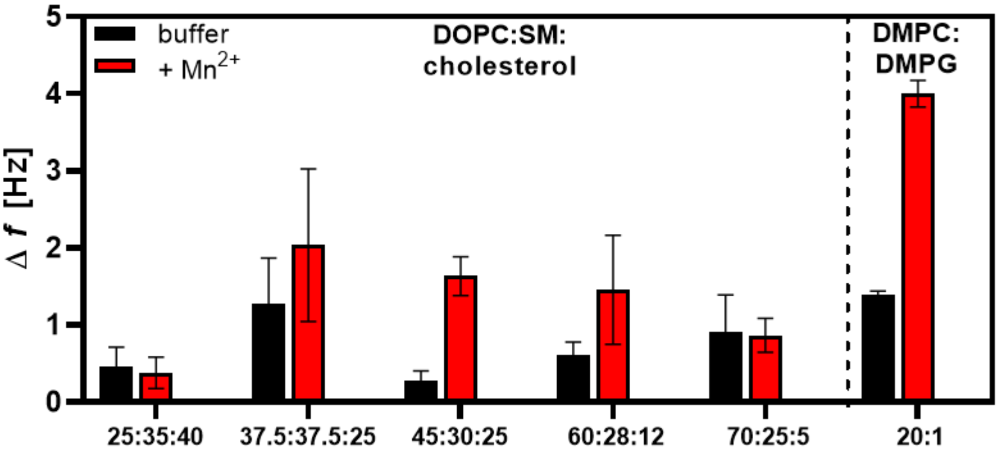

Figure 32: Activation of integrin αIIbβ3 reconstituted within different lipid ratios: Changes in Δ *f* upon injection start of PAC-1 were subtracted from values after rinsing. QCM-D experiments were carried out with proteoliposomes after treatment with buffer (black) or 1 mM Mn^{2+} (red) for at least 30 min at 37°C. DOPC:SM:cholesterol derived proteoliposomes with different ratios are injected onto a SiO_2 surface and vesicle fusion was forced with 13 µM AH peptide. Afterwards, membrane was treated for at least 30 min with either HEPES liposome buffer or buffer containing 1 mM $MnCl_2$, followed by injection of PAC-1 antibody diluted 1:50 in the respective buffer. Finally, membrane was rinsed with the respective buffer. Results correspond to two-three independent measurements ± SEM. Overall results are depicted in Table S1.

4.2. HEK293 cells as an expression platform and model system to study the impact of integrin on cell elasticity

Proceeding from the artificial membrane system and its many advantages, proteoliposomes alone are not able to mimic the highly complex network in cells, such as blood platelets. Platelets are highly active and can be triggered by various external influences including shear stress. Additionally, mutagenesis of platelets is not easily possible due to absence of the nucleus. Therefore, an integrin expression platform in HEK293 cells mimicking indeed the complex cell network but avoiding the delicate activation threshold of platelets was established. For understanding of the integrin activation and its effect on the actin cytoskeletal structures as well as resulting mechanical properties of the cell, mutations were introduced leading to constantly active or inactive integrins. Several setups where established to address impact of integrin αIIbβ3 on cell mechanical properties and are illustrated in Figure 33. Both adhesive and suspended cell elasticity was studied by the two biophysical methods AFM and RT-DC. Figure 33C shows a close up view of the cell membrane containing either integrin αIIbβ3 wildtype (WT), αIIb-(*ITGA2B*) R320C and β3-(*ITGB3*) R563C for inactive integrin mutant (αIIbβ3 Inactive) or β3-(*ITGB3*) C560R for the constantly active integrin mutant (αIIbβ3 Active). Talin-1 binds to the integrin cytoplasmic tails and connects them with vinculin and the actin filaments. Additionally, confocal images were taken to see the direct influence of integrin activation on the cytoskeleton.

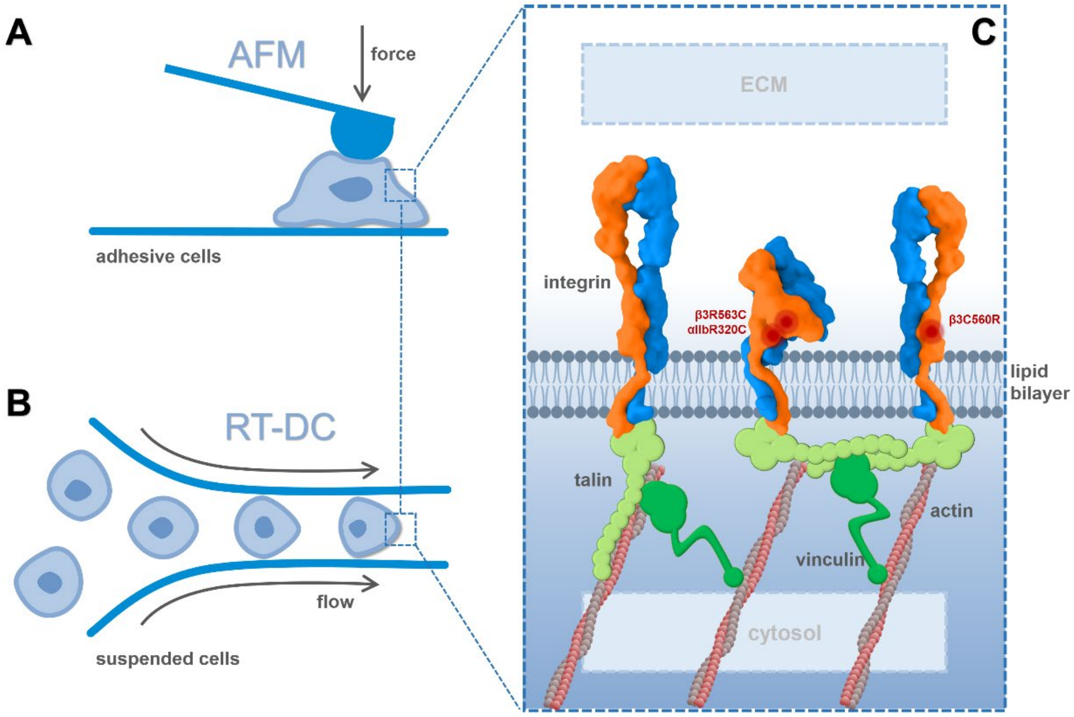

Figure 33: Schematic illustration of integrin effect analysis on cell mechanical properties. A) Elasticity of adhesive HEK293 cells was examined by AFM. B) Cell deformability in suspension was measured in RT-DC. C) Close-up of the interface between extracellular matrix (ECM) and cytosol of the cells (not in scale). The membrane is illustrated containing integrin αIIbβ3 (αIIb-blue; β3-orange) wildtype, mutations αIIb (*ITGA2B*) R320C and β3 (*ITGB3*) R563C for inactive integrin, as well as β3 (*ITGB3*) C560R for the constantly active integrin. The integrin cytoplasmic tail is related to talin-1, which is associated with actin and vinculin among others.

4.2.1. *Expression of integrin αIIbβ3 and co-localization*

For preparation of the integrin wildtype and mutant expressing cells, site directed mutagenesis was carried out and HEK293 cells were transfected to express the desired integrin protein. Plasmid DNA was verified by restriction enzyme digestion and Sanger-sequencing. Confocal microscopy imaging reveal presence of both subunits by fluorescently-labeled antibody staining. Fluorescence signal is displayed at the rim of the integrin expressing cells and is depicted in Figure 34. All cells show a profile size of around 20 nm. Integrin expression and membrane localization was validated and the fluorescence signal is evenly distributed over the entire edge of the cells.

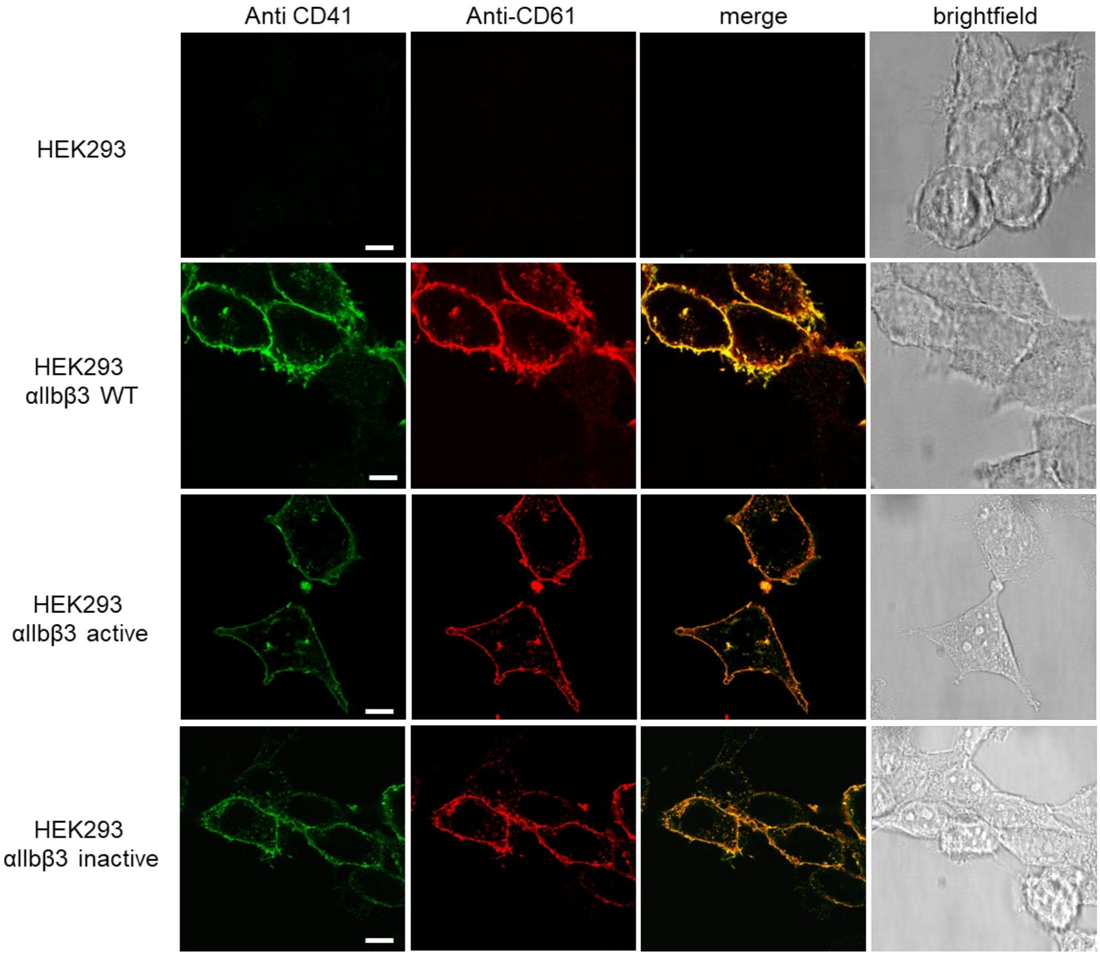

Figure 34: Representative confocal images of co-localized integrin subunits. Different cell lines were stained with primary antibodies from left to right: anti-CD41 Alexa 488 (green) and anti-CD61 Alexa 647 (red) in a dilution of 1:100. Both fluorescence channels are overlaid for co-localization in a merge picture and brightfield image is shown on the right. Scale bar corresponds to 10 µm for all images.

Furthermore, subunit expression was controlled by flow cytometry measurements. Figure 35 presents the results after staining the different cell lines with fluorescently-labeled antibodies against the αIIb- and β3-subunit. Additional to fluorescence signal, size and granularity can be detected *via* forward and side scatter (FSC and SSC) and are shown in Figure 35A. Cells of interest were gated in a FSC *versus* SSC plot to exclude debris and doublets. Single parameter histograms of single cells were used further to identify the expressed marker CD41, corresponding to the αIIb-subunit (B) and CD61, as marker for the β3-subunit (C), respectively. The appropriate frequency of positive signal is summarized in Figure 35D. HEK293 cells do not show any signal, while αIIbβ3 WT expressing cells have over 91 % CD41- and 89 % CD61-positive cells. Also, αIIbβ3 inactive cells show 94 % CD41- and 89% CD61-positive signal, which can be replicated by the αIIbβ3 active mutant cells (87 % CD41-positive, and 97 % CD61-positive cells).

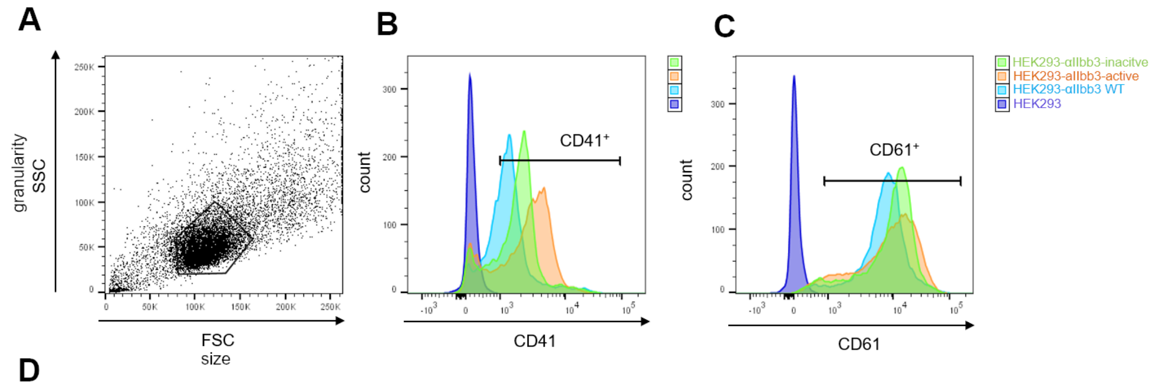

D

Cell line	Frequency of CD41 positive signals [%]	Frequency of CD61 positive signals [%]
HEK293	0.3 ± 0.2	0.3 ± 0
HEK293-αllbb3 WT	91.9 ± 1.8	89.4 ± 6.9
HEK293-αllbb3-inacitve	93.6 ± 3.7	98.3 ± 1.2
HEK293-αllbb3-active	87.3 ± 6.1	97.4 ± 0.9

Figure 35: Integrin subunit detection in flow cytometry. A) Representative FACS dot plot. The indicated gate (black) was further used for analysis by creation of a histogram of the fluorescence intensity of anti-CD41 Alexa 488 (B-CD41+) and anti-CD61 Alexa 647 (C- CD61+) diluted 1:100 in PBS from HEK293 (blue), HEK293-αIIbb3 WT (cyan), HEK293-αIIbb3 inactive (green) and HEK293-αIIbb3 active (orange) cells. Statistical analysis was done with FlowJo software and is summarized in D. Results correspond to three independent measurements ± SEM.

4.2.2. Integrin activation and cytoskeletal rearrangements

Integrin activation was induced by Mn^{2+} treatment and active conformation-specific antibody binding (PAC-1) to the different cell lines expressing wildtype (WT) as well as its integrin mutants was analyzed in a flow cytometer. Figure 36 shows all β3-positive single cells that are additionally positive for PAC-1 antibody fluorescence signal (gating strategy is presented in Figure S2). Control cell line (HEK293) shows no signal at all, whereas PAC-1 positive events increase in WT integrin expressing cells from 5 % to 20 % upon Mn^{2+} treatment. The constitutively active integrin expressing cells increase from 25 % to 70 % PAC-1 signal due to incubation with Mn^{2+}. Moreover, inactive integrin mutant cells show comparable PAC-1 binding as for WT integrin. The presence of EDTA, which leads to removal of divalent cations, leads to no PAC-1 binding to all four cell lines.

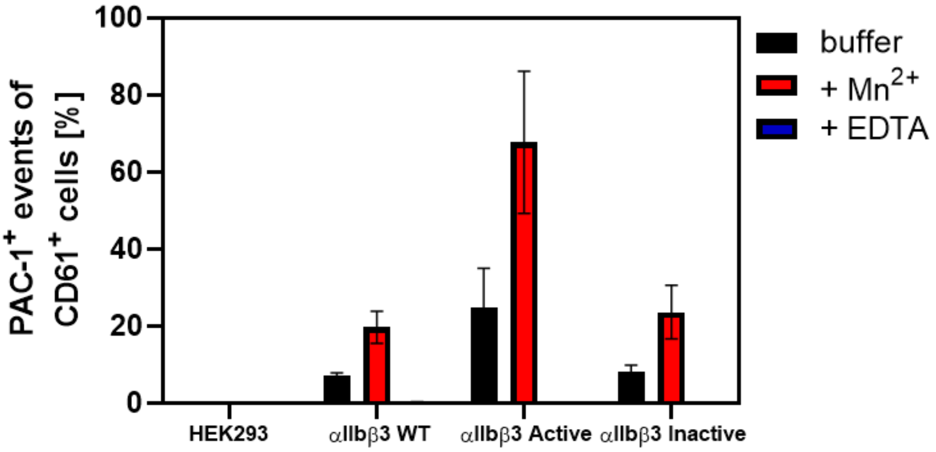

Figure 36: PAC-1 binding to cells expressing the β3-subunit variants. HEK293, HEK298 αIIbβ3 WT, HEK293 αIIbβ3 active and HEK293 αIIbβ3 inactive cells were incubated with anti-CD61 FITC antibody (1:100) and PAC-1 antibody conjugated with Alexa-647 (1:100) in PBS. Beforehand, cells were incubated 30 minutes with cell culture medium containing 1 mM Mn^{2+}, 5 mM EDTA or buffer. Statistical analysis was carried out using Flow Jo software. Single FITC and Alexa-647 positive cells are displayed. Results correspond to three independent measurements ± SEM.

Actin filaments are highly associated with the cytoplasmic tails of integrins and play a major role upon integrin activation and platelet aggregation, consequently (Durrant et al. 2017; Bearer et al. 2002). Therefore, confocal images of the actin filaments, and integrin were taken and compared to cells treated with Mn^{2+}. Figure 37 displays the cell lines HEK293, HEK293-αIIbb3 WT treated with and without Mn^{2+}, stained with phalloidin, to spot the actin filaments, and the FITC labelled integrin β3-subunit antibody. All cells show a size between 10 and 25 nm and cell nuclei stained with Hoechst 33242 (blue). Generally, actin filaments localize mostly at the membrane of the cells but form also small accumulations inside the cells. Integrin expressing cells (WT) display brighter actin filament signal at the edge of the cells but also at the interface between two cells, compared to control HEK293 cells. Especially Mn^{2+} treatment leads to small extensions of the membrane, called filopodia, in integrin expressing cells but less pronounced in HEK293 control cells.

In active mutant expressing cells (Figure 38) additional large fibers within the cytoplasm are visible. Inactive integrin expressing cells show phalloidin signal intensified at the edge of the cells, especially at the contact interface between two cells.

Furthermore, Mn^{2+} treated cells show also augmented lamellipodia along the edge of the cells. Additionally, all integrin expressing cells (with or without Mn^{2+} treatment) show anti-β3 antibody signal, particularly intense at the membrane of the cell, which leads to a co-localization of both phalloidin and integrin β3 signal in the merged picture indicated by a yellow color (Figure 38). Staining of activated integrin with the conformation specific antibody PAC-1 (Figure 39 and Figure 40) shows a significant signal exclusively in the active integrin mutant cell line treated with Mn^{2+} (Figure 40), which is located at the cytoplasm next to the membrane of the cell and appears as clustered dots. Additionally, the HEK293-αIIbβ3 active cell line shows filamentous structures in the phalloidin staining ranging from the nucleus horizontally through the membrane and are distributed in the whole cytoplasm.

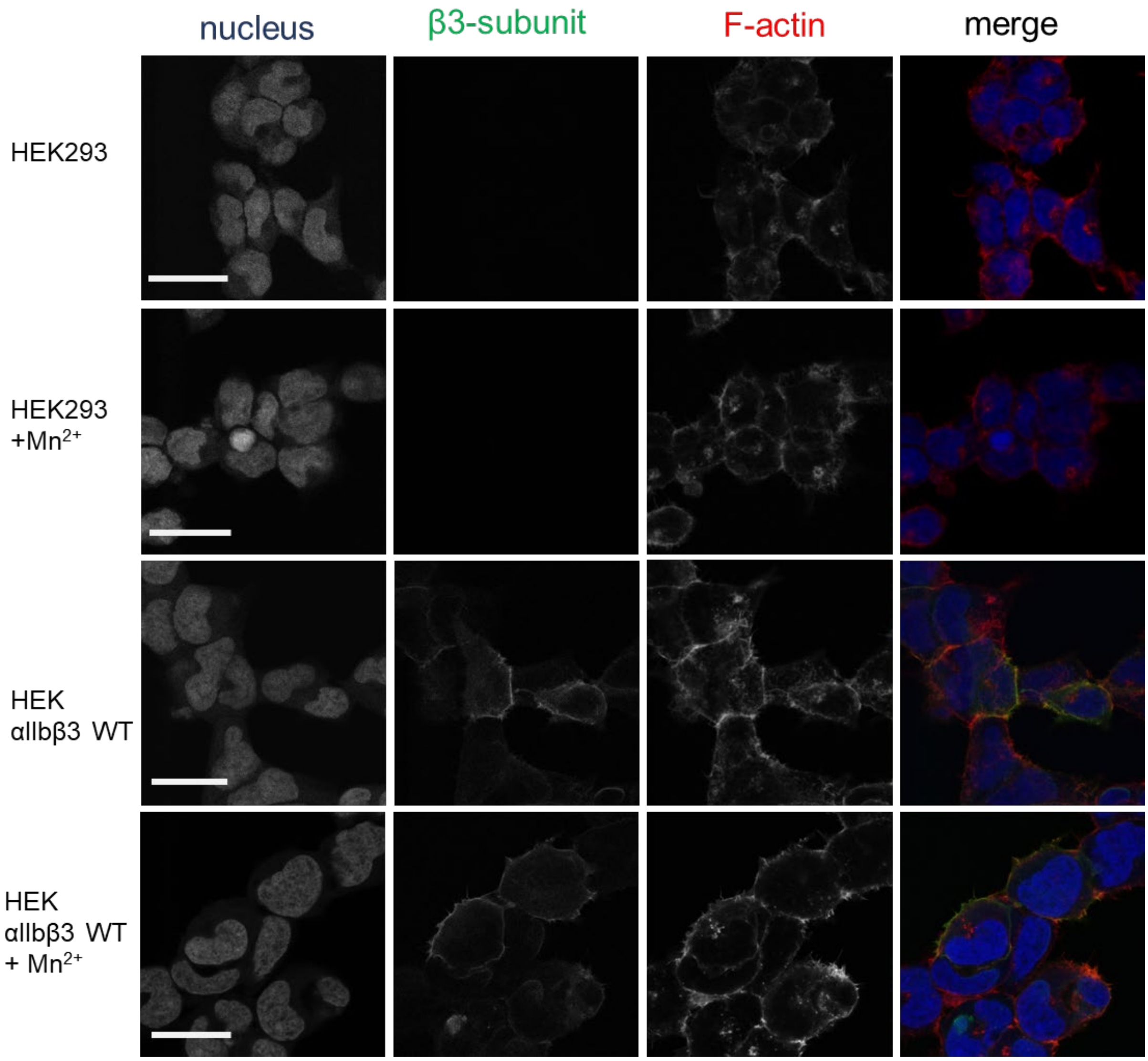

Figure 37: Representative confocal images of integrin β3-subunit and cell cytoskeletal structure. HEK293 and HEK293 integrin WT expressing cells were treated with and without 1 mM Mn^{2+} for 30 min and stained with phalloidin 647 (1:10) as well as anti-integrin β3 FITC antibody (1:40). Nucleus was stained using Hoechst 33242 (1:1000). All fluorescence channels (nucleus-blue, actin filaments-red and β3-subunit- green), are overlaid for co-localization in a merge picture. Scale bar corresponds to 25 μm for all images.

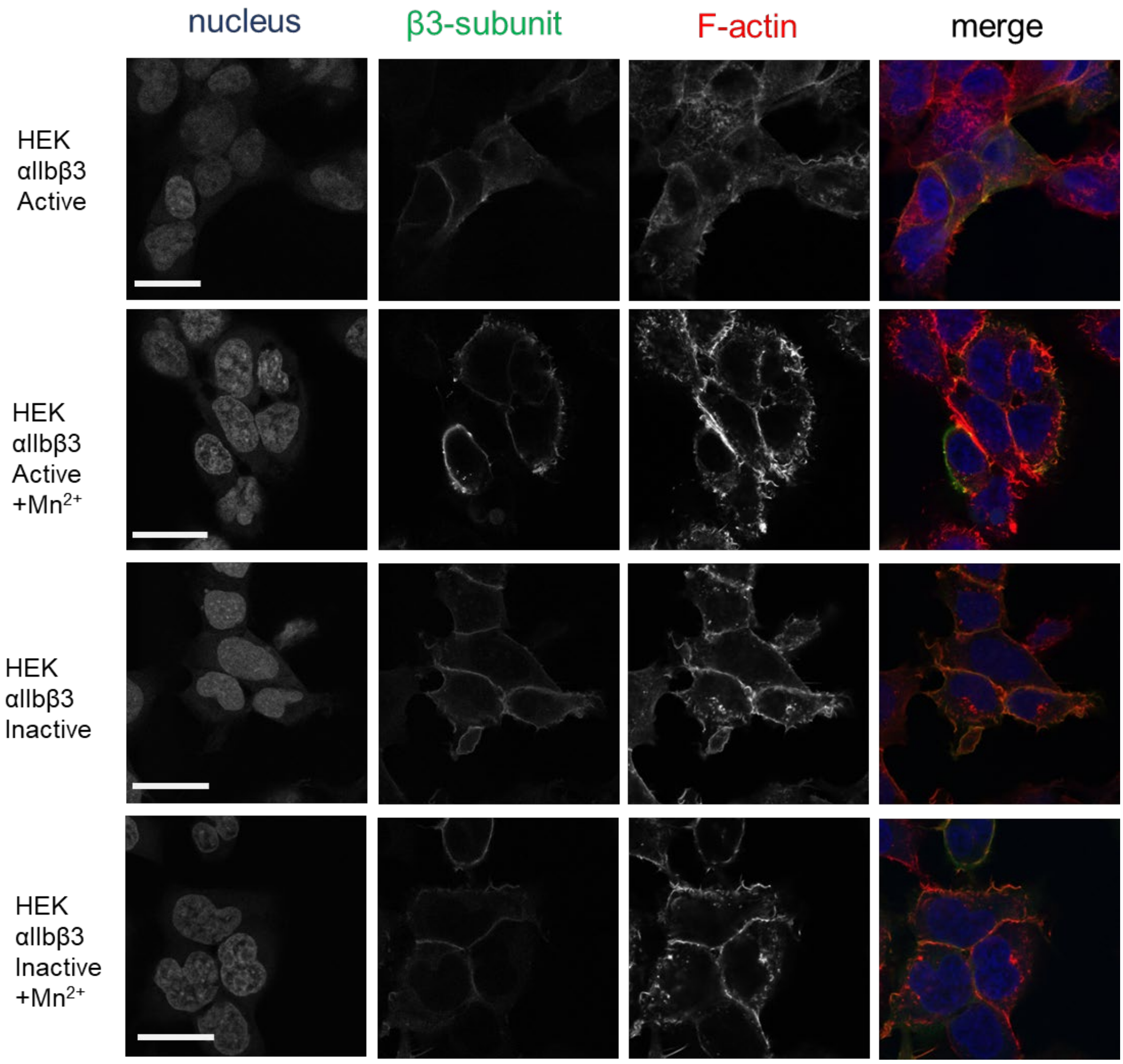

Figure 38: Representative confocal images of integrin β3-subunit and cell cytoskeletal structure of mutants. HEK293 expressing active and inactive αIIbβ3 mutants were treated with and without 1 mM Mn^{2+} for 20 min and stained with phalloidin 647 (1:10) as well as anti-integrin β3 FITC antibody (1:40). Nucleus was stained using Hoechst 33242 (1:1000). All fluorescence channels (nucleus-blue, actin filaments-red and β3-green), are overlaid for co-localization in a merge picture. Scale bar corresponds to 25 µm for all images.

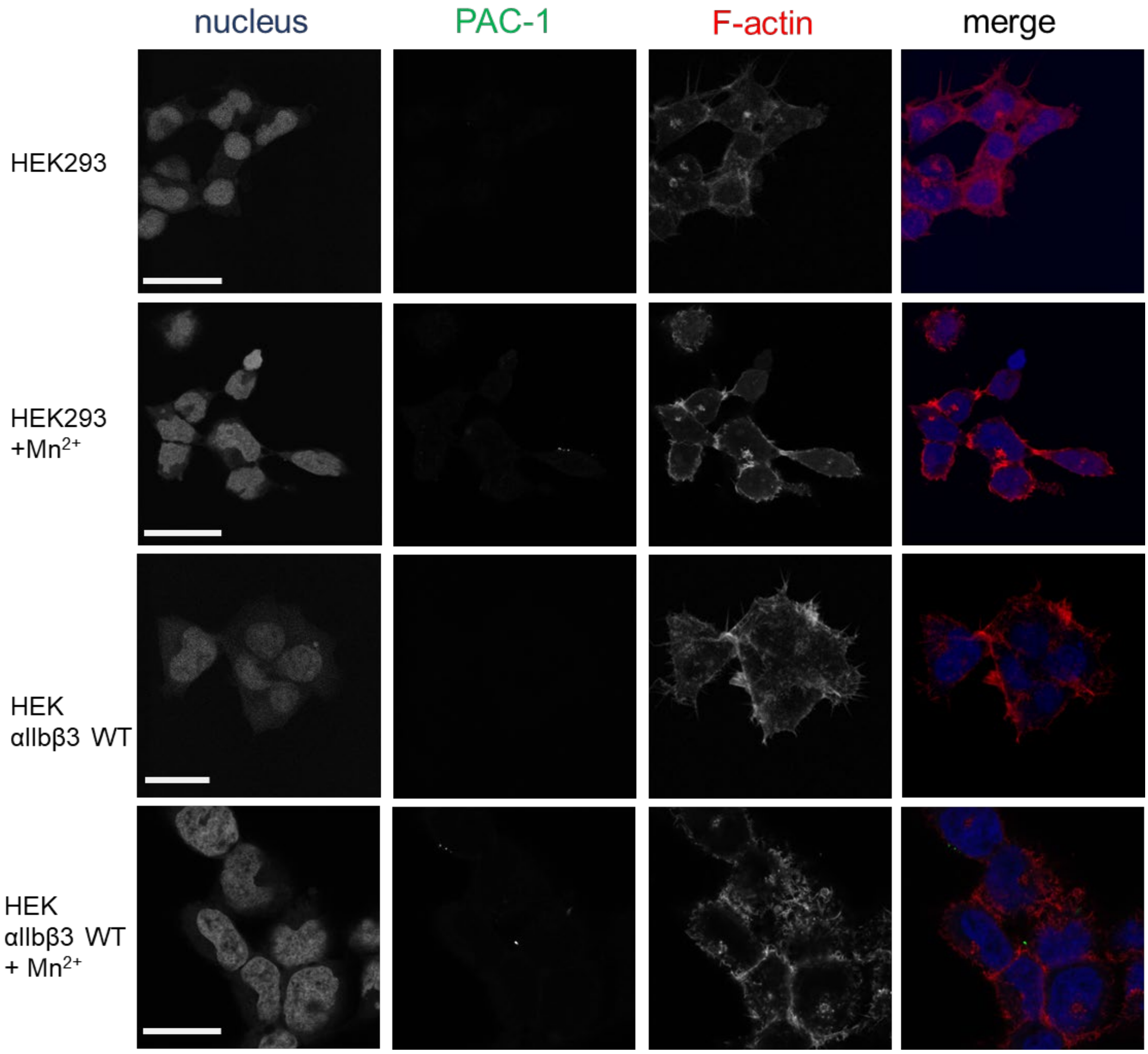

Figure 39: Representative confocal images of integrin activation state and cell cytoskeletal structure. HEK293 and HEK293 integrin WT expressing cells were treated with 1 mM Mn^{2+} and are stained with phalloidin 647 (1:10) as well as PAC-1 as primary antibody (1:10) and FITC-anti IgM as secondary antibody (1:10). Nucleus was stained with Hoechst 33342 (1:1000). All fluorescence channels (nucleus -blue, actin filaments-red and PAC-1 binding- green), are overlaid for co-localization in a merge picture. Scale bar corresponds to 25 µm for all images.

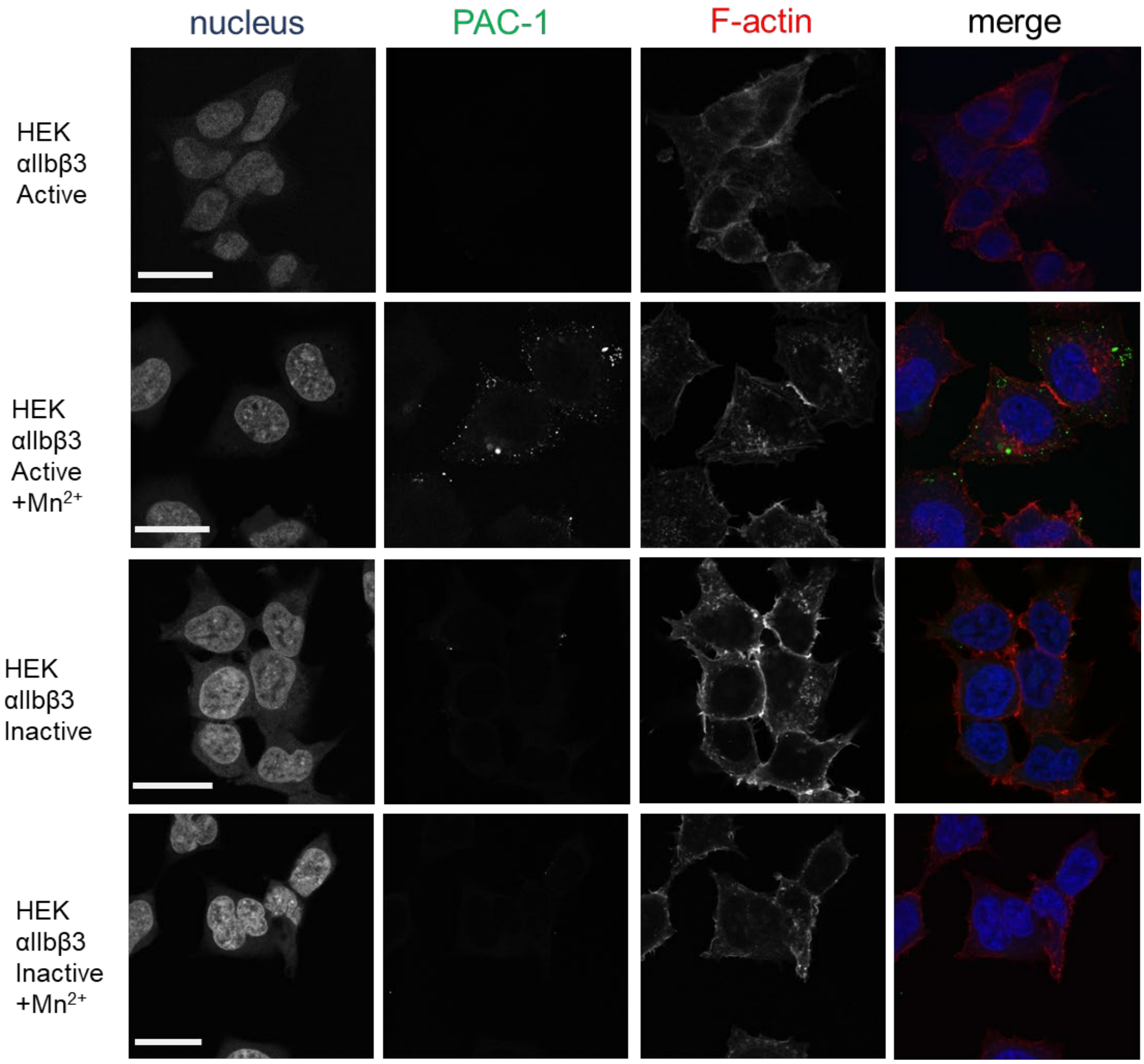

Figure 40: Representative confocal images of integrin activation state and cell cytoskeletal structure of mutants. HEK293 active and inactive integrin expressing mutant cells were treated with 1 mM Mn^{2+}and are stained with phalloidin 647 (1:10) as well as PAC-1 as primary antibody (1:10) and FITC-anti IgM as secondary antibody (1:10). Nucleus was stained with Hoechst 33342 (1:1000). All fluorescence channels (nucleus-blue, actin filaments-red and PAC-1 binding- green), are overlaid for co-localization in a merge picture. Scale bar corresponds to 25 µm for all images.

4.2.3. Cell elasticity and platelet integrin activation

Cell mechanical properties of the cell lines HEK293, HEK αIIbβ3 WT, HEK αIIbβ3 inactive and HEK αIIbβ3 active in adherent and suspension state were measured using two methods: AFM and RT-DC corresponding to adherent and suspended state, respectively. Young's modulus (YM) was calculated and the estimated marginal means and standard error of the means are obtained from a linear mixed effect model in R (software R). The used model considers clustering and distribution of datapoints and was therefore selected to display the results. First, YM of all cell lines obtained from both methods were compared in Figure 41.

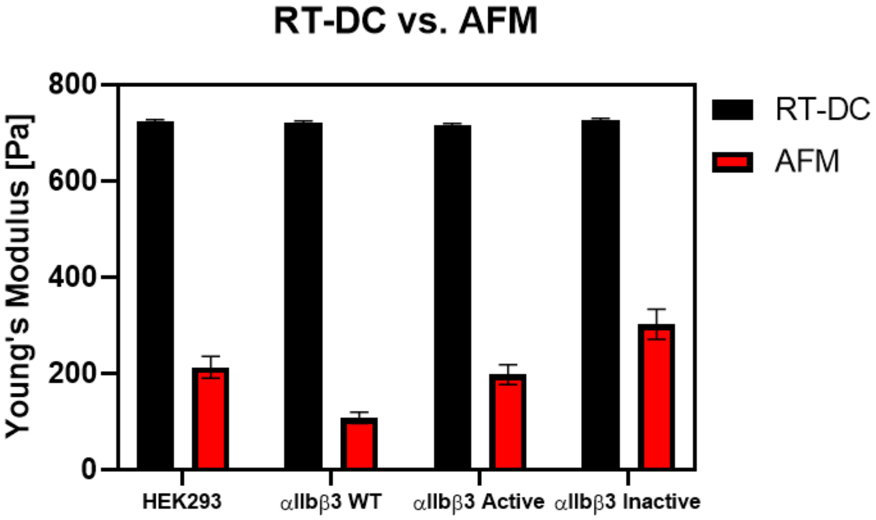

Figure 41: Cell elasticity in AFM *versus* RT-DC measurement. Marginal means of measured Young's Modulus of untreated HEK293, HEK αIIbβ3 WT, HEK αIIbβ3 active and inactive cells in RT-DC (black) and AFM (red). Statistical analysis was carried out from linear mixed models and error bars represents standard error of the mean.

HEK293 cells show a mean YM of 212 Pa in AFM, but threefold higher values of 720 Pa in RT-DC. Same significance is present in HEK αIIbβ3 WT cells where AFM measurements give YM means at 107 Pa, whereas RT-DC studies show mean YM of 719 Pa. Although no significant differences can be observed in RT-DC studies, integrin WT and active mutant expressing cells are softer than control HEK293 and αIIbβ3 inactive cell lines in AFM measurements. Cells expressing active mutant of integrin show YM of 725 Pa in RT-DC and 196 Pa in AFM, where this difference is also displayed in inactive mutant expressing cells but with generally increased YM.

Since literature from the past decades and previous liposome studies described in Chapter 4.1.5 show the importance of divalent cations ions, especially Mn^{2+} ions, for the structure and activation state of integrin αIIbβ3, the influence of integrin activation, induced by these ions, on the cell elasticity was studied (Figure 42). Control cells in adherent state measured in AFM show upon Mn^{2+} treatment softer cells changing mean YM from 212 Pa to under 120 Pa, whereas Mn^{2+} treatment of integrin WT cells lead to increased mean YM ranging from 107 Pa of untreated up to 160 for Mn^{2+}- treated cells. The same trend is observable for the active mutant expressing cells with YM for untreated cells at 196 Pa and ion treated cells at 225 Pa (Figure 42A). Inactive mutant represents the opposite trend, with decreasing YM caused by Mn^{2+} incubation, with highest YM at 300 Pa to 290 Pa. Basically, integrin WT and active mutant expressing cells give lower mean YM values compared to HEK293 control cells, while inactive mutant shows highest YM.

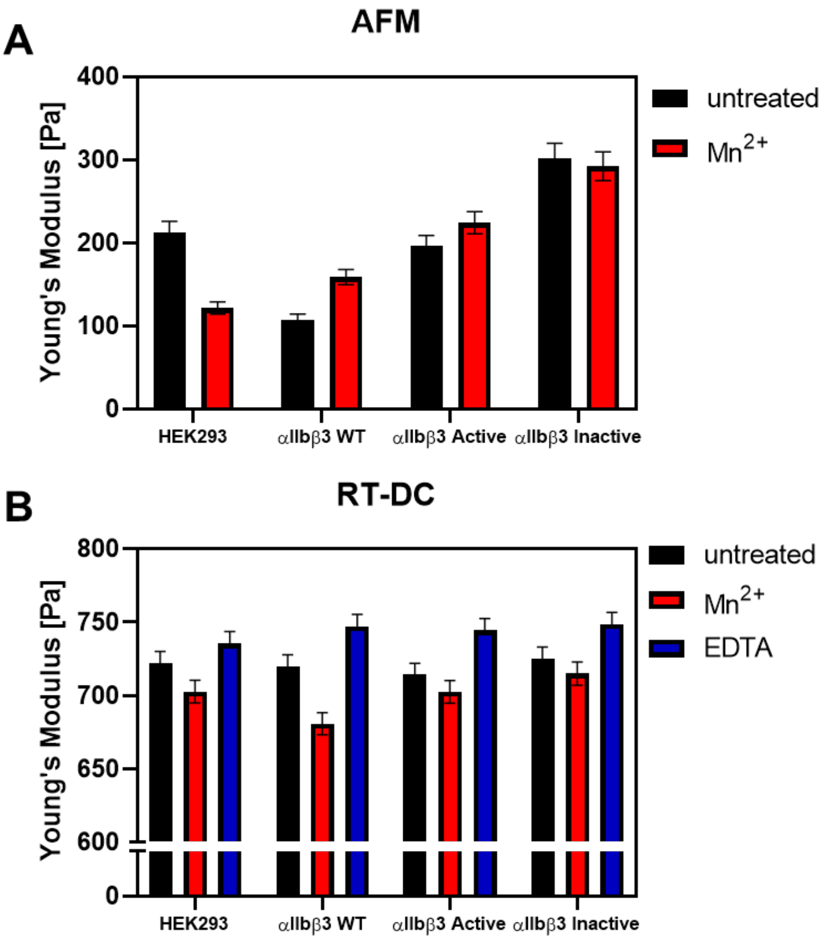

Figure 42: Cell elasticity upon different treatment in AFM and RT-DC. A) Mean Young's Modulus of HEK293 , HEK293 αIIbβ3 WT, HEK293 αIIbβ3 active and inactive cells treated with 1 mM Mn^{2+} measured in AFM and B) treated with 1 mM Mn^{2+} or 5 mM EDTA in RT-DC. Statistical analysis was carried out from linear mixed models and error bars represents standard error of the mean.

By contrast, comparing adherent cells with the cells in suspension, the results demonstrate another tendency regarding the elasticity (Figure 42B). Integrin-expressing cells show significantly reduced mean YM after treatment with Mn^{2+} compared to the respective untreated cells. The most significant effect is observed in integrin WT expressing cells with YM going from 720 Pa to 680 Pa. EDTA treatment, which captures all divalent ions, leads to increased YM in all four cell lines, especially in integrin expressing cells (WT and mutant), reaching values up to 750 Pa. Additionally, except inactive mutant cells, all cells are basically softer than control HEK293 cells. The results already indicate the importance of the adhesion state for different integrin-conformation cell lines.

5. Discussion

5.1. Liposomes as biomimetic system

In the first part of this thesis a membrane-like biomimetic system (liposomes) was applied to study the platelet integrin αIIbβ3, excluding any additional manipulations caused by e.g. platelet activators or other signaling proteins. Therefore, integrin alone was characterized prior to reconstitution procedure. ELISA and reductive SDS-PAGE reveal that both subunits are present in the protein stock. Utilized concentrations of the two antibodies to reach potential saturation assume different affinities (Hulme and Trevethick 2010). Integrin shows a size of 15 nm in DLS, which is supported by AFM measurements of pure air dried integrin, showing a size of approximately 22 nm, considering lateral AFM tip convolution artifacts and consequently decreased lateral resolution because of the tip geometry (Canet-Ferrer et al. 2014). AFM images confirm the DLS results and literature values for the size of the integrin (Bennett 2005). Moreover, protein stability was checked by DLS by heating the integrin, resulting in aggregation and an increase in size, consequently. By application of a thermal denaturation plugin assuming a two-state model (Niklasson et al. 2015), a melting temperature of 50.5 °C was determined, which is slightly lower than already published for fragments of integrin αIIbβ3 (Makogonenko et al. 1996) as well as T_m forecasted by prediction websites (Ku et al. 2009).

To study the membrane protein integrin αIIbβ3 in a biomimetic and artificial physiological environment in QCM-D, conditions for lipid bilayer formation were examined. Since Frohnmayer et al. used egg PC and egg PG for αIIbβ3 reconstitution (Frohnmayer et al. 2015), these lipids were initially chosen for QCM-D experiments and vesicle rupture was studied. High amounts of PC lead to a typical bilayer formation with a temporary huge frequency and dissipation change due to vesicle adsorption and water release during fusion, coming to a baseline at -25 Hz and a dissipation between 0-1 x 10^{-6} (Richter et al. 2003; Richter et al. 2006). Interestingly, at higher amounts of PG, only vesicle layers are formed without any rupture event. This could be due to the fact that the potential negative charge by the headgroup of PG leads to small rejections between liposomes that cause a low coverage of the surface, consequently. It is known, that a low coverage promotes vesicle layers, but no vesicle fusion (Hardy et al. 2013). Additionally, the lack in formation of SLBs with PG was assigned to its charged head groups, but also the molecular shape (Israelachvili et al. 1976; Lind et al. 2019), considering that these lipids do not prefer the lamellar structure of a bilayer (Lee 2004).

By contrast, PC has a cylindrical shaped head group and will self-assemble into a lamellar phase similar to biological membranes (Lee 2004; Dickey and Faller 2008). Though, the existence of "non-bilayer" lipids, as PG, in membranes has been found to be required for certain transmembrane proteins to maintain its functionality and conformational state (Lee

2004). Consequently, a higher egg PC:egg PG ratio was chosen for bilayer formation and therefore used in the integrin reconstitution procedure.

Frohnmayer et al. (Frohnmayer et al. 2015) assumed integrin reconstitution within egg PC and egg PG but without substantial evidence. In addition, the protocols carried out in this thesis also demonstrated no integrin reconstitution with these lipids. Moreover, the studies of Erb and Engel (Erb and Engel 2000) confirm no reconstitution success. Potentially, detergent and its CMC (critical micellar concentration) as well as unsaturation of lipids play a role. Hence, the protocol was changed to DMPG and DMPC, that show same results as egg PG and egg PC in SLB formation behavior, but successful integrin reconstitution. The dissipation increased upon higher amounts of DMPG, corresponding to a vesicle layer and no SLB (Richter et al. 2006), whereas higher DMPC levels led to SLB formation. Therefore, 20:1 DMPC:DMPG ratio was selected for αIIbβ3 reconstitution and further experiments.

The successful reconstitution of αIIbβ3 into DMPG:DMPC liposomes was demonstrated by DLS showing larger proteoliposomes compared to bare liposomes. Additionally, TEM images confirm the association of the typical integrin structure, with a head domain and its two stalk domains (Bennett 2005; Takagi et al. 2002), attached or inserted to the membrane of the vesicles, which was also presented by the authors of the original reconstitution protocol (Erb and Engel 2000). Both αIIb- and β3-subunits can be detected by flow cytometry *via* binding of subunit specific antibodies, and SDS-PAGE showing the corresponding αIIbβ3 bands (Bennett 2005). In this thesis, it is expected, that potentially occurring oppositely orientated integrins reconstituted into liposomes do not contribute to activation measurements and adhesion.

5.2. Integrin activation in liposomes

For detection of activated integrin, several complementary methods were used. One of them is the already described QCM-D technique, which enables the study of liposome rupture and formation of supported lipid bilayers (Jing et al. 2014; Frohnmayer et al. 2015; Hardy et al. 2013; Lind and Cárdenas 2016). Frohnmayer et al. investigated the binding of αIIbβ3 proteoliposomes to extracellular matrix in QCM-D (Frohnmayer et al. 2015), but the system shown in this thesis, and in the resultant publications (Janke et al. 2019; Martens et al. 2020) has not been previously contemplated for the interaction measurements of SLBs containing full-length αIIbβ3. Proteoliposome injection leads to a decrease in frequency (*f*), which is comparable to the blank liposome measurement. However, a strong rise in dissipation (*D*) upon injection can be observed indeed, but not as high as it would be expected without any SLB formation (Richter et al. 2006). The different values of *D* compared to blank liposome injection, can be explained by either the grand ectodomain of the 235 kDa αIIbβ3 (Adair and Yeager 2002) or small amounts of proteoliposomes remaining on the saturated SLB covered SiO_2 substrate (Richter et al. 2003). Additionally, AFM results confirm the formation of a bilayer with a height of ~4.3 nm (Goksu et al. 2009) in both liposome- and proteoliposome-treated SiO_2 surface emerging from QCM-D experiments. The integrin-containing bilayers shows additional clusters with a height between 8 and 10 nm within the bilayer. Lateral resolution implies clustering of integrins, but decreased lateral resolution due to tip geometry must be considered. Moreover, contact mode imaging leads to remaining biomaterial at the cantilever wherefore artifacts increase, displayed as small triangular structures.

QCM-D measurements, as well as flow cytometry and activation assay results show an increased binding of the conformation-specific antibody PAC-1 upon treatment with Mn^{2+} compared to standard buffer conditions and after capture of divalent ions with EDTA. This binding directs to the importance of divalent ions such as Ca^{2+} and especially Mn^{2+} for an activation process of αIIbβ3, which was also subject in other studies over the past decades (Zhang and Chen 2012; Frohnmayer et al. 2015; Ye et al. 2010; Litvinov et al. 2012). Prior studies revealed eight divalent cation binding sites in the head domain auf αIIbβ3 (Zhang and Chen 2012). In detail, the MIDAS, which is important for integrin ligand binding, is able to bind Ca^{2+} and Mg^{2+}, while other binding sites are only capable of binding Ca^{2+}. These metal ions initiate structural changes in the integrin head domain, resulting in a displacement of the α7-helix (Figure 5B) by two helical turns upon integrin activation (Zhang and Chen 2012; Campbell and Humphries 2011). It is controversially debated if a complete activation of αIIbβ3 is reached, once Mn^{2+} compete with the divalent ions in the integrin head and increases the ligand affinity (Kamata et al. 2005). The results of this thesis reveal PAC-1 binding and assume Mn^{2+}-induced activation of αIIbβ3. However, in the activation assay also control buffer shows increased activation, which could be due to long incubation times with PAC-1 antibody or unspecific binding to the microtiter plate.

CD spectroscopy measurements should clarify whether the opening of the head domain, due to activation, correlates to changes in the protein secondary structure. Several studies concentrate on specific domains of the integrin reaching from the I domain of leukocyte integrin (Fairbanks et al. 1995), or head domain of α3β1 (Furrer et al. 2006) and the cytoplasmic as well as transmembrane fragments of αIIbβ3 (Li et al. 2002). In this thesis, full-length integrin in a lipid environment was considered. Moreover, the integrin motion upon activation was predicted by crystal structures (Xiong et al. 2002) and MDS studies (Puklin-Faucher et al. 2006; Gahmberg et al. 2009) but do not show major changes in integrin secondary structure upon activation. Taken together with the CD results in this thesis, findings confirm the switchblade model for integrin activation, as it was shown by several groups (Zhu et al. 2008; Takagi et al. 2002; Beglova et al. 2002; Bidone et al. 2017; Kulke and Langel 2020). Here, a drastic rearrangement of the extracellular domain structure by a switchblade-like opening of the interface between headpiece and stalk domain leads to the extension of the ligand binding domain away from the plasma membrane. Dramatic changes in secondary structure do not occur, which can be explained by presumable motion of basically disordered regions e.g. the flexible knee region between the EGF- domains of the β-subunit (Zhu et al. 2008). Nevertheless, due to solvent shifts resulting from hydrophobic lipid environment, differential light scattering or absorption flattening effects (Miles and Wallace 2016; Ciancaglini et al. 2012), evaluation of CD results from liposomes/proteoliposomes is complicated. In addition, lipid-to-protein ratio, which was in this thesis as about 1000:1, influences strongly the data quality resulting in the exclusion of lower wavelengths in CD spectra data evaluation and limited extend of data deconvolution (Ciancaglini et al. 2012).

MDS studies, implemented to confirm CD data, show minor changes in β-sheet content of the knee region of both integrin subunits, which includes calf-1 and EGF2 domain, respectively. Looking at the overall β-sheet probability, finally reduced force is needed for unfolding the protein by e.g. Mn^{2+} treatment due to a decrease in the interaction between thigh and calf-1 as well as EGF1 and EGF2 domains. These changes could be assigned from the MIDAS to the rearrangement of the β-sheets in the β-propeller. However, exclusion of divalent cations in MDS results in random changes of secondary structure in all integrin domains, whereas experimental EDTA-induced removal of divalent ions leads to differing results. Experimentally, might be that several ions are not reachable by EDTA and stay coordinated in the head domain or even EDTA could impact the (proteo)liposomes due to destabilizing lipid effects (Prachayasittikul et al. 2007). If assumed that only MIDAS, ADMIDAS and SyMDS ions, located in the β-subunit, are extracted in MDS, changes in integrin secondary structure might be insignificant such as in experimental data.

Summarized, the results reveal, minor secondary structural changes during Mn^{2+}- induced activation of αIIbβ3.

5.3. Influence of clinically relevant drugs on integrin activation

The introduced biophysical methods were applied to test clinically relevant drugs (quinine, unfractionated heparin and fondaparinux) for their effect on αIIbβ3 activation. Especially quinine and unfractionated heparin (UFH) are known to be involved in drug-induced thrombocytopenia and interaction with αIIbβ3 (Visentin and Liu 2007). Although low concentrations of quinine do not lead to changes in secondary structure in CD spectroscopy experiments, quinine treatment induces PAC-1 binding indicating αIIbβ3 activation. The blood plasma concentration of quinine in treated patients with uncomplicated *falciparum malaria* is approximately 6 µg/mL and it was not achieved in the CD measurements in this thesis, due to its chirality (Vieira et al. 2008). Nonetheless, potential structural changes upon integrin activation could be the consequence of possible binding sites of quinine involved in the swing-out movement by the β3 α7-helix interaction with the hybrid domain (Campbell and Humphries

2011). Two probable explanations can describe the interaction of quinine to αIIbβ3. On the one hand, quinine binds to the αIIbβ3 head domain and leads to the extended state resulting in PAC-1 binding, consequently. On the other hand, quinine facilitates the interaction between PAC-1 IgM antibody and αIIbβ3 independently from the conformational state due to increased affinity. The latter was presented recently for quinine dependent mouse antibodies (Bougie et al. 2015; Bougie et al. 2006; Zhu et al. 2015), whereas option one suited to the displayed results in this thesis showing the quinine-induced activation of αIIbβ3. This might provoke the exposure of cryptic epitopes such as ligand-induced binding sites, leading to drug-induced thrombocytopenia and high bleeding risk, consequently (Visentin and Liu 2007).

Interestingly, heparin (UFH) treatment of integrin initiates other changes in secondary structure compared to Mn^{2+} treatment shown by oppositely influenced CD-spectra minimum, while both lead to αIIbβ3 activation as shown in QCM-D and activation assays.Additionally, other studies with integrins showing heparin binding to homologous regions to the β3-subunit in their head domains, respectively (Vorup-Jensen et al. 2007; Ballut et al. 2013). Probably, activation is stimulated by UFH and Mn^{2+} but initiated by different mechanisms. Hence, interaction of UFH with the RGD binding site of αIIbβ3, which was shown already elsewhere (Sobel et al. 2001), could cause the extension of the integrin and in PAC-1 binding, consequentially. On the contrary, fondaparinux treatment reveals neither strong activation of αIIbβ3, nor changes in secondary structure. Obviously, varying lengths of sulfated polysaccharide chains contacts contrarily αIIbβ3, as it was shown also for other proteins e.g. platelet-factor 4 (PF4). In this instance, heparin/PF4 complex-induced thrombocytopenia is accompanied by potential platelet activation by αIIbβ3 (Gao et al. 2011; Kreimann et al. 2014).

To conclude, Mn^{2+}, quinine and UFH treatment induce the action of αIIbβ3 and show only minor changes in integrin secondary structure. The presentation of hidden regions in the integrin head domain region upon extension of the extracellular parts, could lead to induction of immune system response and immunogenicity in some patients (Bhoria et al. 2015; Visentin and Liu 2007). The presented platelet membrane mimicking system enables the investigation of potential binding of e.g. autoantibodies under almost infinitely possible conditions and may become of increasing importance in clinical research.

5.4. Interaction of integrin αIIbβ3 with fibrinogen-nanoparticle bioconjugates

Apart from clinically relevant drugs, also nanoparticles are becoming more and more important in research and diagnostics e.g. targeted drug delivery. Especially, superparamagnetic NPs are frequently used because of their biocompatibility and stability, among others (Mahdavi et al. 2013). Due to blood contact upon injection, a protein corona is formed by high abundant proteins such as fibrinogen, and cell interactions of e.g. platelets with the formed bioconjugates might also be induced. Therefore, fibrinogen corona formation was detected by increase in size and a decreased zeta potential after protein corona formation.

Interestingly, PEGylated NPs show less fibrinogen corona formation in all used methods compared to citrate- and dextran- coated bioconjugates. PEGylation of NPs is a strategy to shield the NP surface from aggregation and protein adsorption as well as prolongation of blood circulation time (Suk et al. 2016), thus explaining the slow protein adsorption and the absence of corona formation (Martens et al. 2020). Once injection through the blood occurred, potential binding to cell membranes and receptors could be induced, as it is already described elsewhere (Fröhlich 2016). The previously described biophysical setup using QCM-D, can be applied to study the interaction of differently coated NPs with the introduced artificial platelet-like membrane system containing integrin αIIbβ3 receptor. After SLB formation with- and without integrin, changes in frequency and dissipation are measured during NP injection. There was only minor adsorption of bare NPs to blank lipid bilayer, whereas strong binding to integrin-containing bilayer was detected for citrate- and dextran-coated NPs. This effect could be due to the impact of various adhesion forces between blank NP surface and integrin inserted in the bilayer, such as electrostatic, hydrophobic and van-der-Waals forces (Auría-Soro et al. 2019; Zhao and Stenzel 2018).

However, PEGylated NPs without- or even with fibrinogen corona show comparable low changes in mass adsorption. In accordance with the NPs characterization data, a potential explanation is an interplay of the minor amount of protein corona formation and the properties of PEG leading to steric hindrance for blood component binding, which results in acceptance by the immune system and a high circulation time in the body (Suk et al. 2016). Fibrinogen corona formation for dextran and citrate NPs lead to lower adsorption to integrin-containing bilayer, which can be explained by the diminished surface energy and reduction of unspecific binding, consequently (Di Silvio et al. 2017; Lesniak et al. 2012). It has to be mentioned that the particle number differs between the different coating, thus effects on the binding behavior to the membrane could not be excluded. Additionally, fibrinogen circulates in the human blood at high concentrations (2-4.5 mg/mL) (Kattula et al. 2017), whereas in bioconjugate preparation initially 1 mg/mL fibrinogen was applied and after magnetic separation concentration was even lower. However, also pure fibrinogen shows only minor interaction with proteoliposome-derived bilayer.

Stability, but also integrin dynamic and activation depends strongly on divalent cations, e.g. Ca^{2+}, Mg^{2+}, Mn^{2+}. Therefore, lipid bilayers were treated with these ions to activate the integrin and to make ligand binding feasible. This biophysical setup mimics the stimulation of platelets and its potential interaction with NPs in an artificial biomimetic system. Interestingly, even the alternation from divalent ions-containing buffer to PBS without divalent cations lead to changes in both bilayer and integrin-containing bilayer, which was not observed for blank SiO_2 surface.

In conclusion, divalent cations lead to a significantly softer and thicker bilayer due to potential hydration of the lipid headgroups and swelling of the interfacial water, consequently (Alsop et al. 2016). However, it should be mentioned, that all NPs are suspended in PBS without any divalent cations due to aggregation of NPs. The buffer mismatch during treatment of bilayer and NPs injection results in hardly estimated shifts in frequency and dissipation, that need to be evaluated carefully. Nonetheless, dextran and citrated NPs, as well as their bioconjugates, result in a shift that exceeds the buffer mismatch for integrin-containing bilayer. Bioconjugates show increased binding affinity for divalent cation-treated integrin bilayer compared to untreated proteoliposome-derived bilayer. These findings confirm, the importance of divalent cations for integrin stability and activation (Janke et al. 2019; Campbell and Humphries 2011). The αIIbβ3 head domain opens up upon Mn^{2+} treatment and exposes the binding site for fibrinogen through a RGD sequence in the fibrinogen Aα chain or by the KQAGDV motif located in the γ chain (Hantgan et al. 2010). On the contrary, both PEG NPs and their fibrinogen-conjugated modification show only minor changes in adsorption for both liposome- and proteoliposome-derived bilayer, whereas viscoelasticity arises upon NP injection, which could be explained by the hygroscopic effect of PEG (Baird et al. 2010).

In conclusion, fibrinogen bioconjugates of dextran and citrated NPs bind especially to Mn^{2+}-treated integrin-containing bilayer, while PEGylated maghemite NPs with and without fibrinogen show only minor contact under both conditions. The shielding effect of PEG could lead to a reduction of unspecific binding of blood components to the injected NPs and could possibly protect from activation of immune cells and platelet aggregation, as it is known already from other studies with various NPs (Suk et al. 2016; Guildford et al. 2009; Fröhlich 2016). Upon platelet stimulation, where activated integrins are present, the results reveal NPs major role in clot formation. Additionally, the biophysical setup could be applied in future experiments predicting NP binding to biomimetic membranes and thus, importance for targeted drug delivery and elimination of toxicity, consequently.

5.5. Influence of the lipidic system on integrin dynamics

The perfect state for an artificial membrane mimicking system would be an environment closely related to the physiological lipid bilayers that belted the different membrane proteins in cells. Recreation of these complex environment is almost impossible, but a more appropriate lipid membrane system was aimed during this thesis. DMPC and DMPG have saturated short fatty acid chains and are mostly prominent in prokaryotic membranes (Cronan and Thomas 2009). Integrin αIIbβ3 is unfailingly expressed in mammalian cells, specifically blood platelets and its progenitors megakaryocytes, which leads to the development of a reconstitution protocol containing components of such membranes, e.g. DOPC, SM and cholesterol (O'Donnell et al. 2014).

Firstly, DMPG and DMPC were replaced by the DOPC (unsaturated lipid), SM (saturated lipid) and cholesterol, lipids that are especially in the external leaflet of the platelet membrane, but protocol remains unchanged with hydrophobic adsorption (biobeads) of Triton X-100. Indeed, much protein was detected after density gradient in a reductive SDS-PAGE, but a highly heterogeneous mixture of huge liposomes was formed. Additionally, TEM images confirm aggregation of both liposome and proteoliposome sample.

Upon synthesis of lipid embedded membrane proteins in liposomes, several detergents are suitable for reconstitution of membrane proteins depending on several factors such as lipids, proteins and lipid-to-protein ratios. One important aspect is the CMC that is defined as the minimal concentration of detergent that is needed for formation of micelles of individual detergent molecules (Rosen and Kunjappu 2012). This leads to a change in surface tension and depends on factors such as pH, ionic strength, temperature, presence of protein and lipids. Additionally, different detergents have different properties, that can be advantageous or drawbacks for reconstitution protocols. For instance, Triton X-100, a nonionic detergent, inhibits activity of reconstituted proton pump channel or changes the orientation of bacterial transporter protein within the liposome membrane (Seddon et al. 2004). This detergent, with a low CMC, is suitable for detergent removal by hydrophobic adsorption, e.g. with biobeads, as it was done in the used protocol.

However, the zwitterionic detergent CHAPS can be easily removed by dialysis due to its high CMC and the disintegration into micelles or into smaller monomers with a dilution below the CMC (Seddon et al. 2004). Depending on the used membrane components, solubilization behavior of detergents differ dramatically. Triton X-100 interaction with SM and cholesterol is unfavorable and fully solubilization would need an intensively increased detergent concentration, whereas CHAPS showed equally solubilized lipid micelles containing all applied liposome components (Rodi et al. 2014). Changing the lipids from DMPG/DMPC to DOPC/SM/cholesterol could potentially lead to incomplete solubilization by Triton X-100 resulting in reconstituted protein admittedly, but heterogeneous liposome generation. Incomplete lipid solubilization and possible protein aggregation due to disordering detergent can be additionally reported in this thesis.

Since a homogenous size distribution and functional protein were required for further analysis, other more suitable detergent for integrin reconstitution was chosen. CHAPS has a steroid type chemical structure and protein disaggregating properties. In addition, complete removal is possible due to excessive dialysis, which was not the case for Triton X-100. Hence, reconstitution procedure was changed towards an adapted protocol based on extrusion, to form homogenous size distribution, and dialysis from Coskun et al. (Coskun et al. 2011). Integrin was successfully reconstituted, confirmed by intense integrin bands in a reduced SDS-PAGE after density gradient as well as protein structures in TEM images. Moreover, DLS data shows smaller PDI compared to the preparation with Triton X-100. Different from data with DMPG/DMPC lipids, proteoliposomes are smaller than bare liposomes, which could be due to the fact of variable ionic gradients during dialysis or protein-induced stabilization of lipids. The latter protects proteoliposomes even more from vesicle fusion compared to bare liposomes (Miller and Dahl 1982; Crommelin et al. 1986).

Biological membranes generate highly dynamic structures that are sterol- and sphingolipid-enriched ordered assemblies characterized by specific proteins, called lipid rafts. In the nanoscale, raft assembly is created by tightly packing of cholesterol and saturated acyl chains leading to a thickening and stiffening of the membrane segment. For artificial model membranes these phases can be separated in i) liquid-ordered (Lo) phase, containing highly dense saturated lipids and cholesterol, and ii) liquid-disordered (Ld) phase, comprising of mainly unsaturated lipids in disordered state (Kaiser et al. 2009; Simons and Sampaio 2011). Therefore, different ratios of DOPC, SM and cholesterol were utilized to mimic liquid-ordered and liquid disordered phases and even raft domains of membranes.

High cholesterol content leads to less integrin reconstitution which could have two potential reasons: firstly, integrin αIIbβ3 does not favor highly ordered phases, which was already published in studies of blood platelets, showing indeed important role in αIIbβ3-dependent upregulation of microdomains upon platelet stimulation but only minor detection of integrin inside rafts of activated platelets (Bodin et al. 2005; Wonerow et al. 2002). Interestingly, other integrins such as LFA-1 and α4β1 are mobilized upon activation to the lipid rafts (Leitinger and Hogg 2002).

Secondly, high cholesterol content leads to a shift in CMC for liposomes solubilization (Rodi et al. 2014; Schürholz 1996), resulting in less solubilized membrane and less reconstituted integrin, consequently. Hence, high cholesterol content of liposomes impedes the successful reconstitution of αIIbβ3, without potential increase of detergent concentration. Generally, making a protein “raftophilic” is a topic that is still unclear, although studies indicate the important role of palmytoilation as well as properties of the proteins, e.g. glycosyl phosphatidyl inositol- anchors (Simons and Sampaio 2011).

Nonetheless, DLS data of the liposomes consisting different ratios of DOPC, SM and cholesterol reveal decreasing size with increasing amounts of DOPC content, whereas PDI values increase dramatically. For highly cholesterol packed liposomes the opposite trend is apparent, which is summarized in Figure 43.

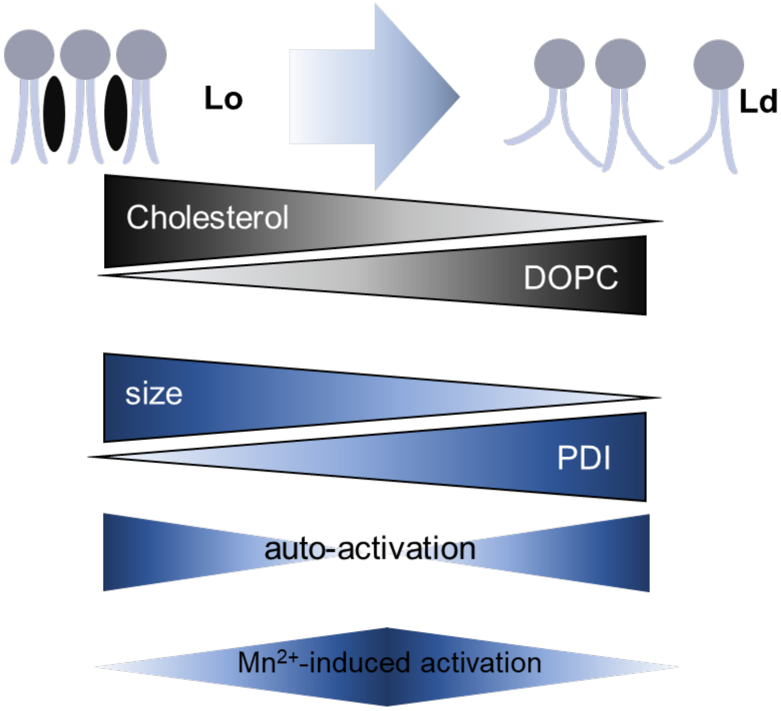

Figure 43: Schematic summary of the effect of various lipidic systems on αIIbβ3 activation. Lipid systems varying in liquid-ordered (Lo) and liquid-disordered (Ld) phases.

Interestingly, DOPC is set as an inverted cone shaped lipid (Simons and Sampaio 2011), prominently forming lamellar structures (Nagle and Tristram-Nagle 2000), that are not as dense as bilayers consisting of unsaturated PC lipids (Costigan et al. 2000), but shows tendency to form smaller liposomes compared to liposomes consisting of saturated lipids in this thesis. Possible explanations could be i) the presence of cholesterol, that destabilizes at specific concentrations, the DOPC bilayer by reductions of the packing stress, ii) due to the fact that DOPC is able to form hexagonal phases of large dimensions (Chen and Rand 1997), and/or iii) pressure induced by the various shapes of protein transmembrane domains (Koller and Lohner 2014), leading to higher curvature, heterogeneous size distribution and smaller liposomes, consequently. Additionally, high SM and cholesterol content causes highly packed lipid phases that stabilize lamellar bilayer structures (Shipley et al. 1974), which could explain the high size of SM- and cholesterol-enriched liposomes.

Taking into account also the potential of activating the integrin αIIbβ3 receptor in a lipid bilayer comprising varying ratios ranging from liquid-ordered (DOPC:SM:cholesterol 25:35:40) to disordered phases (70:25:5), it appears that highly disordered phases (70:25:5 and 60:28:12) already lead to partial activation of αIIbβ3. This activation level could not be increased by Mn^{2+} treatment, whereas high amount of cholesterol, thus ordered phases, lead to even vanishingly low activation. The latter could be also explainable by the fact of only minor integrin reconstitution success indicated by the SDS-PAGE. Interestingly, a mixture of both phases (45:30:25) showed less auto-activated integrin under physiological conditions but high activation after Mn^{2+} incubation, which confirms previous studies (Campbell and Humphries

2011; Zhang and Chen 2012). Even small rise of the saturation of the hydrocarbon chains by increasing amounts of SM (37.5:37.5:25) or usage of originally appointed DMPG:DMPC liposomes, lead to partial integrin extension without additional induction of activation by divalent cations. In contrast to samples with highly ordered phases, these lipid ratios could be still shifted towards activated integrin upon Mn^{2+} injection (Figure 43).

Summarized, high content of cholesterol potentially diminishes integrin reconstitution and does not favor integrin activation. Nonetheless, high content of liquid-disordered phases, formed by DOPC, facilitates high unspecific integrin activation. Even small increasements of saturated lipids, related to liquid-ordered phase, show also unspecific integrin activation. However, integrin ectodomain extension upon Mn^{2+} treatment is still feasible. Lowest unspecific activation but specific activated integrin by divalent cations represents the “balanced course” DOPC:SM:cholesterol ratio 45:30:25. Given these findings, the lipid environment and its flexibility *versus* rigidity likely play an essential role in receptor regulation and downstream signaling upon platelet aggregation.

5.6. Impact of integrin on cell elasticity and cytoskeleton

Platelet activation and aggregation includes, beyond the influence of lipids and ligands, structural changes and rearrangements of the actin cytoskeleton, which is mediated mainly by the mechanical sensors, namely integrins. Thus, understanding the mechanisms behind integrin activation, the cytoskeleton needs to be considered. Biomimetic minimal systems, such as liposomes, are not efficiently mimicking the highly complex actin machinery behind the integrin dynamics. Therefore, an expression platform was created using HEK293 cells, which are widely used as stable human derived cells for transfection (Graham et al. 1977).

Integrin wildtype (WT) was expressed and additionally mutated protein expressing cells were synthesized, that contain mutations to either keep the integrin constantly active or constantly inactive. The inactivated mutant, causing a Glanzmann thrombasthenia-like phenotype, results from a disulfide-bridge linking the integrin head to the leg domains, which should lock the protein in the bent conformation (Takagi et al. 2002). While, point mutation of cysteine to arginine in the β3-head keeps the integrin in an extended conformation, by disruption of a disulfide bridge (Ruiz et al. 2001). Co-localization in all four cell lines was confirmed successfully by flow cytometry measurements and confocal microscopy images.

The cytoskeletal network is closely related to the membrane *via* its interaction with integrins (Durrant et al. 2017). Upon activation of integrins, actin arrangements change, which is basically the initiator for shape change and adhesion of cells to a substrate or other cells (Bearer et al. 2002). The cell elasticity is mainly dependent on the cytoskeleton; therefore, it serves as an indicator for the processes within the cytoskeletal machinery by certain triggers (Gavara and Chadwick 2016). Expression alone or even external induction of integrin αIIbβ3 activation potentially leads to changes in cell mechanics indicating variations in actin filamentous distribution.

First, integrin extension caused by Mn^{2+} was studied in flow cytometer measurements by binding of the active conformation-specific antibody PAC-1. Mn^{2+} shifts the equilibrium towards the active conformation, which is observable in all integrin-expressing cells, especially in the active mutant-expressing cells. Although constant active conformation was expected for the active mutant under both untreated and Mn^{2+}-treated conditions, Mn^{2+} increases the activation dramatically. Probably, mutations induce integrin extension but the head domain is not entirely directed towards the extracellular space, making the PAC-1 binding site at the interface of both subunits in the head domain not accessible for huge proteins as IgM antibodies. Mn^{2+} binds the cation binding sites (e.g. MIDAS) and directs the αIIbβ3 head even more upright (Tiwari et al. 2011; Zhang and Chen 2012), which could clarify the increased activation signal in the flow cytometer.

Surprisingly, also inactive mutant-expressing cells show activation levels similar to the WT integrin, although completely loss of PAC-1 binding would be expected. Disulfide linkers between head and leg domains of the αIIbβ3, that should keep the integrin in the bent conformation, might be not formed for every protein, leading to partial expression of flexible integrin that is able to extend. However, active mutant cells express high amounts of extended integrin, whereas WT shows less and inactive integrin expressing cells even lower Mn^{2+}-induced activation, basically. The chelator EDTA, which captures divalent cations (Oviedo and Rodríguez 2003), leads in turn to no activation detection at all cell lines indicating again the importance of divalent ions for protein stability and activation, even for constitutively active integrin (Zhang and Chen 2012).

Integrins build a bridge between adhesion sites and the actin filaments, which raises the question whether actin rearrangements due to integrin activation result in cell elasticity differences. Initially, actin filaments, as well as the β3-subunit, were imaged in confocal microscopy and additionally treated with Mn^{2+} to induce activation. Interestingly, already integrin expression alone, leads to F-actin recruitment to the membrane, specifically to the interfaces of two cells, leading to a co-localization of integrin and actin filaments. Especially at the cell periphery, the actin network forms lamellipodia-like structures, which favors adhesion contacts and serves as mechano-sensor (Oakes et al. 2018). Accordingly, integrin expression results in actin recruitment and augmented development of lamellipodia, which was also observed for other integrins (Guillou et al. 2008; Pinco et al. 2002).

Upon manganese treatment, all cells intensify lamellipodia characteristics and induce additional filopodia extensions indicating increased actin polymerization and induction of migration and development of cell-cell interactions. Albeit, integrin expressing cells show even higher accumulations of lamellipodia and filopodia compared to control. Additionally, small dot-shaped F-actin structures accumulate inside the cells indicating rearrangement of F-actin (Haghparast et al. 2015). PAC-1 antibody is most of all constructed and advertised for flow cytometry measurements, anyhow, signal was detected as clustered dots at the periphery and edge of Mn^{2+}-treated active integrin mutant expressing cells in confocal microscopy images. Confirming the results of the flow cytometry activation, Mn^{2+} treatment supported active integrin conformation. Moreover, the integrin conformation alone seems to play only a minor role, while presence of integrin affects indeed cytoskeletal rearrangements (Pinco et al. 2002). Treatment with Mn^{2+} intensifies the described effect compared to control cells, but could have already minor side effects independently from the integrin expression, such as oxidative stress introduction in mitochondria (Smith et al. 2017) and interaction with cation binding sites at the filaments to drive actin polymerization (Kang et al. 2012).

The actin rearrangements observed in confocal microscopy are potentially associated with differences in cell elasticity, which was studied for adherent cells in AFM and suspended cell in RT-DC.

Generally, cells in suspension are characterized by an isotropic actin cytoskeleton and an actin cortex, which is a network underlying the membrane provoking cortical stiffness (Schwarz and Safran 2013). In contrast, adherent cells comprising of an anisotropic actin distribution consisting of additional subsystems, namely lamellipodia, that pushes outwards against the membrane and contractile actin filaments forming stress fibers. These areas are sides of adhesion, which are anchored to the receptor connecting them to the ECM, which is displayed also in presented confocal images. The ventral and dorsal stress fibers are flexible, whereas upon adhesion tension is developed leading to force sensing and spreading, consequently (Schwarz and Safran 2013).

Difference between suspension and adherent cells mirrors in dramatically differences in cell stiffness, which is displayed in the presented results by high YM in the suspension, but lower YM in adherent cells. This was already observed for HEK293 cells in other studies (Haghparast et al. 2015; Haghparast et al. 2013). While integrin expression has no significant effect on elasticity for cells in suspension (RT-DC), adherent integrin expressing cells in AFM show significantly softer cells. The difference is not surprising, due to integrins main function as adhesion receptor connecting ECM and cytoskeleton (Schwarz and Safran 2013; Campbell and Humphries 2011).

In adherent cells, ventral stress fibers as well as lamellipodia in the cell periphery promote adhesion contacts to the substrate at the adhesion sites. Actin reorganization concentrate on the ventral site, whereas AFM measurements are taken from the dorsal site of the cells. Therefore, AFM results have to be interpreted carefully, since elasticity changes across the cell. Potential recruitment of actin to the adhesion sites, especially in integrin WT and active mutant expressing cells (Oakes et al. 2018; Schwarz and Safran 2013), could lead to softer cell surface in AFM compared to control cells as well as inactive mutant expressing cells. Furthermore, the adhesion area is highly active and actin polymerization forces modulate the integrin-ECM connection leading to increased integrin density and initiation of integrin clustering. Consequently, adhesions sites and cell spreading are stabilized, whose elastic characteristics depend strongly on the type of integrin (Pinco et al. 2002; Lange et al. 2016; Lacaria et al. 2020).

This process can be forced in especially WT integrin expressing cells by induction of integrin active state by Mn^{2+} ions (Zhang and Chen 2012). Interestingly, WT- and active mutant expressing cells become stiffer in AFM upon incubation with Mn^{2+}, which could be explained by stronger attachment and spreading mediated by increased integrin clustering among the whole cell (Zhang and Chen 2012; Gingras et al. 2013; Oakes et al. 2018). This effect is not present in suspended cells in RT-DC, confirming the fact of the high importance of adhesion interfaces in cell mechanical behavior. The cells expressing inactive integrin, and the control cells without any integrin, show comparable effects in both complemental methods.

However, Mn^{2+} treatment leads to higher elasticity for i) all cell lines in RT-DC and ii) for control and inactive mutant expressing cells in AFM, although studies of Lange et al. (Lange et al. 2016) show stiffer cells upon Mn^{2+} treatment. Other factors could affect the cell mechanics upon ion incubation, such as divalent ion interaction with the lipid bilayers by different binding behavior to lipid headgroups (Binder and Zschörnig 2002) or induction of cellular processes e.g. apoptosis through caspase activation and ER stress within the cell (Smith et al. 2017).

Contrary results indicating already the highly complex network and interplay of different factors ranging from cell type, membrane composition, adhesion sites, actin polymerization (Scipion et al. 2018), integrin expression and its activation state (Lickert et al. 2018). Finally, divalent ions play a major role in integrin stability and activation as well as plenty cellular processes, which emerges in samples treated with EDTA (Tiwari et al. 2011; Chaigne-Delalande and Lenardo 2014; Bashford et al. 1988; Gingell et al. 1970), that captures all divalent ions: cortical stiffness increases significantly in all cell lines in RT-DC.

Apparently, mutations influencing the activation state of αIIbβ3 (as in Glanzmann thrombasthenia), have a drastic effect on cell mechanics and actin reorganization which in turn, controls the platelet performance upon clot formation in hemostasis. The discussed results reveal the radical differences whether cells are in suspension thus, circulating in the blood, or adhere to substrates such as sites of injury and exposed ECM.

5.7. Summary and perspectives

The integrin αIIbβ3 fulfill plenty of functions and is major part in several cell processes. Ranging from adhesion to activation of various signaling pathways, αIIbβ3 affects cellular shape up to platelet survival and platelet death. Disease mediated by the receptor αIIbβ3 are based on incorrect αIIbβ3 expression, structural and functional abnormalities and dysregulated immune response, among others. Many external factors can influence the transmembrane protein stability and its conformation. Moreover, highly reactive platelets can be triggered already by small stimuli, which makes studies on αIIbβ3 extremely delicate.

Therefore, the development of biomimetic systems advanced upon the last decades, which enables to focus on simplified networks for understanding of transmembrane protein function (e.g. liposomes, nanodiscs and lipid bilayers). Results in this study reveal the importance of divalent ions, especially Mn^{2+} and Ca^{2+}, for integrin activation with receptor reconstituted into liposomes. However, also the clinically relevant drugs heparin and quinine are found to interact with αIIbβ3 and affect its conformation. Furthermore, biomedical applications, such as maghemite NPs, can be tested for interaction with artificial platelet membranes. Since not only ligands and interaction partners are capable for integrin alterations, also lipidic environment can be controlled in the introduced membrane systems. Hence, integrins associate with several other important molecules that play a crucial role in surveillance of integrins but also essential downstream events.

To mimic the highly complex system *in vivo*, a HEK293 cell based-expression platform was generated, which enables the genetic modification of the integrin as well as the consideration of the influence of cellular proteins, such as actin. The analyses of mutated integrins, exhibit the consequential role of actin rearrangements due to αIIbβ3 activation. For this reason, also the mechanical properties of cells change, albeit the cell status, whether its adherent or in suspension, has a significant collateral impact on the cell elasticity.

The biophysical tools combined with the established biomimetic systems in this thesis, enable the analysis of receptors, such as αIIbβ3, to elucidate associated disease mechanisms, study induction of immunogenicity, reveal the importance of varying lipidic environment and the connection between adhesions sites and cellular actin network. The findings contribute to the development of diagnostic tools and treatment strategies against certain diseases, e.g. autoantibody induction by integrin neoepitopes in ITP or targeted drug delivery systems.

6. List of figures

7. List of tables

8. References

Adair, B. D., Xiong, J.-P., Maddock, C., Goodman, S. L., Arnaout, M. A. and Yeager, M. (2005). Three-dimensional EM structure of the ectodomain of integrin alphaVbeta3 in a complex with fibronectin. *The Journal of cell biology* **168**, 1109–1118.

Adair, B. D. and Yeager, M. (2002). Three-dimensional model of the human platelet integrin alpha IIbbeta 3 based on electron cryomicroscopy and x-ray crystallography. *Proceedings of the National Academy of Sciences of the United States of America* **99**, 14059–14064.

Alsop, R. J., Maria Schober, R. and Rheinstädter, M. C. (2016). Swelling of phospholipid membranes by divalent metal ions depends on the location of the ions in the bilayers. *Soft matter* **12**, 6737–6748.

Audia, S., Mahévas, M., Samson, M., Godeau, B. and Bonnotte, B. (2017). Pathogenesis of immune thrombocytopenia. *Autoimmunity reviews* **16**, 620–632.

Auría-Soro, C., Nesma, T., Juanes-Velasco, P., Landeira-Viñuela, A., Fidalgo-Gomez, H., Acebes-Fernandez, V., Gongora, R., Almendral Parra, M. J., Manzano-Roman, R. and Fuentes, M. (2019). Interactions of Nanoparticles and Biosystems: Microenvironment of Nanoparticles and Biomolecules in Nanomedicine. *Nanomaterials (Basel, Switzerland)* **9**.

Baird, J. A., Olayo-Valles, R., Rinaldi, C. and Taylor, L. S. (2010). Effect of molecular weight, temperature, and additives on the moisture sorption properties of polyethylene glycol. *Journal of pharmaceutical sciences* **99**, 154–168.

Ballut, L., Sapay, N., Chautard, E., Imberty, A. and Ricard-Blum, S. (2013). Mapping of heparin/heparan sulfate binding sites on αvβ3 integrin by molecular docking. *Journal of molecular recognition: JMR* **26**, 76–85.

Bashford, C. L., Alder, G. M., Graham, J. M., Menestrina, G. and Pasternak, C. A. (1988). Ion modulation of membrane permeability: effect of cations on intact cells and on cells and phospholipid bilayers treated with pore-forming agents. *The Journal of membrane biology* **103**, 79–94.

Bearer, E. L., Prakash, J. M. and Li, Z. (2002). Actin dynamics in platelets. *International review of cytology* **217**, 137–182.

Beglova, N., Blacklow, S. C., Takagi, J. and Springer, T. A. (2002). Cysteine-rich module structure reveals a fulcrum for integrin rearrangement upon activation. *Nature structural biology* **9**, 282–287.

Beltrán-Gracia, E., López-Camacho, A., Higuera-Ciapara, I., Velázquez-Fernández, J. B. and Vallejo-Cardona, A. A. (2019). Nanomedicine review: clinical developments in liposomal applications. *Cancer Nano* **10**, 1175.

Bennett, J. S. (2005). Structure and function of the platelet integrin alphaIIbbeta3. *The Journal of clinical investigation* **115**, 3363–3369.

Berg, J. M., Tymoczko, J. L. and Stryer, L. (2002). *Biochemistry*. New York, [Bethesda, MD]: W.H. Freeman; NCBI.

Bhattacharjee, S. (2016). DLS and zeta potential - What they are and what they are not? *Journal of controlled release: official journal of the Controlled Release Society* **235**, 337–351.

Bhoria, P., Sharma, S., Varma, N., Malhotra, P., Varma, S. and Luthra-Guptasarma, M. (2015). Effect of steroids on the activation status of platelets in patients with Immune thrombocytopenia (ITP). *Platelets* **26**, 119–126.

Bidone, T. C., Polley, A., Durumeric, A., Driscoll, T., Iwamoto, D., Calderwood, D., Schwartz, M. A. and Voth, G. A. (2017). *New Insights into the Conformational Activation of Full-Length Integrin*.

Binder, H. and Zschörnig, O. (2002). The effect of metal cations on the phase behavior and hydration characteristics of phospholipid membranes. *Chemistry and Physics of Lipids* **115**, 39–61.

Bligh, E. G. and Dyer, W. J. (1959). A rapid method of total lipid extraction and purification. *Can. J. Biochem. Physiol.* **37**, 911–917.

Bodin, S., Soulet, C., Tronchère, H., Sié, P., Gachet, C., Plantavid, M. and Payrastre, B. (2005). Integrin-dependent interaction of lipid rafts with the actin cytoskeleton in activated human platelets. *Journal of cell science* **118**, 759–769.

Bougie, D. W., Peterson, J., Rasmussen, M. and Aster, R. H. (2015). Mechanism of quinine-dependent monoclonal antibody binding to platelet glycoprotein IIb/IIIa. *Blood* **126**, 2146–2152.

Bougie, D. W., Wilker, P. R. and Aster, R. H. (2006). Patients with quinine-induced immune thrombocytopenia have both “drug-dependent” and “drug-specific” antibodies. *Blood* **108**, 922–927.

Bozzuto, G. and Molinari, A. (2015). Liposomes as nanomedical devices. *International journal of nanomedicine* **10**, 975–999.

Brügger, B. (2014). Lipidomics: analysis of the lipid composition of cells and subcellular organelles by electrospray ionization mass spectrometry. *Annual review of biochemistry* **83**, 79–98.

Burridge, K. and Wittchen, E. S. (2013). The tension mounts: stress fibers as force-generating mechanotransducers. *The Journal of cell biology* **200**, 9–19.

Butt, H.-J., Cappella, B. and Kappl, M. (2005). Force measurements with the atomic force microscope: Technique, interpretation and applications. *Surface Science Reports* **59**, 1–152.

Campbell, I. D. and Humphries, M. J. (2011). Integrin structure, activation, and interactions. *Cold Spring Harbor perspectives in biology* **3**.

Canet-Ferrer, J., Coronado, E., Forment-Aliaga, A. and Pinilla-Cienfuegos, E. (2014). Correction of the tip convolution effects in the imaging of nanostructures studied through scanning force microscopy. *Nanotechnology* **25**, 395703.

Chaigne-Delalande, B. and Lenardo, M. J. (2014). Divalent cation signaling in immune cells. *Trends in immunology* **35**, 332–344.

Chen, Z. and Rand, R. P. (1997). The influence of cholesterol on phospholipid membrane curvature and bending elasticity. *Biophysical Journal* **73**, 267–276.

Cho, N.-J., Cheong, K. H., Lee, C., Frank, C. W. and Glenn, J. S. (2007a). Binding dynamics of hepatitis C virus' NS5A amphipathic peptide to cell and model membranes. *Journal of virology* **81**, 6682–6689.

Cho, N.-J., Cho, S.-J., Cheong, K. H., Glenn, J. S. and Frank, C. W. (2007b). Employing an amphipathic viral peptide to create a lipid bilayer on Au and TiO2. *Journal of the American Chemical Society* **129**, 10050–10051.

Choi, W.-S., Rice, W. J., Stokes, D. L. and Coller, B. S. (2013). Three-dimensional reconstruction of intact human integrin αIIbβ3: new implications for activation-dependent ligand binding. *Blood* **122**, 4165–4171.

Ciancaglini, P., Simão, A. M. S., Bolean, M., Millán, J. L., Rigos, C. F., Yoneda, J. S., Colhone, M. C. and Stabeli, R. G. (2012). Proteoliposomes in nanobiotechnology. *Biophysical reviews* **4**, 67–81.

Cines, D. B., Liebman, H. and Stasi, R. (2009). Pathobiology of secondary immune thrombocytopenia. *Seminars in hematology* **46**, S2-14.

Coskun, Ü., Grzybek, M., Drechsel, D. and Simons, K. (2011). Regulation of human EGF receptor by lipids. *Proceedings of the National Academy of Sciences of the United States of America* **108**, 9044–9048.

Costigan, S.C., Booth, P.J. and Templer, R.H. (2000). Estimations of lipid bilayer geometry in fluid lamellar phases. *Biochimica et Biophysica Acta (BBA) - Biomembranes* **1468**, 41–54.

Crommelin, D. J. A., Fransen, G. J. and Salemink, P. J. M. (1986). Stability of Liposomes on Storage. In *Targeting of Drugs With Synthetic Systems* (ed. G. Gregoriadis, J. Senior and G. Poste), pp. 277–287. Boston, MA: Springer US.

Cronan, J. E. and Thomas, J. (2009). Chapter 17 Bacterial Fatty Acid Synthesis and its Relationships with Polyketide Synthetic Pathways. In *Complex Enzymes in Microbial Natural Product Biosynthesis, Part B: Polyketides, Aminocoumarins and Carbohydrates*, pp. 395–433: Elsevier.

Dai, A., Ye, F., Taylor, D. W., Hu, G., Ginsberg, M. H. and Taylor, K. A. (2015). The Structure of a Full-length Membrane-embedded Integrin Bound to a Physiological Ligand. *The Journal of biological chemistry* **290**, 27168–27175.

Davydov, D. R., Fernando, H., Baas, B. J., Sligar, S. G. and Halpert, J. R. (2005). Kinetics of dithionite-dependent reduction of cytochrome P450 3A4: heterogeneity of the enzyme caused by its oligomerization. *Biochemistry* **44**, 13902–13913.

Di Silvio, D., Maccarini, M., Parker, R., Mackie, A., Fragneto, G. and Baldelli Bombelli, F. (2017). The effect of the protein corona on the interaction between nanoparticles and lipid bilayers. *Journal of colloid and interface science* **504**, 741–750.

Diaspro, A., ed. (2002). *Confocal and two-photon microscopy: foundations, applications, and advances*: Wiley-Liss. New York.

Dickey, A. and Faller, R. (2008). Examining the contributions of lipid shape and headgroup charge on bilayer behavior. *Biophysical Journal* **95**, 2636–2646.

Dimova, R. (2019). Giant Vesicles and Their Use in Assays for Assessing Membrane Phase State, Curvature, Mechanics, and Electrical Properties. *Annual review of biophysics* **48**, 93–119.

Dixon, M. C. (2008). Quartz Crystal Microbalance with Dissipation Monitoring: Enabling Real-Time Characterization of Biological Materials and Their Interactions. *Journal of Biomolecular Techniques : JBT* **19**, 151–158.

Durrant, T. N., van den Bosch, M. T. and Hers, I. (2017). Integrin αIIbβ3 outside-in signaling. *Blood* **130**, 1607–1619.

Erb, E. M. and Engel, J. (2000). Reconstitution of functional integrin into phospholipid vesicles and planar lipid bilayers. *Methods in molecular biology (Clifton, N.J.)* **139**, 71–82.

Errante, P. R. (2016). Flow cytometry: a literature review. *Journal of Biological and Medical sciences.* **2**, 221.

Fairbanks, M. B., Pollock, J. R., Prairie, M. D., Scahill, T. A., Baczynskyj, L., Heinrikson, R. L. and Stockman, B. J. (1995). Purification and structural characterization of the CD11b/CD18 integrin alpha subunit I domain reveals a folded conformation in solution. *FEBS letters* **369**, 197–201.

Fröhlich, E. (2016). Action of Nanoparticles on Platelet Activation and Plasmatic Coagulation. *Current medicinal chemistry* **23**, 408–430.

Frohnmayer, J. P., Brüggemann, D., Eberhard, C., Neubauer, S., Mollenhauer, C., Boehm, H., Kessler, H., Geiger, B. and Spatz, J. P. (2015). Minimal synthetic cells to study integrin-mediated adhesion. *Angewandte Chemie (International ed. in English)* **54**, 12472–12478.

Fuchs, B., Süss, R., Teuber, K., Eibisch, M. and Schiller, J. (2011). Lipid analysis by thin-layer chromatography—a review of the current state. *Journal of chromatography. A* **1218**, 2754–2774.

Furrer, J., Luy, B., Basrur, V., Roberts, D. D. and Barchi, J. J. (2006). Conformational analysis of an alpha3beta1 integrin-binding peptide from thrombospondin-1: implications for antiangiogenic drug design. *Journal of medicinal chemistry* **49**, 6324–6333.

Gahmberg, C. G., Fagerholm, S. C., Nurmi, S. M., Chavakis, T., Marchesan, S. and Grönholm, M. (2009). Regulation of integrin activity and signalling. *Biochimica et biophysica acta* **1790**, 431–444.

Gao, C., Boylan, B., Fang, J., Wilcox, D. A., Newman, D. K. and Newman, P. J. (2011). Heparin promotes platelet responsiveness by potentiating αIIbβ3-mediated outside-in signaling. *Blood* **117**, 4946–4952.

Gasteiger, E., Gattiker, A., Hoogland, C., Ivanyi, I., Appel, R. D. and Bairoch, A. (2003). ExPASy: The proteomics server for in-depth protein knowledge and analysis. *Nucleic acids research* **31**, 3784–3788.

Gavara, N. and Chadwick, R. S. (2016). Relationship between cell stiffness and stress fiber amount, assessed by simultaneous atomic force microscopy and live-cell fluorescence imaging. *Biomechanics and modeling in mechanobiology* **15**, 511–523.

Ge, Y., Gao, J., Jordan, R. and Naumann, C. A. (2018). Changes in Cholesterol Level Alter Integrin Sequestration in Raft-Mimicking Lipid Mixtures. *Biophysical Journal* **114**, 158–167.

Geiger, B., Bershadsky, A., Pankov, R. and Yamada, K. M. (2001). Transmembrane crosstalk between the extracellular matrix—cytoskeleton crosstalk. *Nature reviews. Molecular cell biology* **2**, 793–805.

Ghoshal, K. and Bhattacharyya, M. (2014). Overview of platelet physiology: its hemostatic and nonhemostatic role in disease pathogenesis. *The Scientific World Journal* **2014**, 781857.

Gianazza, E., Brioschi, M., Baetta, R., Mallia, A., Banfi, C. and Tremoli, E. (2020). Platelets in Healthy and Disease States: From Biomarkers Discovery to Drug Targets Identification by Proteomics. *International Journal of Molecular Sciences* **21**.

Gingell, D., Garrod, D. R. and Palmer, J. F. (1970). Divalent Cations and Cell Adhesion. In *A Symposium on Calcium and Cellular Function* (ed. A. W. Cuthbert), pp. 59–64. London: Palgrave Macmillan UK.

Gingras, A. R., Ye, F. and Ginsberg, M. H. (2013). Reconstructing integrin activation in vitro. *Methods in molecular biology (Clifton, N.J.)* **1046**, 1–17.

Giuliodori, M. J., Lujan, H. L., Briggs, W. S., Palani, G. and DiCarlo, S. E. (2009). Hooke's law: applications of a recurring principle. *Advances in physiology education* **33**, 293–296.

Goksu, E. I., Vanegas, J. M., Blanchette, C. D., Lin, W.-C. and Longo, M. L. (2009). AFM for structure and dynamics of biomembranes. *Biochimica et biophysica acta* **1788**, 254–266.

Gorter, E. and Grendel, F. (1925). On biomolecular layers of lipoids on the chromocytes of the blood. *The Journal of experimental medicine* **41**, 439–443.

Gossett, D. R., Tse, H. T. K., Lee, S. A., Ying, Y., Lindgren, A. G., Yang, O. O., Rao, J., Clark, A. T. and Di Carlo, D. (2012). Hydrodynamic stretching of single cells for large population mechanical phenotyping. *Proceedings of the National Academy of Sciences of the United States of America* **109**, 7630–7635.

Graham, F. L., Smiley, J., Russell, W. C. and Nairn, R. (1977). Characteristics of a human cell line transformed by DNA from human adenovirus type 5. *The Journal of general virology* **36**, 59–74.

Guildford, A. L., Poletti, T., Osbourne, L. H., Di Cerbo, A., Gatti, A. M. and Santin, M. (2009). Nanoparticles of a different source induce different patterns of activation in key biochemical and cellular components of the host response. *Journal of the Royal Society, Interface* **6**, 1213–1221.

Guillou, H., Depraz-Depland, A., Planus, E., Vianay, B., Chaussy, J., Grichine, A., Albigès-Rizo, C. and Block, M. R. (2008). Lamellipodia nucleation by filopodia depends on integrin occupancy and downstream Rac1 signaling. *Experimental cell research* **314**, 478–488.

Gutmann, T., Schäfer, I. B., Poojari, C., Brankatschk, B., Vattulainen, I., Strauss, M. and Coskun, Ü. (2020). Cryo-EM structure of the complete and ligand-saturated insulin receptor ectodomain. *The Journal of cell biology* **219**.

Haghparast, S. M. A., Kihara, T. and Miyake, J. (2015). Distinct mechanical behavior of HEK293 cells in adherent and suspended states. *PeerJ* **3**, e1131.

Haghparast, S. M. A., Kihara, T., Shimizu, Y., Yuba, S. and Miyake, J. (2013). Actin-based biomechanical features of suspended normal and cancer cells. *Journal of bioscience and bioengineering* **116**, 380–385.

Hantgan, R. R., Stahle, M. C. and Lord, S. T. (2010). Dynamic regulation of fibrinogen: integrin αIIbβ3 binding. *Biochemistry* **49**, 9217–9225.

Hardy, G. J., Nayak, R. and Zauscher, S. (2013). Model cell membranes: Techniques to form complex biomimetic supported lipid bilayers via vesicle fusion. *Current Opinion in Colloid & Interface Science* **18**, 448–458.

Hashemzadeh, M., Furukawa, M., Goldsberry, S. and Movahed, M. R. (2008). Chemical structures and mode of action of intravenous glycoprotein IIb/IIIa receptor blockers: A review. *Experimental and clinical cardiology* **13**, 192–197.

Höök, F., Rodahl, M., Brzezinski, P. and Kasemo, B. (1998). Energy Dissipation Kinetics for Protein and Antibody−Antigen Adsorption under Shear Oscillation on a Quartz Crystal Microbalance. *Langmuir* **14**, 729–734.

Huang, J., Li, X., Shi, X., Zhu, M., Wang, J., Huang, S., Huang, X., Wang, H., Li, L., Deng, H. et al. (2019). Platelet integrin αIIbβ3: signal transduction, regulation, and its therapeutic targeting. *Journal of hematology & oncology* **12**, 26.

Hughes, A. L. (2001). Evolution of the integrin alpha and beta protein families. *Journal of molecular evolution* **52**, 63–72.

Hulme, E. C. and Trevethick, M. A. (2010). Ligand binding assays at equilibrium: validation and interpretation. *British journal of pharmacology* **161**, 1219–1237.

Israelachvili, J. N., Mitchell, D. J. and Ninham, B. W. (1976). Theory of self-assembly of hydrocarbon amphiphiles into micelles and bilayers. *J. Chem. Soc., Faraday Trans. 2* **72**, 1525.

Jackman, J., Knoll, W. and Cho, N.-J. (2012). Biotechnology Applications of Tethered Lipid Bilayer Membranes. *Materials* **5**, 2637–2657.

Janke, U., Kulke, M., Buchholz, I., Geist, N., Langel, W. and Delcea, M. (2019). Drug-induced activation of integrin alpha IIb beta 3 leads to minor localized structural changes. *PloS one* **14**, e0214969.

Jing, Y., Trefna, H., Persson, M., Kasemo, B. and Svedhem, S. (2014). Formation of supported lipid bilayers on silica: relation to lipid phase transition temperature and liposome size. *Soft matter* **10**, 187–195.

Johnson, W. C. (1988). Secondary structure of proteins through circular dichroism spectroscopy. *Annual review of biophysics and biophysical chemistry* **17**, 145–166.

Kaiser, H.-J., Lingwood, D., Levental, I., Sampaio, J. L., Kalvodova, L., Rajendran, L. and Simons, K. (2009). Order of lipid phases in model and plasma membranes. *Proceedings of the National Academy of Sciences of the United States of America* **106**, 16645–16650.

Kamata, T., Handa, M., Sato, Y., Ikeda, Y. and Aiso, S. (2005). Membrane-proximal alpha/beta stalk interactions differentially regulate integrin activation. *The Journal of biological chemistry* **280**, 24775–24783.

Kang, H., Bradley, M. J., McCullough, B. R., Pierre, A., Grintsevich, E. E., Reisler, E. and La Cruz, E. M. de (2012). Identification of cation-binding sites on actin that drive polymerization and modulate bending stiffness. *Proceedings of the National Academy of Sciences of the United States of America* **109**, 16923–16927.

Kattula, S., Byrnes, J. R. and Wolberg, A. S. (2017). Fibrinogen and Fibrin in Hemostasis and Thrombosis. *Arteriosclerosis, thrombosis, and vascular biology* **37**, e13-e21.

Kelly, S. M., Jess, T. J. and Price, N. C. (2005). How to study proteins by circular dichroism. *Biochimica et biophysica acta* **1751**, 119–139.

Khan, I., Saeed, K. and Khan, I. (2019). Nanoparticles: Properties, applications and toxicities. *Arabian Journal of Chemistry* **12**, 908–931.

Kim, C., Ye, F. and Ginsberg, M. H. (2011). Regulation of integrin activation. *Annual review of cell and developmental biology* **27**, 321–345.

Koller, D. and Lohner, K. (2014). The role of spontaneous lipid curvature in the interaction of interfacially active peptides with membranes. *Biochimica et biophysica acta* **1838**, 2250–2259.

Kraft, J. C., Freeling, J. P., Wang, Z. and Ho, R. J. Y. (2014). Emerging research and clinical development trends of liposome and lipid nanoparticle drug delivery systems. *Journal of pharmaceutical sciences* **103**, 29–52.

Kreimann, M., Brandt, S., Krauel, K., Block, S., Helm, C. A., Weitschies, W., Greinacher, A. and Delcea, M. (2014). Binding of anti-platelet factor 4/heparin antibodies depends on the thermodynamics of conformational changes in platelet factor 4. *Blood* **124**, 2442–2449.

Krieg, M., Fläschner, G., Alsteens, D., Gaub, B. M., Roos, W. H., Wuite, G. J. L., Gaub, H. E., Gerber, C., Dufrêne, Y. F. and Müller, D. J. (2019). Atomic force microscopy-based mechanobiology. *Nat Rev Phys* **1**, 41–57.

Krishnegowda, M. and Rajashekaraiah, V. (2015). Platelet disorders: an overview. *Blood coagulation & fibrinolysis : an international journal in haemostasis and thrombosis* **26**, 479–491.

Ku, T., Lu, P., Chan, C., Wang, T., Lai, S., Lyu, P. and Hsiao, N. (2009). Predicting melting temperature directly from protein sequences. *Computational Biology and Chemistry* **33**, 445–450.

Kulke, M. and Langel, W. (2020). Molecular dynamics simulations to the bidirectional adhesion signaling pathway of integrin αV β3. *Proteins* **88**, 679–688.

Kuznetsova, T. G., Starodubtseva, M. N., Yegorenkov, N. I., Chizhik, S. A. and Zhdanov, R. I. (2007). Atomic force microscopy probing of cell elasticity. *Micron (Oxford, England : 1993)* **38**, 824–833.

Lacaria, L., Lange, J. R., Goldmann, W. H., Rico, F. and Alonso, J. L. (2020). αvβ3 integrin expression increases elasticity in human melanoma cells. *Biochemical and biophysical research communications* **525**, 836–840.

Lam, W. A., Chaudhuri, O., Crow, A., Webster, K. D., Li, T.-D., Kita, A., Huang, J. and Fletcher, D. A. (2011). Mechanics and contraction dynamics of single platelets and implications for clot stiffening. *Nature materials* **10**, 61–66.

Lange, J. R., Goldmann, W. H. and Alonso, J. L. (2016). Influence of αvβ3 integrin on the mechanical properties and the morphology of M21 and K562 cells. *Biochemical and biophysical research communications* **478**, 1280–1285.

Langmuir, I. (1916). The constitution and fundamental properties of solids and liquids. Part I. Solids. *J. Am. Chem. Soc.* **38**, 2221–2295.

Lee, A. G. (2004). How lipids affect the activities of integral membrane proteins. *Biochimica et biophysica acta* **1666**, 62–87.

Lee, A. G. (2011). Biological membranes: the importance of molecular detail. *Trends in biochemical sciences* **36**, 493–500.

Leitinger, B. and Hogg, N. (2002). The involvement of lipid rafts in the regulation of integrin function. *Journal of cell science* **115**, 963–972.

Leitz, A. J., Bayburt, T. H., Barnakov, A. N., Springer, B. A. and Sligar, S. G. (2006). Functional reconstitution of Beta2-adrenergic receptors utilizing self-assembling Nanodisc technology. *BioTechniques* **40**, 601-2, 604, 606, passim.

Lesniak, A., Fenaroli, F., Monopoli, M. P., Åberg, C., Dawson, K. A. and Salvati, A. (2012). Effects of the presence or absence of a protein corona on silica nanoparticle uptake and impact on cells. *ACS nano* **6**, 5845–5857.

Li, R., Babu, C. R., Valentine, K., Lear, J. D., Wand, A. J., Bennett, J. S. and DeGrado, W. F. (2002). Characterization of the monomeric form of the transmembrane and cytoplasmic domains of the integrin beta 3 subunit by NMR spectroscopy. *Biochemistry* **41**, 15618–15624.

Lickert, S., Sorrentino, S., Studt, J.-D., Medalia, O., Vogel, V. and Schoen, I. (2018). Morphometric analysis of spread platelets identifies integrin αIIbβ3-specific contractile phenotype. *Scientific reports* **8**, 5428.

Lind, T. K. and Cárdenas, M. (2016). Understanding the formation of supported lipid bilayers via vesicle fusion-A case that exemplifies the need for the complementary method approach (Review). *Biointerphases* **11**, 20801.

Lind, T. K., Skoda, M. W. A. and Cárdenas, M. (2019). Formation and Characterization of Supported Lipid Bilayers Composed of Phosphatidylethanolamine and Phosphatidylglycerol by Vesicle Fusion, a Simple but Relevant Model for Bacterial Membranes. *ACS omega* **4**, 10687–10694.

Litvinov, R. I., Mekler, A., Shuman, H., Bennett, J. S., Barsegov, V. and Weisel, J. W. (2012). Resolving two-dimensional kinetics of the integrin αIIbβ3-fibrinogen interactions using binding-unbinding correlation spectroscopy. *The Journal of biological chemistry* **287**, 35275–35285.

Ma, Y.-Q., Qin, J. and Plow, E. F. (2007). Platelet integrin alpha(IIb)beta(3): activation mechanisms. *Journal of thrombosis and haemostasis: JTH* **5**, 1345–1352.

Maghsoudy-Louyeh, S., Kropf, M. and Tittmann, B. R. (2018). Review of Progress in Atomic Force Microscopy. *TONIJ* **12**, 86–104.

Mahdavi, M., Ahmad, M. B., Haron, M. J., Namvar, F., Nadi, B., Rahman, M. Z. A. and Amin, J. (2013). Synthesis, surface modification and characterisation of biocompatible magnetic iron oxide nanoparticles for biomedical applications. *Molecules (Basel, Switzerland)* **18**, 7533–7548.

Makogonenko, E. M., Yakubenko, V. P., Ingham, K. C. and Medved, L. V. (1996). Thermal Stability of Individual Domains in Platelet Glycoprotein IIbIIIa. *Eur J Biochem* **237**, 205–211.

Martens, U., Janke, U., Möller, S., Talbot, D., Abou-Hassan, A. and Delcea, M. (2020). Interaction of fibrinogen–magnetic nanoparticle bioconjugates with integrin reconstituted into artificial membranes. *Nanoscale* **41**, 4306.

Marx, K. A. (2003). Quartz crystal microbalance: a useful tool for studying thin polymer films and complex biomolecular systems at the solution-surface interface. *Biomacromolecules* **4**, 1099–1120.

Michelson, A. D., Cattaneo, M., Frelinger, A. L. and Newman, P. J., eds. (2019). *Platelets*: Academic Press, an imprint of Elsevier. London, United Kingdom.

Miles, A. J. and Wallace, B. A. (2016). Circular dichroism spectroscopy of membrane proteins. *Chemical Society reviews* **45**, 4859–4872.

Miller, D. C. and Dahl, G. P. (1982). Early events in calcium-induced liposome fusion. *Biochimica et Biophysica Acta (BBA) - Biomembranes* **689**, 165–169.

Morrison, W. R. (1964). A fast, simple and reliable method for the microdetermination of phosphorus in biological materials. *Analytical Biochemistry* **7**, 218–224.

Múzquiz-Ramos, E. M., Guerrero-Chávez, V., Macías-Martínez, B. I., López-Badillo, C. M. and García-Cerda, L. A. (2015). Synthesis and characterization of maghemite nanoparticles for hyperthermia applications. *Ceramics International* **41**, 397–402.

Nagle, J. F. and Tristram-Nagle, S. (2000). Structure of lipid bilayers. *Biochimica et biophysica acta* **1469**, 159–195.

NanoWizard (2014). Determining the elastic modulus of biological samples using atomic force microscopy. http://www.jpk.com/afm.230.en.html.

Niklasson, M., Andresen, C., Helander, S., Roth, M. G. L., Zimdahl Kahlin, A., Lindqvist Appell, M., Mårtensson, L.-G. and Lundström, P. (2015). Robust and convenient analysis of protein thermal and chemical stability. *Protein science : a publication of the Protein Society* **24**, 2055–2062.

Oakes, P. W., Bidone, T. C., Beckham, Y., Skeeters, A. V., Ramirez-San Juan, G. R., Winter, S. P., Voth, G. A. and Gardel, M. L. (2018). Lamellipodium is a myosin-independent mechanosensor. *Proceedings of the National Academy of Sciences of the United States of America* **115**, 2646–2651.

O'Donnell, V. B., Murphy, R. C. and Watson, S. P. (2014). Platelet lipidomics: modern day perspective on lipid discovery and characterization in platelets. *Circulation research* **114**, 1185–1203.

Oom, A., Poggi, M., Wikström, J. and Sukumar, M. (2012). Surface interactions of monoclonal antibodies characterized by quartz crystal microbalance with dissipation: impact of hydrophobicity and protein self-interactions. *Journal of pharmaceutical sciences* **101**, 519–529.

Otto, O., Rosendahl, P., Mietke, A., Golfier, S., Herold, C., Klaue, D., Girardo, S., Pagliara, S., Ekpenyong, A., Jacobi, A. et al. (2015). Real-time deformability cytometry: on-the-fly cell mechanical phenotyping. *Nature methods* **12**, 199-202, 4 p following 202.

Oviedo, C. and Rodríguez, J. (2003). EDTA: the chelating agent under environmental scrutiny. *Quím. Nova* **26**, 901–905.

Parmar, M. M., Edwards, K. and Madden, T. D. (1999). Incorporation of bacterial membrane proteins into liposomes: factors influencing protein reconstitution. *Biochimica et biophysica acta* **1421**, 77–90.

Pinco, K. A., He, W. and Yang, J. T. (2002). alpha4beta1 integrin regulates lamellipodia protrusion via a focal complex/focal adhesion-independent mechanism. *Molecular biology of the cell* **13**, 3203–3217.

Porcelijn, L., Huiskes, E., Maatman, R., Kreuk, A. de and **Haas, M.** de (2008). Acquired Glanzmann's thrombasthenia caused by glycoprotein IIb/IIIa autoantibodies of the immunoglobulin G1 (IgG1), IgG2 or IgG4 subclass: a study in six cases. *Vox sanguinis* **95**, 324–330.

Prachayasittikul, V., Isarankura-Na-Ayudhya, C., Tantimongcolwat, T., Nantasenamat, C. and Galla, H.-J. (2007). EDTA-induced membrane fluidization and destabilization: biophysical studies on artificial lipid membranes. *Acta biochimica et biophysica Sinica* **39**, 901–913.

Puklin-Faucher, E., Gao, M., Schulten, K. and Vogel, V. (2006). How the headpiece hinge angle is opened: New insights into the dynamics of integrin activation. *The Journal of cell biology* **175**, 349–360.

Richter, R., Mukhopadhyay, A. and Brisson, A. (2003). Pathways of Lipid Vesicle Deposition on Solid Surfaces: A Combined QCM-D and AFM Study. *Biophysical Journal* **85**, 3035–3047.

Richter, R. P., Bérat, R. and Brisson, A. R. (2006). Formation of solid-supported lipid bilayers: an integrated view. *Langmuir* **22**, 3497–3505.

Robertson, J. D. (1959). The ultrastructure of cell membranes and their derivatives. *Biochemical Society symposium* **16**, 3–43.

Rodi, P. M., Bocco Gianello, M. D., Corregido, M. C. and Gennaro, A. M. (2014). Comparative study of the interaction of CHAPS and Triton X-100 with the erythrocyte membrane. *Biochimica et biophysica acta* **1838**, 859–866.

Roe, D. R. and Cheatham, T. E. (2013). PTRAJ and CPPTRAJ: Software for Processing and Analysis of Molecular Dynamics Trajectory Data. *Journal of chemical theory and computation* **9**, 3084–3095.

Rosen, M. J. and Kunjappu, J. T. (2012). *Surfactants and interfacial phenomena*. Hoboken, N.J: Wiley.

Rowley, T. (2012). Flow Cytometry - A Survey and the Basics. Mater Methods **2**.

Ruiz, C., Liu, C. Y., Sun, Q. H., Sigaud-Fiks, M., Fressinaud, E., Muller, J. Y., Nurden, P., Nurden, A. T., Newman, P. J. and Valentin, N. (2001). A point mutation in the cysteine-rich domain of glycoprotein (GP) IIIa results in the expression of a GPIIb-IIIa (alphaIIbbeta3) integrin receptor locked in a high-affinity state and a Glanzmann thrombasthenia-like phenotype. *Blood* **98**, 2432–2441.

Sauerbrey, G. (1959). Verwendung von Schwingquarzen zur Wägung dünner Schichten und zur Mikrowägung. *Z. Physik* **155**, 206–222.

Schürholz, T. (1996). Critical dependence of the solubilization of lipid vesicles by the detergent CHAPS on the lipid composition. Functional reconstitution of the nicotinic acetylcholine receptor into preformed vesicles above the critical micellization concentration. *Biophysical Chemistry* **58**, 87–96.

Schwarz, U. S. and Safran, S. A. (2013). Physics of adherent cells. *Journal of cell science* **85**, 1327–1381.

Scipion, C. P. M., Ghoshdastider, U., Ferrer, F. J., Yuen, T.-Y., Wongsantichon, J. and Robinson, R. C. (2018). Structural evidence for the roles of divalent cations in actin polymerization and activation of ATP hydrolysis. *Proceedings of the National Academy of Sciences of the United States of America* **115**, 10345–10350.

Seddon, A. M., Curnow, P. and Booth, P. J. (2004). Membrane proteins, lipids and detergents: not just a soap opera. *Biochimica et biophysica acta* **1666**, 105–117.

Semple, J. W., Italiano, J. E. and Freedman, J. (2011). Platelets and the immune continuum. *Nature reviews. Immunology* **11**, 264–274.

Senden, T. J. (2001). Force microscopy and surface interactions. *Current Opinion in Colloid & Interface Science* **6**, 95–101.

Shahin, V., Ludwig, Y., Schafer, C., Nikova, D. and Oberleithner, H. (2005). Glucocorticoids remodel nuclear envelope structure and permeability. *Journal of cell science* **118**, 2881–2889.

Shen, H.-H., Lithgow, T. and Martin, L. (2013). Reconstitution of membrane proteins into model membranes: seeking better ways to retain protein activities. *International Journal of Molecular Sciences* **14**, 1589–1607.

Shipley, G. G., Avecilla, L. S. and Small, D. M. (1974). Phase behavior and structure of aqueous dispersions of sphingomyelin. *Journal of lipid research* **15**, 124–131.

Simonian, M. H. (2002). Spectrophotometric Determination of Protein Concentration. *Current Protocols in Food Analytical Chemistry* **4**, B1.3.1-B1.3.7.

Simons, K. and Sampaio, J. L. (2011). Membrane organization and lipid rafts. *Cold Spring Harbor perspectives in biology* **3**, a004697.

Singer, S. J. and Nicolson, G. L. (1972). The fluid mosaic model of the structure of cell membranes. *Science (New York, N.Y.)* **175**, 720–731.

Smith, M. R., Fernandes, J., Go, Y.-M. and Jones, D. P. (2017). Redox dynamics of manganese as a mitochondrial life-death switch. *Biochemical and biophysical research communications* **482**, 388–398.

Smith, P. K., Krohn, R. I., Hermanson, G. T., Mallia, A. K., Gartner, F. H., Provenzano, M. D., Fujimoto, E. K., Goeke, N. M., Olson, B. J. and Klenk, D. C. (1985). Measurement of protein using bicinchoninic acid. *Analytical Biochemistry* **150**, 76–85.

Sobel, M., Fish, W. R., Toma, N., Luo, S., Bird, K., Mori, K., Kusumoto, S., Blystone, S. D. and Suda, Y. (2001). Heparin modulates integrin function in human platelets. *Journal of vascular surgery* **33**, 587–594.

Solh, T., Botsford, A. and Solh, M. (2015). Glanzmann's thrombasthenia: pathogenesis, diagnosis, and current and emerging treatment options. *Journal of blood medicine* **6**, 219–227.

Stetefeld, J., McKenna, S. A. and Patel, T. R. (2016). Dynamic light scattering: a practical guide and applications in biomedical sciences. *Biophysical reviews* **8**, 409–427.

Suk, J. S., Xu, Q., Kim, N., Hanes, J. and Ensign, L. M. (2016). PEGylation as a strategy for improving nanoparticle-based drug and gene delivery. *Advanced drug delivery reviews* **99**, 28–51.

Sun, Z., Costell, M. and Fässler, R. (2019). Integrin activation by talin, kindlin and mechanical forces. *Nature cell biology* **21**, 25–31.

Sunshine, H. and Iruela-Arispe, M. L. (2017). Membrane lipids and cell signaling. *Current opinion in lipidology* **28**, 408–413.

Swinehart, D. F. (1962). The Beer-Lambert Law. *J. Chem. Educ.* **39**, 333.

Takagi, J., Petre, B. M., Walz, T. and Springer, T. A. (2002). Global Conformational Rearrangements in Integrin Extracellular Domains in Outside-In and Inside-Out Signaling. *Cell* **110**, 599–611.

Taub, R., Gould, R. J., Garsky, V. M., Ciccarone, T. M., Hoxie, J., Friedman, P. A. and Shattil, S. J. (1989). A monoclonal antibody against the platelet fibrinogen receptor contains a sequence that mimics a receptor recognition domain in fibrinogen. *The Journal of biological chemistry* **264**, 259–265.

Tiwari, S., Askari, J. A., Humphries, M. J. and Bulleid, N. J. (2011). Divalent cations regulate the folding and activation status of integrins during their intracellular trafficking. *Journal of cell science* **124**, 1672–1680.

Tonda-Turo, C., Carmagnola, I. and Ciardelli, G. (2018). Quartz Crystal Microbalance With Dissipation Monitoring: A Powerful Method to Predict the in vivo Behavior of Bioengineered Surfaces. *Frontiers in bioengineering and biotechnology* **6**, 158.

Versteeg, H. H., Heemskerk, J. W. M., Levi, M. and Reitsma, P. H. (2013). New fundamentals in hemostasis. *Physiological reviews* **93**, 327–358.

Vieira, J. L. F., Borges, L. M. G., Nascimento, M. T. S. and Gomes, A. d. L. S. (2008). Quinine levels in patients with uncomplicated falciparum malaria in the Amazon region of Brazil. *The Brazilian journal of infectious diseases: an official publication of the Brazilian Society of Infectious Diseases* **12**, 353–354.

Vilanova, O., Mittag, J. J., Kelly, P. M., Milani, S., Dawson, K. A., Rädler, J. O. and Franzese, G. (2016). Understanding the Kinetics of Protein-Nanoparticle Corona Formation. *ACS nano* **10**, 10842–10850.

Visentin, G. P. and Liu, C. Y. (2007). Drug-induced thrombocytopenia. *Hematology/oncology clinics of North America* **21**, 685-96, vi.

Vorup-Jensen, T., Chi, L., Gjelstrup, L. C., Jensen, U. B., Jewett, C. A., Xie, C., Shimaoka, M., Linhardt, R. J. and Springer, T. A. (2007). Binding between the integrin alphaXbeta2 (CD11c/CD18) and heparin. *The Journal of biological chemistry* **282**, 30869–30877.

Williams, D. B. and Carter, C. B. (1996). *Transmission Electron Microscopy. A Textbook for Materials Science*. Boston, MA, s.l.: Springer US.

Williams, E. K., Oshinowo, O., Ravindran, A., Lam, W. A. and Myers, D. R. (2019). Feeling the Force: Measurements of Platelet Contraction and Their Diagnostic Implications. *Seminars in thrombosis and hemostasis* **45**, 285–296.

Williamson, P. (2015). Phospholipid Scramblases. *Lipid insights* **8**, 41–44.

Wonerow, P., Obergfell, A., Wilde, J. I., Bobe, R., Asazuma, N., Brdicka, T., Leo, A., Schraven, B., Horejsí, V., Shattil, S. J. et al. (2002). Differential role of glycolipid-enriched membrane domains in glycoprotein VI- and integrin-mediated phospholipase Cgamma2 regulation in platelets. *The Biochemical journal* **364**, 755–765.

Xiao, Z. and Théroux, P. (1998). Platelet activation with unfractionated heparin at therapeutic concentrations and comparisons with a low-molecular-weight heparin and with a direct thrombin inhibitor. *Circulation* **97**, 251–256.

Xiong, J.-P., Stehle, T., Zhang, R., Joachimiak, A., Frech, M., Goodman, S. L. and Arnaout, M. A. (2002). Crystal structure of the extracellular segment of integrin alpha Vbeta3 in complex with an Arg-Gly-Asp ligand. *Science (New York, N.Y.)* **296**, 151–155.

Xu, X.-P., Kim, E., Swift, M., Smith, J. W., Volkmann, N. and Hanein, D. (2016). Three-Dimensional Structures of Full-Length, Membrane-Embedded Human α(IIb)β(3) Integrin Complexes. *Biophysical Journal* **110**, 798–809.

Yagi, M., Murray, J., Strand, K., Blystone, S., Interlandi, G., Suda, Y. and Sobel, M. (2012). Heparin modulates the conformation and signaling of platelet integrin αIIbβ3. *Thrombosis research* **129**, 743–749.

Ye, F., Hu, G., Taylor, D., Ratnikov, B., Bobkov, A. A., McLean, M. A., Sligar, S. G., Taylor, K. A. and Ginsberg, M. H. (2010). Recreation of the terminal events in physiological integrin activation. *The Journal of cell biology* **188**, 157–173.

Ye, F., Kim, C. and Ginsberg, M. H. (2012). Reconstruction of integrin activation. *Blood* **119**, 26–33.

Ye, F., Liu, J., Winkler, H. and Taylor, K. A. (2008). Integrin alpha IIb beta 3 in a membrane environment remains the same height after Mn2+ activation when observed by cryoelectron tomography. *Journal of molecular biology* **378**, 976–986.

Yeagle, P. L. (2016). *The Membranes of Cells*. s.l.: Elsevier Science.

Yun, S.-H., Sim, E.-H., Goh, R.-Y., Park, J.-I. and Han, J.-Y. (2016). Platelet Activation: The Mechanisms and Potential Biomarkers. *BioMed research international* **2016**, 9060143.

Zhang, K. and Chen, J. (2012). The regulation of integrin function by divalent cations. *Cell adhesion & migration* **6**, 20–29.

Zhang, Y., Qiu, Y., Blanchard, A. T., Chang, Y., Brockman, J. M., Ma, V. P.-Y., Lam, W. A. and Salaita, K. (2018). Platelet integrins exhibit anisotropic mechanosensing and harness piconewton forces to mediate platelet aggregation. *Proceedings of the National Academy of Sciences of the United States of America* **115**, 325–330.

Zhao, H. and Lappalainen, P. (2012). A simple guide to biochemical approaches for analyzing protein-lipid interactions. *Molecular biology of the cell* **23**, 2823–2830.

Zhao, J. and Stenzel, M. H. (2018). Entry of nanoparticles into cells: the importance of nanoparticle properties. *Polym. Chem.* **9**, 259–272.

Zhu, J., Luo, B.-H., Xiao, T., Zhang, C., Nishida, N. and Springer, T. A. (2008). Structure of a complete integrin ectodomain in a physiologic resting state and activation and deactivation by applied forces. *Molecular cell* **32**, 849–861.

Zhu, J., Zhu, J., Bougie, D. W., Aster, R. H. and Springer, T. A. (2015). Structural basis for quinine-dependent antibody binding to platelet integrin αIIbβ3. *Blood* **126**, 2138–2145.

9. Appendix

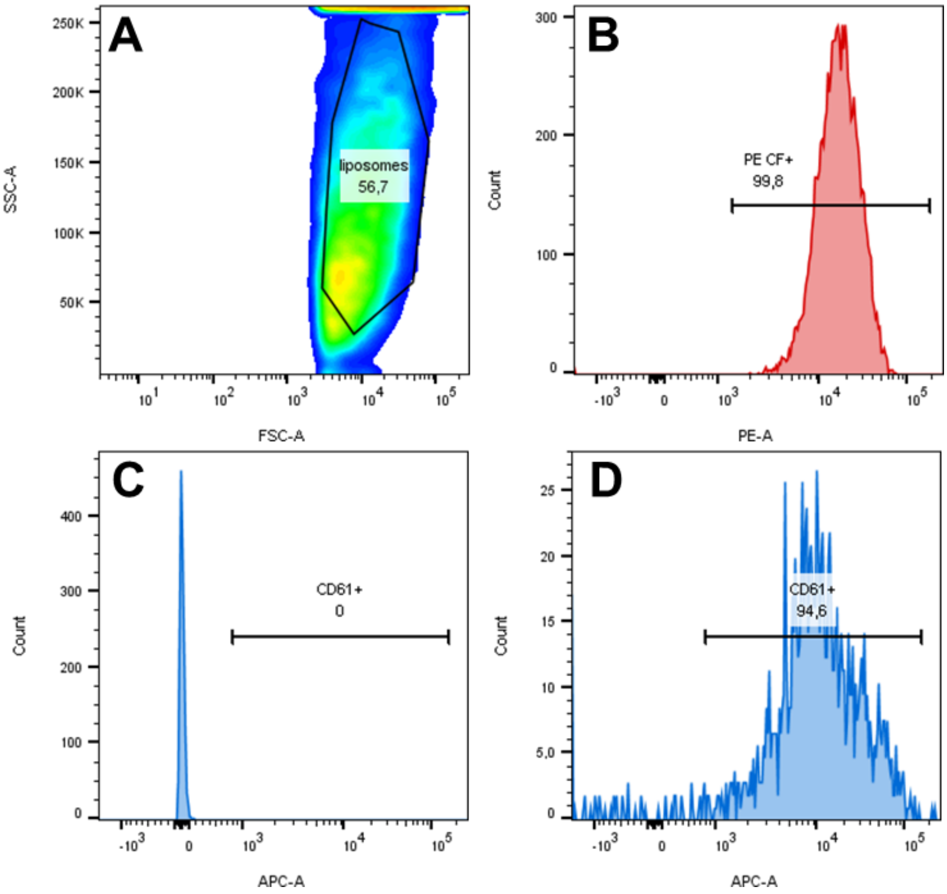

Figure S1: Representative FACS plots for integrin detection and activation measurements with liposomes. A) PE CF-labeled liposomes and proteoliposomes were analyzed in a flow cytometer as SSC and FSC (log scale) plot and B) PE CF positive (+) particles are displayed in a histogram. Representative histograms showing Alexa-647 (APC) mean intensities for PE CF positive liposomes (C) or proteoliposomes (D). Samples were stained with either anti-CD61 Alexa 647, PAC-1 Alexa-647 or anti-CD41 antibodies diluted 1:10 with the sample. CD41-labelled sample was additionally incubated with secondary antibody goat-anti mouse IgG Alexa-647.

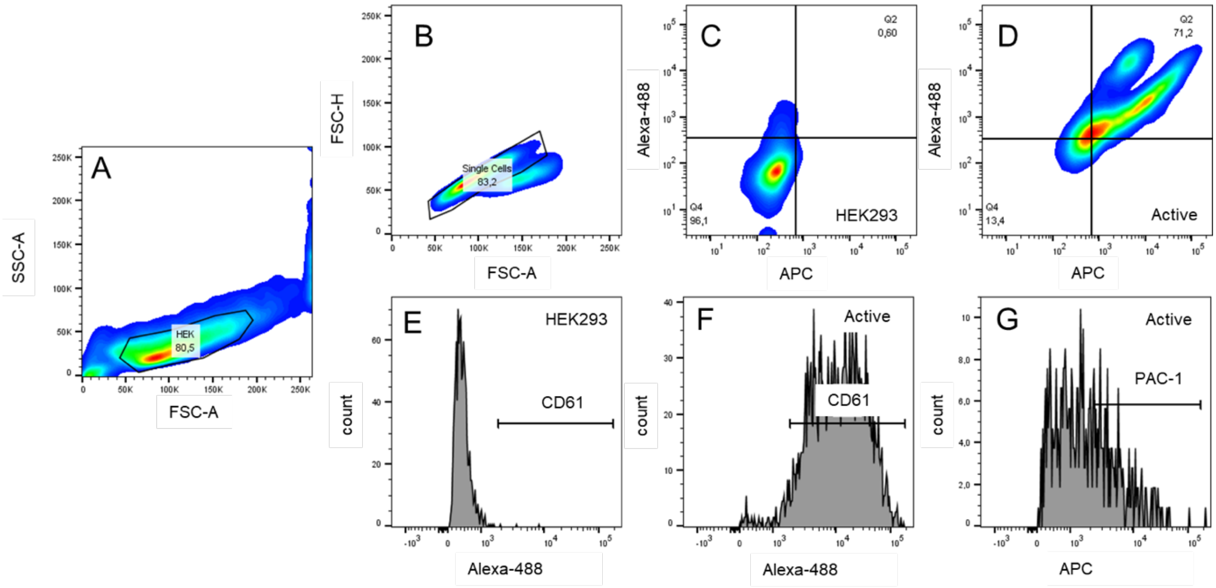

Figure S2: Representative FACS plots for integrin activation measurements with HEK293 cells. (A) First SSC and FSC were plotted and (B) single cells were marked using the FSC-H (h-heigth) parameter. C) From the single cells all Alexa-488 and APC (corresponding Alexa 647) positive cells (stained with anti-CD61 Alexa 488 and PAC-1 Alexa-647 antibodies 1:100 dilution in PBS) were tagged and are displayed for C) HEK293 and D) active integrin mutant expressing cells. Afterwards, histograms of all CD61 positive cells, representative for HEK293 cells (E) and for active integrin mutant (F), were marked and from this population, PAC-1 positive cells were gated (G).

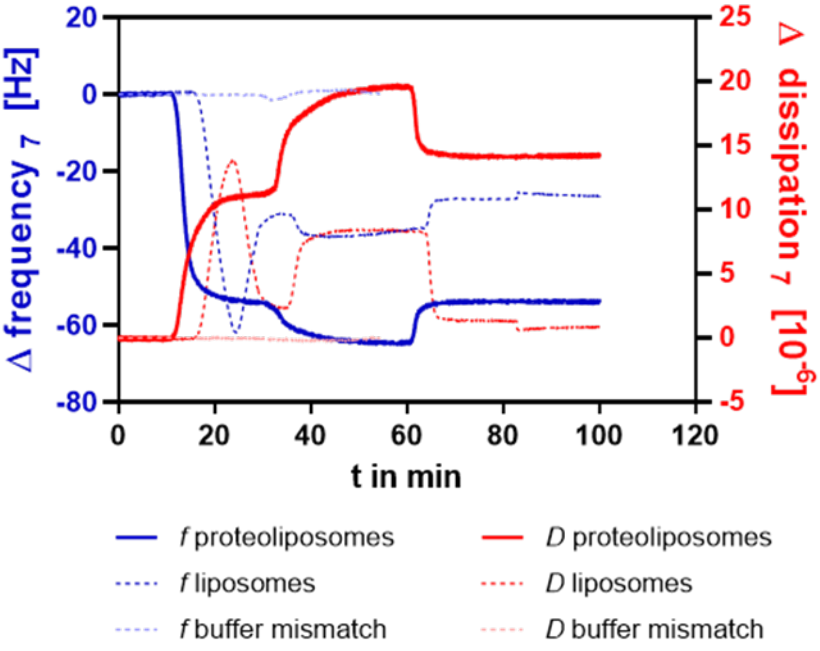

Figure S3: Representative QCM-D experimental profile for the buffer changes. Changes in dissipation (D-red) and frequency f (blue) of the seventh overtone at 37 °C. PBS buffer was injected over the SiO_2 sensors and after reaching a baseline, liposomes or proteoliposomes were injected (10 min) and the formation of a bilayer was observed except for control injections of buffer on blank surface. After a washing step with PBS containing 1 mM Mn^{2+}, 1 mM Ca^{2+}, 1mM Mg^{2+}. Rinsing with PBS buffer (60 min) followed for bilayer samples.

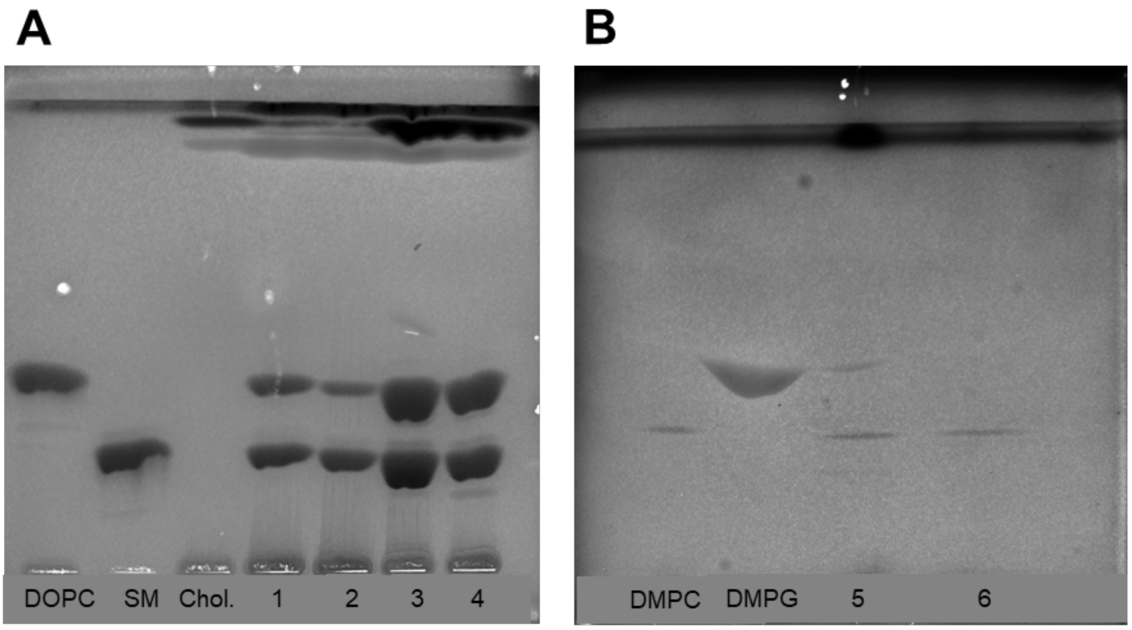

Figure S4: Thin-layer chromatography of lipids extracted from liposome samples. A) DOPC, SM and cholesterol standard. 1- liposomes CHAPS protocol, 2- proteoliposomes CHAPS protocol, 3- liposomes Triton protocol, 4- proteoliposomes Triton protocol, B) DMPG and DMPC standards, 5- liposomes Triton protocol, 6- proteoliposomes Triton protocol.

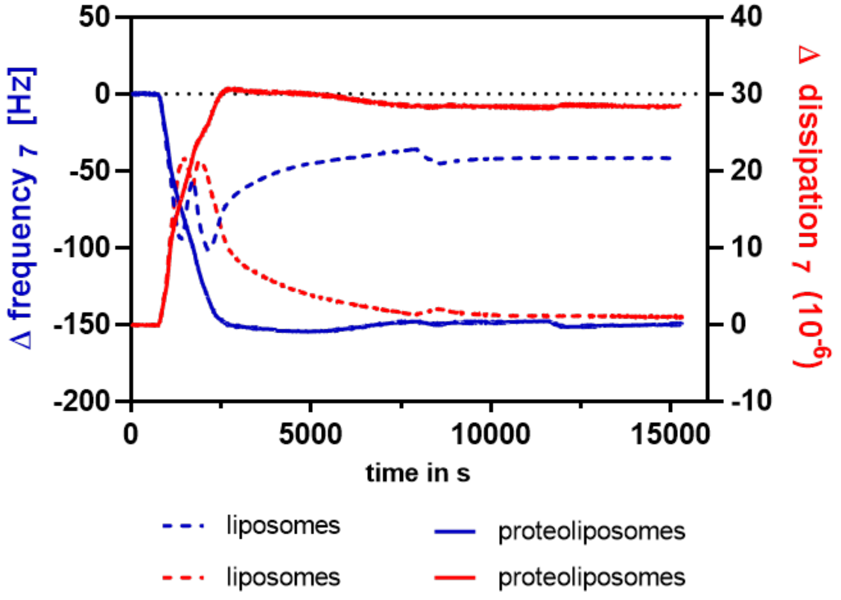

Figure S5: Representative QCM-D experimental profile of DOPC:SM:cholesterol liposomes/proteoliposomes. Changes in dissipation (D-red) and frequency f (blue) of the seventh overtone at 37 °C. HEPES buffer was injected over the SiO_2 sensors and after reaching a baseline, liposomes or proteoliposomes, prepared with Triton protocol and 37.5:37.5:25 lipid ratio DOPC:SM:cholesterol, were injected (10 min) and the absorbance of vesicles was observed. Vesicle fusion should be induced by injection of AH peptide at 2000 s. After a washing step with HEPES buffer, PAC-1 antibody was injected (7500 s) which was followed by rinsing with buffer.

Table S1: Changes in frequency upon PAC-1 binding to liposome- or proteoliposome-derived bilayer with different lipid ratios in QCM-D measurements. Bilayer was formed on SiO2 surface at 37 °C. Different ratios of DOPC:SM:cholesterol and DMPG:DMPC 1:20 as control are loaded on the sensor surface.

Δ *f* [Hz]	**liposomes**		**proteoliposomes**	
	buffer	Mn^{2+}	buffer	Mn^{2+}
25:35:40	0,25 ± 0,11	0,79 ± 0,13	0,46 ± 0,21	0,38 ± 0,17
37.5:37.5:25	0,25 ± 0,00	0,20 ± 0,00	1,28 ± 0,41	2,04 ± 0,70
45:30:25	0,26 ± 0,04	0,50 ± 0,07	0,28 ± 0,10	1,63 ± 0,21
60:28:12	0,27 ± 0,14	0,24 ± 0,16	0,62 ± 0,13	1,46 ± 0,58
70:25:5	0,35 ± 0,25	0,50 ± 0,35	0,92 ± 0,39	0,87 ± 0,18
20:1	1,00 ± 0,00	0,20 ± 0,00	1,39 ± 0,04	4,00 ± 0,14

R-Skript – Evaluation of RT-DC and AFM data using RStudio with linear mixed model

```
####### RT-DC Mutants #############

#set working directory

setwd("C:/Users/Thersa/Desktop/Statistik/HiWi")

# load packages

pacman::p_load(tidyverse, car, lmerTest, emmeans, MASS, Hmisc)

emm_options(lmerTest.limit = 100000)

RTDC <- read_delim(file = "RT-DC_Una.txt",

                   delim = "\t",

                   col_names = TRUE)

RTDC$cell_line <- as.factor(RTDC$cell_line) #??

RTDC$cell_line <- relevel(RTDC$cell_line, ref = "integrin")

levels(factor(RTDC$cell_line))

RTDC$treatment <- as.factor(RTDC$treatment)

RTDC$treatment <- relevel(RTDC$treatment, ref = "untreated ")

levels(factor(RTDC$treatment))


l1 <- quantile(RTDC$YM_kPa, c(0.05))

u1 <- quantile(RTDC$YM_kPa, c(0.95))


RTDC_new <- lmer(log(YM_kPa) ~ factor(cell_line) * factor(treatment)

              + (1|replica),
```

```
        data = RTDC,
        REML = FALSE,
        subset = (YM_kPa >= l1 & YM_kPa <= u1))
Anova(RTDC_new)
summary(RTDC_new)
ls_new <- emmeans(RTDC_new,
          pairwise ~ cell_line*treatment,
          adjust = NULL,
          type = "response")
sum_new <- summary(ls_new, type = "response")
sum_new$emmeans <- as.data.frame(sum_new$emmeans)



ggplot(sum_new$emmeans,
    aes(x=as.factor(cell_line),
     y=response,
     fill=factor(treatment))) +
 geom_bar(position=position_dodge(),
     stat="identity") +
 geom_errorbar(aes(ymin = response - SE,
          ymax = response + SE),
        width=0.2,
        position = position_dodge(0.9)) +
 coord_cartesian(ylim = c(0, 1)) +
 ylab("YM [kPa] means") +
 ggtitle("RTDC Una") +
 xlab("cell line")
####################################
#########################################
#########  AFM Mutants ##################
#####################################
####################################
#set working directory
setwd("C:/Users/Thersa/Desktop/Statistik/HiWi")
```

```
# load packages
pacman::p_load(tidyverse, car, lmerTest, emmeans, MASS, Hmisc)
emm_options(lmerTest.limit = 50000)
# load data
AFM <- read_delim(file = "AFM_komplett.txt",
                  delim = "\t",
                  col_names = TRUE)

# define factors and set "integrin" as reference factor
AFM$cell_line <- as.factor(AFM$cell_line) #??
levels(factor(AFM$cell_line))
AFM$cell_line <- relevel(AFM$cell_line, ref = "integrin")
levels(factor(AFM$cell_line))
AFM$treatment <- as.factor(AFM$treatment)
AFM$treatment <- relevel(AFM$treatment, ref = "untr")
levels(factor(AFM$treatment))
#due to some very high values, outliers are removed (here meaning the highest and lowest
1% of all data points)
l1 <- quantile(AFM$Data, c(0.05))
u1 <- quantile(AFM$Data, c(0.95))
#only values in between lower and upper percentiles are used for model fitting
# fit data to generalizes linear mixed model
AFM_model <- lmer(log(Data) ~ factor(cell_line) * factor(treatment) +
                  (1|replica) +
                 (1|replica:cell_ID) +
                 (1|replica:cell_ID:position_ID),
               data = AFM,
               REML = FALSE,
               subset = (Data >= l1 & Data <= u1))
# & (replica=="C")
#perform Anova to check for significance
Anova(AFM_model)
summary(AFM_model)
#calculate estimated marginal means
ls_afm <- emmeans(AFM_model,
```

```
                    pairwise ~ cell_line*treatment,
                    adjust = NULL)
#warning: "treatment" and "cell_line" is not a factor
sum_afm <- summary(ls_afm, type = "response")
sum_afm$emmeans <- as.data.frame(sum_afm$emmeans)
ggplot(sum_afm$emmeans,
       aes(x=as.factor(cell_line),
           y=response,
           fill=factor(treatment))) +
  geom_bar(position=position_dodge(),
           stat="identity") +
  geom_errorbar(aes(ymin = response - SE,
                    ymax = response + SE),
                width=0.2,
                position = position_dodge(0.9)) +
  coord_cartesian(ylim = c(0, 350)) +
  ylab("YM [Pa] means") +
  ggtitle("AFM Mutants") +
  xlab("cell line")
################ Tests
ranef(AFM_model)
coef(AFM_model)
print(dotplot(ranef(AFM_model, condVar=T))[['replica']])
print(dotplot(ranef(AFM_model, condVar=T), groups=AFM$cell_line)[['replica']])
```

Statistical Analysis – p-values

Table S2: Contrast of two cell lines and their respective p-values from RT-DC measurement as described in chapter 3.6.6. The different cell lines are stated with short names: integrin αIIbβ3 wildtype=” integrin”, αIIbβ3 Inactive=” inactive”, αIIbβ3 Active=” active”, HEK293= “ control”. The treatments are stated as untreated-standard cell media, Mn-standard cell media containing 1 mM $MnCl_2$, EDTA-standard cell media containing 5 mM EDTA. Significance levels are displayed according to the p-values as [***] for p-values < 0.001, [**] for p-values 0.001 – ≤ 0.01 and [*] for p-values of 0.01 – 0.05.

contrast					p-value	significance
cell line	treatment		cell line	treatment		
integrin	untreated	/	active	untreated	0.0938	
integrin	untreated	/	control	untreated	0.2133	
integrin	untreated	/	inactive	untreated	<.0001	***

integrin	untreated	/	integrin	EDTA	<.0001	***
integrin	untreated	/	active	EDTA	<.0001	***
integrin	untreated	/	control	EDTA	<.0001	***
integrin	untreated	/	inactive	EDTA	<.0001	***
integrin	untreated	/	integrin	Mn	<.0001	***
integrin	untreated	/	active	Mn	<.0001	***
integrin	untreated	/	control	Mn	<.0001	***
integrin	untreated	/	inactive	Mn	0.0024	**
active	untreated	/	control	untreated	0.0022	**
active	untreated	/	inactive	untreated	<.0001	***
active	untreated	/	integrin	EDTA	<.0001	***
active	untreated	/	active	EDTA	<.0001	***
active	untreated	/	control	EDTA	<.0001	***
active	untreated	/	inactive	EDTA	<.0001	***
active	untreated	/	integrin	Mn	<.0001	***
active	untreated	/	active	Mn	0.0013	**
active	untreated	/	control	Mn	<.0001	***
active	untreated	/	inactive	Mn	<.0001	***
control	untreated	/	inactive	untreated	<.0001	***
control	untreated	/	integrin	EDTA	<.0001	***
control	untreated	/	active	EDTA	<.0001	***
control	untreated	/	control	EDTA	<.0001	***
control	untreated	/	inactive	EDTA	<.0001	***
control	untreated	/	integrin	Mn	<.0001	***
control	untreated	/	active	Mn	<.0001	***
control	untreated	/	control	Mn	<.0001	***
control	untreated	/	inactive	Mn	0.0500	*
inactive	untreated	/	integrin	EDTA	<.0001	***
inactive	untreated	/	active	EDTA	<.0001	***
inactive	untreated	/	control	EDTA	<.0001	***
inactive	untreated	/	inactive	EDTA	<.0001	***
inactive	untreated	/	integrin	Mn	<.0001	***
inactive	untreated	/	active	Mn	<.0001	***
inactive	untreated	/	control	Mn	<.0001	***
inactive	untreated	/	inactive	Mn	0.0089	**
integrin	EDTA	/	active	EDTA	0.0009	***
integrin	EDTA	/	control	EDTA	0.0005	***
integrin	EDTA	/	inactive	EDTA	0.0001	***
integrin	EDTA	/	integrin	Mn	<.0001	***

Table S3: Contrast of two cell lines and their respective p-values from AFM measurement as described in chapter 3.6.5. The different cell lines are stated with short names: integrin αIIbβ3 wildtype=” integrin”, αIIbβ3 Inactive=” inactive”, αIIbβ3 Active=” active”, HEK293= “control”. The treatments are stated as untreated-standard cell media, Mn-standard cell media containing 1 mM $MnCl_2$. Significance levels are displayed according to the p-values as [***] for p-values < 0.001, [**] for p-values 0.001 – ≤ 0.01 and [*] for p-values of 0.01 – 0.05.

contrast					p-value	significance
cell line	treatment		cell line	treatment		
control	untreated	/	control	Mn	<0.0001	***
integrin	untreated	/	integrin	Mn	<0.0001	***
active	untreated	/	active	Mn	0.0262	*
inactive	untreated	/	inactive	Mn	0.8364	
control	untreated	/	integrin	untreated	<0.0001	***
control	untreated	/	active	untreated	0.2507	
control	untreated	/	inactive	untreated	<0.0001	***
control	Mn	/	integrin	Mn	0.0008	**
control	Mn	/	active	Mn	<0.0001	***
control	Mn	/	inactive	Mn	<0.0001	***

Acknowledgements

Diese Arbeit wäre ohne die Hilfe und Unterstützung von vielen besonderen Menschen nicht möglich gewesen.

Many thanks to Mihaela Delcea, who supervised and guided me through my whole PhD time. You gave me the opportunity to grow every day with challenges, excelling and learning a lot about myself. Thank you also for the freedom, patience and confidence during this time period.
Ich möchte auch gern Frau Professorin Sabine Müller danken, die mich als „kommissarische Doktormutter" aufgenommen und mir den Einstieg als Promovendin erleichtert hat.
This work was financially supported by the European Research Council (ERC) Starting Grant 'PredicTOOL' (637877).
Peter Nestler, dir bin ich sehr dankbar für deine Unterstützung als Seelsorger, positiv-Denker und als guter Vermittler physikalischen Wissens für Dummies.
Ich möchte mich außerdem vom ganzen Herzen bei Felix Nagel bedanken! Ohne dich hätte ich vermutlich schon vor zwei Jahren aufgehört und hätte aufgegeben. Wegen dir bin ich wieder gerne ins Labor gegangen, in Zeiten in denen es mir nicht gut ging. Danke für den Spaß während der Arbeit, das gemeinsame Echauffieren über alles und jeden, für Glühwein/Pizza/Bier//Wein/Doku Abende und die sinnvollen wie auch sinnlosen Diskussionen. Du weißt ja geteiltes Leid ist halbes Leid… und dafür bin ich dir sehr dankbar.
In diesem Zuge möchte ich auch der gesamten Arbeitsgruppe Biophysikalische Chemie, früher Nanostructure, danken! Ganz besonderer Dank gilt dabei Anne Susemihl, Alexandra Mitlehner, Aileen Weide und Eric Tönnies, für den Spaß und die tolle Arbeitsatmosphäre; nicht zuletzt auch für eure Hilfe im Laboralltag und eure immerwährende Motivation, selbst bei niederschlagenden Ergebnissen, wenn wieder nichts geklappt hat oder ich einfach, mal wieder, keine Zeit hatte.
Danke auch an Ina Buchholz, für die liebe Aufnahme in die Arbeitsgruppe, die lustigen Dienstreisen und wissenschaftlichen Ratschläge.
Ohne die aufmunternden Worte und die Hilfe von Doreen Biedenweg und Astrid Kempcke wäre ich so manches Mal verzweifelt. Danke dafür!
Martin und Norman möchte ich für amüsante Arbeitsgruppenausflüge und interessante tiefgründige Gespräche danken, sowie den Willen immer eine Lösung zu finden, das ist eine tolle Eigenschaft! Danke Norman für deine Hilfe und Geduld bei den Bildern!
Auch Herrn Oliver Otto, Ünal Coskun und Theresia Gutmann gilt mein Dank für die Unterstützung, neue wissenschaftliche Perspektiven und inspirierenden Diskussionen. Stephanie Spiegler, dir danke ich für deine Geduld und deinen Rat während der Mutagenesen, ohne den ich so manches Mal keinen Ausweg gewusst hätte.

I would like to thank also Adnane Achour and Tim Schulte from the Karolinska Institute in Stockholm for their support, even when my cells are doing crazy things, and the opportunity to learn new techniques in your lab!

Many thanks also to Prof. Karen Vanhoorelbeke for the kind gift of Plasmid DNA, which was the basis for the mutagenesis studies and cell experiments.

Vielen Dank an Theresa Brinker und Stephan Groß für die Hilfe bei der statistischen Auswertung der AFM und RT-DC Daten.

Auch dem Imaging Center des Instituts für Biologie der Universität Greifswald möchte ich für die TEM Bilder danken.

Dem Mentoring Programm der Universität Greifswald, besonders Frau Hoppe und Frau Ehmler, als auch dem Graduiertenkolleg BioX, danke ich für interessante und entscheidende Seminare und Workshops. Besonderer Dank gilt auch meiner Mentorin Professorin Müller-Hilke; durch Ihre ehrlichen Worte und den wegweisenden Gesprächen konnte ich viel lernen und wichtige Entscheidungen treffen.

Ein herzliches Dankeschön geht an Annemarie Struck, ohne die ich diese Arbeit wohl nie beendet hätte. Sie haben mich in meiner dunkelsten Zeit wiederaufgebaut und mir den Mut gegeben weiter zu machen.

Theresa Schwaiger meine liebe, dir danke ich für deine großartige Sicht auf die Dinge und deine Gelassenheit, die mich inspiriert und so manches Mal vor der Verzweiflung bewahrt hat.

An meine Voltis in Wusterhusen geht ein großer Dank für Eure Unterstützung und die geistigen Pausen sowie die Erdung, die ich immer wieder gebraucht habe. Dank dafür!

Meine lieben Freunde, euch danke ich für die Aufmunterungen, Auszeiten, Motivationsschübe und Hilfe während der letzten Jahre! Ihr seid wunderbar.

Björn, dir danke ich von Herzen dafür, dass du mir den Rücken freigehalten, meine Launen ertragen und mich trotzdem geheiratet hast. Du bist das wunderbarste was mir passiert ist.

Meine liebe Familie, ganz besonders meinen Eltern, danke ich für die Freiheit und Unterstützung in jedweder Hinsicht. Ihr habt mir all das ermöglicht und dafür bin ich euch auf ewig dankbar!